THEORETICAL CHARACTERIZATION OF THE STRUCTURAL, ELECTRONIC AND MECHANICAL PROPERTIES OF SUPERCONDUCTING $GdBa_2Cu_3O_{7-x}$

AGORA OMARI JARED

MSc. PHYSICS, BED SCIENCE (KENYATTA UNIVERSITY)

A THESIS SUBMITTED TO THE BOARD OF POST-GRADUTE STUDIES IN PARTIAL FULFILLMENT OF THE REQUIREMENT OF THE AWARD OF THE DEGREE OF DOCTOR OF PHILOSOPHY IN PHYSICS IN THE SCHOOL OF PURE AND APPLIED SCIENCES, DEPARTMENT OF PHYSICS OF KISII UNIVERSITY

2023

DECLARATION BY THE CANDIDATE

This thesis is my original work and has not been presented for a degree in any other university.

Jared Omari Agora Signature ……………….. Date ……………………….

RECOMMENDATION BY THE SUPERVISORS

This thesis has been submitted for examination with our approval as University Supervisors.

Dr. Philip Otieno Nyawere Signature ……………….. Date ……………

Senior Lecturer Kabarak University

Department of Physical and Biological Sciences

Kabarak University

Dr.Calford Otieno Signature ……………….. Date …………….

Lecturer

Department of Physics

Kisii University

Dr. George Simiyu Manyali Signature ………………. Date …………….

Senior Lecturer

Department of Physical Sciences

Kaimosi Friends University

PLAGIARISM DECLARATION

DECLARATION BY STUDENT

i. I declare I have read and understood Kisii University Postgraduate Examination Rules and Regulations, and other documents concerning academic dishonesty.

ii. I do understand that ignorance of these rules and regulations is not an excuse for a violation of the said rules.

iii. If I have any questions or doubts, I realize that it is my responsibility to keep seeking an answer until I understand.

iv. I understand I must do my own work.

v. I also understand that if I commit any act of academic dishonesty like plagiarism, my thesis/project can be assigned a fail grade ("F")

vi. I further understand I may be suspended or expelled from the University for Academic Dishonesty.

Jared Omari Agora Signature ……………..
Reg. No. DPS/70041/14 Date …………………..

DECLARATION BY SUPERVISOR (S)

i. I/we declare that this thesis/project has been submitted to plagiarism detection service.

ii. The thesis/project contains less than 20% of plagiarized work.

iii. I/we hereby give consent for marking.

Dr. Philip Otieno Nyawere Signature ……………….. Date …………
Senior Lecturer Kabarak University
Department of Physical and Biological Sciences
Kabarak University

Dr.Calford Otieno Signature ……………….. Date …………….
Lecturer
Department of Physics
Kisii University

Dr. George Simiyu Manyali Signature ………………. Date ………….
Senior Lecturer
Department of Physical Sciences
Kaimosi Friends University

DECLARATION OF NUMBER OF WORDS FOR THE THESES

I confirm that the word length of:

1) The thesis, including footnotes, is 38,842 2) the bibliography is 8,759

and, if applicable, 3) the appendices are 2,942

I also declare the electronic version is identical to the final, hard bound copy of the thesis and corresponds with those on which the examiners based their recommendation for the award of the degree.

Jared Omari Agora Signature ……………….. Date …………………..

I confirm that the thesis submitted by the above-named candidate complies with the relevant word length specified in the School of Postgraduate and Commission of University Education regulations for the Masters and PhD Degrees.

Dr. Philip Otieno Nyawere Signature ……………….. Date ……………

Senior Lecturer Kabarak University
Department of Physical and Biological Sciences
Kabarak University
Dr.Calford Otieno Signature ……………….. Date …………….
Lecturer
Department of Physics
Kisii University
Dr. George Simiyu Manyali Signature ………………. Date …………….

Senior Lecturer

Department of Physical Sciences

Kaimosi Friends University

COPY RIGHT

DEDICATION

To my dear wife Harriet,my son Brandon and my daughter Brandy.

ACKNOWLEGEMENT

I wish to express my sincere acknowledgement the following persons for the support during this work: my supervisors and technical advisor Dr. Philip Nyawere, Dr. George Manyali and Dr. Calford Otieno, they offered to use their vast experience in this area of study to guide and properly advise in all steps in this work; my fellow post graduate students at Kisii University and other Universities with whose we shared different levels of difficult in the research process; The Centre for high performance computing (CHPC) which offered the cluster resources that we used for the computing process; members to physics department and the entire faculty of Kisii University for their most criticism which made serious improvement of the work and the organizers of various workshop for their consideration to have different section of this work presented which indeed led to betterment and improvement.

ABSTRACT

The aim of the study was to characteris the $GdBa_2Cu_3O_{7-x}$ perovskite superconductor with the view knowing the associated properties under different conditions of pressure. The study applied the computational methods to investigate the structural, electronic and mechanical, properties of the $GdBa_2Cu_3O_{7-x}$ perovskite superconductor and determined how its properties affect the mechanism of superconductivity. With the local the generalized gradient approximation in the frame work of density functional theory using the Quantum espresso code, the ground state properties and equation of state were obtained using the Plane waves. The phenomenon of phase transition studied through pressure induction. The effect of pressure on the band structure, density of states and the partial density of state were also assessed. The orbitals that are responsible for metallization and superconductivity were also computed at varied pressure. The effect holes doping with pressure was also simulated. The BCS theory and the Mc Millan's equation were used to calculate its superconducting transition temperature at different pressure. Doping with variation of oxygen concentration was done. The phase transition was found to occur at 21.9 GPa. It was found that pressure results to narrowing of the band gap for this material and eventually the material undergoes metallization. The orbital that become predominant at the high superconductivity transition temperature below the pressure of phase transition were; Cu 1d and O 2p from the CuO in the valence band near the Fermi level and the Gd 5p near the Fermi level. The stability criterion was satisfied from the calculated elastic constants. Calculated elastic properties were used to calculate Debye temperature and the maximum value was achived at ~20GP. The underdoped regime, where the holes were smaller compared to the ones at optimum doping, was determined to be below 20 GPa of doping pressure. Optimal doping pressure where was achieved at ~ 20 GPa.. There was a drop in T_C above the pressure of around ~20 GPa, which was considered the overdoping regime. The highest calculated T_C (max) was ~141.16 K at ~20GPa. With oxygen doping the T_C (max) was found to be 137.9 K when the value of x was 0.65. the finding of the study can be used to in material design for applications

TABLE OF CONTENTS

Debye temperature is a thermodynamic quantity in material science that is associated with the phonon vibrational modes in a crystal, elastic constant and specific heat. For isotropic elastic medium it is given by (Ledbetter et al., 1987):**Error! Bookmark not defined.**

LIST OF FIGURES

LIST OF ABBREVIATION

$(La_{1-x}Ca_x)MnO_3$	Lanthanum calcium manganese oxide
E_C	Correlation energy
E_X	Exchange energy
t_f	Goldschmidt tolerance factor
ε_F	Fermi surface
ε_{XC}	Exchange-correlation energy
Λ	Superconductivity order parameter
2G	Second Generation
AFM	Antiferromagnetic
B	Magnetic Induction
$Ba(Bi_{1-x}Pb_x)O_3$	Barium bismuth lead oxide
$BaTiO_3$	Barium titanium oxide
BCS	Bardeen-Coopers-Schrieffer
Ca	Calcium
CC	Coated Conductors
CuO_2	Copper oxide
DFT	Density Functional Theory
DOS	Density of states

FE	Ferroelectric
FM	Ferromagnetic
G	Gibbs free energy
GBCO	Gadolinium Barium Copper Oxide
Gd123	Layer gadolinium cuprate superconductor
$GdBa_2Cu_3O_{7-x}$	Gadolinium Barium Copper oxide
GGA	Generalized gradient approximation
GMR	Giant magneto résistance
H_0	zero magnetic field
H_{c1}	First critical magnetic field
H_{c2}	Second critical magnetic field
Hg	Gold
HTS	High Temperature Superconductor
I_c	Critical Current
J	Current Density
J_c	Critical Current Density
$La_{1-x}CaMnO_3$	Lanthanum calcium manganese oxide
LaBaCuO	Lanthanum barium copper oxide
$LaMnO_3$	Lanthanum manganese oxide
LDA	Local density approximation

LSDA	Local spin-density approximation
MI	Metal insulator
Na_xWO_3	Sodium tungsten oxide
OPW	Orthogonalized plane waves
PBE	Perdew, Burke, and Ernzenhoff
PDOS	Partial density of states
PE	Pyro electric
PwSCF	Plane wave Self-consistent field
Re123	Rare Earth Metal-123 Perovskites
ReBaCuO	Rare earth metals barium copper oxide
SCF	Self-consistent field
$Sr_2TaO_{5.5}$	Strontium tantalum oxide
T_c	Superconductivity transition temperature
TFEL	Transient field electroluminescence
TiBaCaCuO	Titanium Lanthanum barium copper oxide
T_N	Neel temperature
V(r).	Potential at distance (r)
V_r	External Potential
Y123	Yttrium- 123 Perovskites
YBCO:123	Yttrium barium copper oxide

CHAPTER ONE

INTRODUCTION

1.1 Background to the Study

The yttrium barium copper oxide (YBCO:123), a ceramic superconductor, was the first perovskite to exhibit the highest superconducting state with a critical temperature (T_C) of 92K (Ramli *et al*., 2016). This is a major achievement because liquid nitrogen, which has a temperature below that could be used as a coolant in applications (Hao *et al*., 2015). This intensified research and studies to search for high T_C superconducting materials with great interest in various applications (Park, 2015). Intensive research has been conducted on double perovskites materials because of their extraordinary magnetic and transport properties (Mnefgui *et al*., 2013; Nabi *et al*., 2019). Analysis shows that the deformation of YBCO ceramics affects their mechanical properties (Bobrov, 1993; Ozturk *et al*., 2019). Mechanical properties are an important consideration in determining the essentials of material design and operating conditions (Alknes *et al*., 2016; Sugano-Segura *et al*., 2017). Experimental analysis using X-ray diffraction where rare-earth metals replace the yttrium atoms in the YBCO:123 has also been done (Bondarenko *et al*., 2017; Kim *et al*., 2020). The observed behavior of the side layers and the mobile oxygen was nearly the same by structural appearance. The crystal structures of these oxides are layered, comprising consecutive layers along the longest side of their orthorhombic crystal structure. The transformation of the cubic perovskites to the layered structure makes the oxygen bonding relatively weak in the layers and provides disorder-free channels for ion mobility (Xinxin Zhang, 2016). These results in doping which can transform the crystal to different phases with renewed properties and T_C (Nakamura *et al*., 2017; Shimojima *et al*., 2017). The influence of doping can also affect oxygen diffusivity and can result in the development of a new class of material with improved properties (Baiutti *et al*., 2015; Kushima & Yildiz, 2010).

Superconducting technology is one of the exciting areas of modern research and technological applications (Brittles *et al*., 2015; Robinson *et al*., 2020; Vinet & Zhedanov, 2011). This is based on the wide range of applications and high efficiency which is associated with the structural, electronic, mechanical, optical, thermoelectric, and magnetic properties of the superconductors (Nabi *et al*., 2019; J. Wang *et al*., 2019). There is an increasing desire to use superconducting electricity in many areas such as the electromotive and aircraft industries as a way of achieving cheap and clean environmentally friendly energy (Robinson *et al*., 2020; X. Sun *et al.*, 2019; J. Wang *et al*., 2019). Superconductivity is one of the ways to assist achieve such desire and therefore there is a great need to understand the best way to utilize superconductors for a better outcome. Since the discovery of superconductors in the year 1911 (Delft, 2012) there have been intense efforts to understand the mechanism that leads to superconductivity (Allender & Bardeen, 1973; Dewar, 1987; Lozovik & Yudson, 1976; Takada, 1978) and how to achieve better conditions for superconducting properties. The discovery of high-temperature superconductors has been one of the greatest achievements in the field and has made it possible for superconductors to be practically used in various technological applications (Bray, 2009; Durrell *et al*., 2018; Hull, 2003; Hull & Murakami, 2004). Among the problems that the practical superconductor has solved is the over-dependency on fossil fuel and other non-renewable energy which is an environmental threat.

In this connection, an effort has been directed toward cheaper and clean energy. Wind power with superconducting wires, which is considered one of the technologies to deliver the renewable energy and turbines wound on superconducting wires instead of the regular copper generator (Y. Lee, 1991; Qu *et al*., 2013; Rahim & Mohammad, 1994; Sarkar & Bhattacharyya, 2012) are some of the modern technologies that make use of superconductors. This is because they are much more efficient and are light weighted and compact than the non-superconducting technology (Barnes *et al*., 2005; Jensen *et al*., 2012; Radebaugh, 2012; Sanz *et al*., 2014). To this, there are several types of High Temperature Superconductor (HTS) rotating machines: those using some bulk superconductor, those using superconductor wires, and those using both.

High-temperature Superconductors are classified depending on the ease at which the magnetic field is expelled out of a material as it achieves a superconductivity state and also the elemental composition of the superconductor. The former leads to first-generation superconductors and the latter leads to second-generation superconductors.

The second-generation HTS in which $GdBa_2Cu_3O_{7-x}$ belongs is the most preferred over the first-generation HTS. For industrial and other applications, the second generation HTS wires are strong given their high irreversibility stress limit (Mohan & Gopi, 2020; Shin & Bautista, 2019, 2018). The current carrying capacity of the second generation wires is mainly associated with electrical current density which depends on the prevailing magnetic field and temperature (Wang *et al* 2009). This is important in consideration of the high stresses that are often encountered in applications such as high field insert coils and high-speed rotating machines. An example of an HTS application is the turbines wound on superconducting wires instead of the normal copper which leads to much higher efficiency, enabling the achievement of the lightweight and compact generator than the other known technology (Abrahamsen *et al*., 2012; Jia *et al*., 2016; Qu *et al*., 2013). Several types of HTS can be applied in rotating machines classified as those using bulk superconductosr, those using superconductor wires, and those that use both (Vélez *et al*., 2009).

The second-generation superconductor's classification comprises some pure metals, alloys, cuprate, and ceramics. The most preferred under this classification are ceramic and cuprate superconductors. Ceramics have the advantage of their superconducting critical temperature coinciding with that of liquid nitrogen and thus liquid nitrogen can be used as a coolant. The only disadvantage of this superconductor is their brittle nature which makes it difficult for them to be drawn into wires (Atul, 2018; Congreve *et al*., 2019; Rizi, 2019).

The cuprate superconductors are layered superconductors comprising copper oxide (CuO_2) (Le *et al*., 2009; H. H. Otto, 2016). These copper oxide layers are weakly coupled and determine the superconductivity of the material. The stable form of these materials is achieved by the presence of either rare earth metals or another suitable atom in the neighborhood of CuO_2 layers. Superconducting properties are determined by the extent of doping of electrons or holes in the layer (Dellea *et al*., 2017; Hirsch & Marsiglio, 2019; Wen *et al*., 2016). Cuprate perovskites have two layers between the copper oxide layers. For these types of superconductors, the hoping oxygen between the two layers enhances the superconducting properties. This means variation of oxygen concentration in these groups of materials greatly influences superconductivity. However, a certain reduction in oxygen concentration; below the optimal level, can lead to loss of superconductivity under the conditions that support superconductivity. The reduction is achieved by the use of a supercell crystal instate of a single cell crystal. A supercell is indicated in Appendix II.

The study of perovskite cuprate oxides has gained tremendous growth due to their unique characteristics (Mohammed *et al*., 2021; Singh *et al*., 2014; Varignon *et al*., 2017). These characteristics include; structural phase transition under certain conditions of temperature and pressure, semiconductor to metal transition, and superconductivity. The ability to manipulate the structure of these perovskites makes it possible to alter the electronic, structural, elastic, optical, and thermoelectric properties among others. The changes affect the bandwidth, atomic bonding, bond angles, bond length, atomic orientation, and porosity of the material, which then influence the associated properties. Therefore, it is of great interest to understand the structural, electronic, and mechanical properties of these perovskites.

In practice, cuprate superconductor applications may demand that the material be drawn into wires or tapes. Also, during the application, the material may be subjected to mechanical stress hence there is a need to understand the elastic properties of the material. The elastic properties give fine details on how the material's strain and stress correlate under specific conditions. Some of the effects of mechanical properties on the superconductor include the effect on the critical current density, trapped magnetic field (BT), and superconductivity transition temperature. One area of interest in applying these properties is the assessment of the capability of superconducting wires for a high field magnetism. It requires the determination of the current density and mechanical properties to handle the stress encountered during fabrication (Hernandez *et al*, 2013). This includes the thermal stress as a result of cooling down as well as any thermal changes that may result during a fault or quench situation (W. K. Chan *et al*., 2013; Poole *et al*., 2016; Senatore et al., n.d. Amin *et al*., 2009; Chiew et al., 2014).

It has been indicated that the study of crystalline materials under high pressure gives important information about properties in material science (C. Li *et al*., 2016; Mao *et al*., 2018; Shen & Mao, 2017). The properties may include conductivity behavior, better superconducting critical transition temperature, superconducting critical current density, and superconducting critical magnetic field. High pressure, just like high temperature can lead to phase transition as a result of reduced interatomic spacing which affects the crystal structure and electronic orbitals (Benmakhlouf *et al*., 2017; Inaguma *et al*., 2018; Zhao *et al*., 2017). Also inducing pressure can result in totally new material with different characteristics from the initial material (Hohenwarter, 2015; Machon *et al*., 2018).

The superconducting $GdBa_2Cu_3O_{7-x}$ has been studied under different conditions to assess the best conditions for application (Antonova *et al*., 2019; Cayado *et al*., 2017; Kargar *et al*., 2015; Mohan & Gopi, 2020; Yoon *et al*., 2016). The effect of pressure on the material has been found to influence many properties that are associated with the material (Drozdov *et a*l., 2015, 2019; Núñez-Regueiro *et al*., 2013; J. Zhu *et al*., 2013). Elevated pressure above the atmospheric pressure is known to influence the ultrasonic velocities in a crystal lattice. This is a result of the decrease in atomic porosity which reduces the interatomic spacing thus increasing the vibrational modes in the crystal lattice. The variation of the ultrasonic wave; both longitudinal and transverse is a result of the effect of the hydrostatic pressure imposed on the density, porosity, and oxygen concentration of the material. The accurate information obtained from such measurement is of great importance because it provides information about the vibrational modes and inharmonicity in the crystal lattice of this superconductor which leads to phenomena such as mode softening at the superconducting transition temperature or modulus hardening at the temperature below the superconducting transition temperature (Peng *et al.*, 2020). Changes in the ultrasonic sound velocities also affect the magnitude of the Debye temperature which is a thermodynamic quantity that relates the elastic properties and the internal temperature of a crystal (Haussühl *et al.*, 2020; Ledbetter *et al.*, 1975). The relationship brings about the temperature dependence of the ultrasonic sound velocity. The velocities are likely to increase as the crystal achieves low temperature. These changes associated with oxygen concentration can be attributed to the variation of oxygen in the CuO_2 chain along the b axis of the crystallographic plane of cuprate superconductors. The properties within the crystal that results in changing from superconducting to the non-superconducting state of the material are of great interest in trying to understand the superconducting mechanism. Also, the effect of pressure on crystalline materials has been used to predict new structures and their corresponding properties (Akhmatskaya & Nobes, 1999).

It has been reported that the oxygen concentration in the $GdBa_2Cu_3O_{7-x}$ greatly affects the properties of the material (Jin *et al.*, 2015; Ogunjimi *et al.*, 2020; Stoyanova-Ivanova *et al.*, 2015). For small values of x the material assumes stable orthorhombic structure. This happens for $x < 0.5$ and this small oxygen deficiency leads to an increase in superconducting transition temperature. The value of x is varied by the variation of oxygen atoms in the supercell crystal. When $x > 0.5$ the material undergoes a polymorphic phase transition to a non-superconducting tetragonal phase. At this range of oxygen concentration, the material loses the superconducting properties and attains new properties.

The composition of the oxygen planes and the layers comprising the charges makes it possible for doping to occur in the cuprate superconductors (Been *et al*., 2021; Emin, 2017). The concentration of the hole is varied in two ways; hole doping (p) or electron doping (n) in the charge concentration zones. Most cuprates will behave like Mott insulators when doping has not been induced in the planes (Cai *et al*., 2016; Cao *et al*., 2016; Yin *et al*., 2019). This is attributed to the large amount of energy that is likely to be involved in the movement of the holes in the same occupational site. However, upon doping, the cuprates assume metallic characteristics based on the shifting of the Fermi level and the Fermi energy, and as a result superconductivity and other properties associated with the material are likely to appear or disappear depending on the degree of doping (Furness *et al*., 2018; Greene *et al*., 2020). Figure 1.1 shows how the degree of doping influences the variation of different properties in a typical cuprate superconductor.

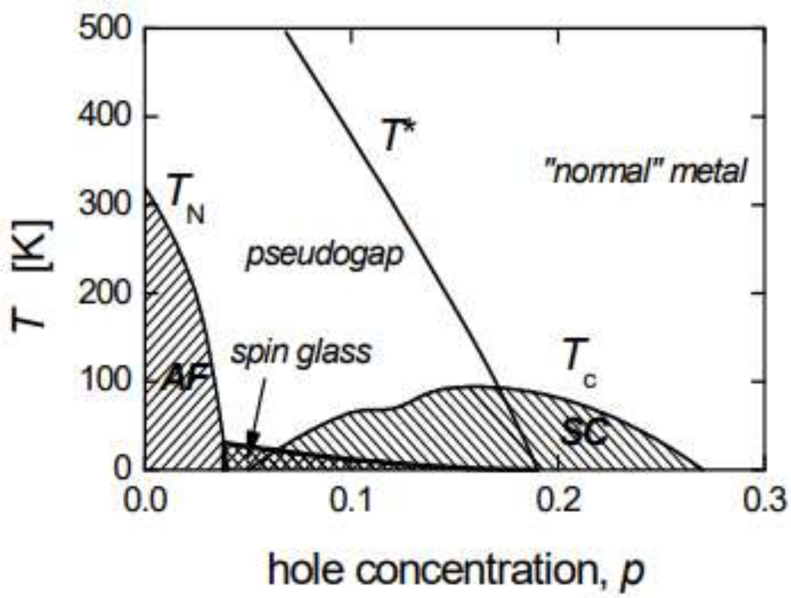

Figure 1.1: A phase diagram of a doped cuprate superconductor representing how temperature varies with the degree of doping.

From Figure 1.1 above, the material portrays different properties depending on the degree of doping. The antiferromagnetic phase occurs in the region before superconductivity and in the overlap region, the two exist. The pseudo gap exists above the superconductivity transition temperature. Above the superconductivity transition temperature, there is over doping leading to a decrease in the superconductivity transition temperature (Tallon, 2005).

It can be inferred that the introduction of the pseudo gap in relationship with the superconducting behavior of the superconductors coupled with the antiferromagnetic Mott insulators, cooper pairing, and the non-Fermi liquid are vital concepts in the understanding of the cuprate superconductors (Hashimoto *et al.*, 2008; Sakai *et al.*, 2010). The principle mechanism that leads to the variation of the properties due to doping can be associated with the magnetic ordering in the hole-doped CuO_2 planes in the perovskite cuprates (Albaalbaky *et al.*, 2018; Razia *et al.*, 2009).

The magnitude of the superconductivity transition temperature is determined by the extent of the antiparallel ordering of the magnetic states within the crystal which brings about the magnetically influenced superconducting states with the coupling of holes as cooper pairs. When the temperature rises above the $\mathbf{T_c}$ the organization of the pair state along the phase is lost, with the retention of the pair condensates, which leads to the transition to the pseudo gap in which state, the charge and magnetic ordering occur. The magnitude of the hole concentration in the Cu-planes is the chief determinant of whether the crystal will be under doped, optimally doped, or create an anomaly (Markiewicz, 1994) within the crystal which will lower the superconductivity transition temperature or at worse make the crystal be a non-superconductor.

It has been shown that the charge density and spin order are critical in the ordering mechanism (Y. Wang & Chubukov, 2014, 2015), and thus for a proper understanding of the influence of doping in the ordering process, the knowledge of the spin, charge, and atomic orbitals are very important.

The orientation of the magnetic moment of the under-doped, optimally doped is a factor of the spin that determines the orientation of the magnetic moment along the CuO_2 plane on the copper hole. In most situations, the doped hole is free to move around the oxygen atoms. At optimal doping, there is strong magnetic ordering which gives rise to the maximum superconducting transition temperature. The pseudo gap region is usually characterized by the antiparallel magnetic ordering for the cuprate superconductors. The periodicity of the order in the supercell crystal setting is always static and thus does not support the superconductivity of the crystal and this can be explained by the fact that the orientation of the CuO bonding is directed to the basal direction of the supercell crystal (Barham & Doetschman, 1992; Nithya & Thiyagaraj, 2020). This behavior implies that the underlying spins in the layers are strongly captured by the antimagnetic ordering. This means that the superconducting states can only be realized by the magnetic ordering of the states.

Some of the properties highlighted above can be explored using the computational modeling of materials technique which has been proved to offer the best way to characterize a material from the first principle. There are so many codes that have been developed to undertake computational calculations in solid-state physics and condensed matter physics.

1.2 Statement of the Research Problem

Research on perovskite materials has led to the discovery of many interesting properties which play a key role in technological application (Assirey, 2019; Fukuhara *et al*., 2010; Ghouch *et al*., 2020; Mumtaz *et al*., 2020). Generally, many perovskites are implemented in the devices we use today. However, many materials which display potentially useful properties have not been fully exploited due to a lack of understanding of their mechanical, electronic, and optical properties and how those properties can be improved to favor diverse applications. It's usual practise to support experimental research with computer studies in order to identify the ideal material of target for a certain application and determine the ideal application conditions.

Among the perovskites of interest are the superconductors such as $GdBa_2Cu_3O_{7-x}$. The perovskite is a superconductor that is desired for both industrial and practical applications. The material can be drawn into long wires with high critical current (J_c) at 77K; it has high magnetic fields (H_C) of 4.2 T; it has the potential to trap magnetic fields up to 2.0 T at 77K and also has low crystalline anisotropy (Leonard *et al*., 2014; W. L. Zhou *et al*., 1994). Elastic properties of the material indicate that it has strong mechanical properties, meaning it can withstand both axial, tensile and compressive strain without getting mechanically damaged (Haberkorn *et al*., 2015; Troitskii *et al*., 2020). However, despite the interesting properties of the material, there is a limitation of the maximum trapped field as a result of the elastic properties of the bulk superconductor. This is as a result of the high magnitude of electromagnetic force that acts on the bulk crystal when subjected to a large trapped field.

The response of the material in terms of mechanical properties to the crystal defects such as cracks and pores is notably high (Antonova *et al*., 2019; Tran *et al*., 2013). This can be attributed to the volume changes that are associated with the polymorphic phase transition from the orthorhombic phase to the tetragonal phase. It is, therefore, important that the material be investigated under different conditions to establish the best conditions for practical application with minimal limitations. The motivation for this study is to explore the effect of hole doping resulting from different effects such as pressure in improving the electronic, structure, superconductivity, and elastic properties of the material. Also, the pressure-induced phase transition will be dealt with.

Although it is very possible to study the properties of a bulk superconducting material experimentally, there is a great challenge to accurately investigate the microscopic properties at very low temperatures. Like $GdBa_2Cu_3O_{7-x}$, most of the high-temperature superconductors are ceramic materials that are characterized by brittle nature. These ceramic materials have many defects and therefore it becomes very difficult to separate the intrinsic and the extrinsic effects on the material experimentally. In solid state physics, bulk properties are important components in determining how the computational results are related to the experimental results. The properties are associated with the lattice constants which form the basic requirement in the computational studies and also determine the experimental values.

1.3 Objectives

1.3.1 Main Objective

To apply computational methods using *ab initio* calculations using the quantum espresso code to investigate the structural, electronic, and mechanical properties of $GdBa_2Cu_3O_{7-x}$ and determine how these properties affect the superconductivity transition temperature of $GdBa_2Cu_3O_{7-x}$.

1.3.2 Specific Objectives

i To investigate the structural and electronic properties of the $GdBa_2Cu_3O_{7-x}$ perovskite superconductor doped phases.

ii To investigate the mechanical properties in relation to stress for $GdBa_2Cu_3O_{7-x}$ under different pressure conditions.

iii To determine how the mechanical and electronic properties affect the superconductivity transition temperature for $GdBa_2Cu_3O_{7-x}$.

1.4 Justification for the Study

Many studies, both theoretical and experimental, have focused on the mechanical and electrical characteristics of perovskite material. Afifi et al., 2019; Ru et al., 2018; N. Zhang, 2020) have conducted studies to investigate the influence of structural and elastic features on the superconducting process in ReBaCuO1. Despite extensive research in the last four decades, there still exists inconsistencies among several outhors in there studies. Therefore, there is a need for further investigations to be done to resolve such inconstancies and to discover new properties for various applications. High magnetic fields and a high critical current density (Jc) are characteristics of ReBa2Cu3O7-x (Re123) high criticaltemperature Tc superconductors. As is well known, two crucial prerequisites for applications in engineering of Re123 superconducting bulks are high Jc and big bulk size, which is associated with the current loop size.

Comparing GdBa2Cu3O7-x to Y123 superconductors, strong magnetic field results in high Jc. Large-scale uses for Gd123 are anticipated to include bulk magnets, magnetic bearings, superconducting flywheels for batteries to store energy, separation of magnetic fields, and motor current lead. Noteworthy for applications in industry are the critical mechanical characteristics of high Tc oxides, as well as the Tc, Jc, and irreversibility fields. Oxide superconductors have intrinsic brittleness and fracture toughness of the material is due to the defects inside superconductors. Therefore, this study seeks to improve the mechanical properties of the material in order to achieve structural reliability for application.

CHAPTER TWO

LITERATURE REVIEW

2.1 Microscopic Theory of Superconductors

The theory explains the phenomenon of superconductivity in terms of bound states. The bound states comprise the paired electrons which against the principles of electrostatics, they attract each other. To explain these, the theory considers paired electrons whose momentum must not be the opposite vectors. Let P and $-P$ be the initial momenta of the electron pairs and P' and $-P'$ be the final momenta of the electron pairs. Considering the Debye radius r_D when the distance of separation of particles in metal is small, the interaction of the electrons is based on the Coulomb repulsion between themselves. This is given by the equation;

$$U_q = \frac{4\pi e^2}{\epsilon(q^2+(r_D)^{-2})} \qquad (2.1)$$

Where $q = \frac{P-P'}{h}$ and, $\mathrm{P}-\mathrm{P}'$ is the change in momentum of the electrons while ϵ is the dielectric constant of the crystal lattice. Equation 2.1 illustrates the effect of the change in momentum in the determination of the repulsion potential.

In addition to the above explanation, the theory also attributes the interaction to be a result of electron-phonon interaction(P. B. Allen & Dynes, 1975; Molinari *et al*., 1992). The quantum Hamiltonian of this interaction explains the absorption and emission of the phonons as explained in the second-order perturbation theory (Gillet *et al*., 2017; Golovach *et al*., 2004). In this case, diagonalization of the matrix in the quantum system is made exact and a large number of phonons are enhanced so that exact energy can be obtained in the expected region. The theory further explains the emission and absorption of virtual photons. The end process results in attractive interaction between the pairs (Fröhlich, 1950).

The scattering amplitude in the second-born approximation is given by equation 2.2 (Holt *et al*., 1971).

$$V = \frac{1}{2}\sum V_{ni}V_{mi}\ \left[\frac{1}{E_n - E_i} + \frac{1}{E_m - E_i}\right] \tag{2.2}$$

Where m and n are the initial and final quantum states, E_i is the ground state energy and the summation includes all the other states. We take the initial and final states as a function of momentum to be presented by $2\varepsilon(P^{\prime})$ and $2\varepsilon(P)$ respectively. The principle of conservation of momentum will only allow the two states. The electron with momentum P will emit a photon of momentum $\hbar q$ and its momentum changes to $P - \hbar q = P^{\prime}$ and thus the energy of the acquired state is given by;

$$\varepsilon(P) + \varepsilon\left(P^{\prime}\right) + \hbar\omega_q \tag{2.3}$$

Where ω_q is the phonon frequency with wave vector q. In the other state, the electron whose momentum is $-P$ will emit a phonon whose momentum is $-\hbar q$ and acquires a momentum $-P - \hbar q = P$ and the energy of the state will remain unchanged. Of interest then is the scattering amplitude resulting from the phonons. This is expressed by the equation;

$$V_{P_1P_1^{\prime}} = \frac{1}{2}|M(q)|^2\left[\frac{1}{\delta\varepsilon - \hbar\omega_q} + \frac{1}{-\delta\varepsilon - \hbar\omega_q}\right] \tag{2.4}$$

Where $\delta\varepsilon = \varepsilon\left(P^{\prime}\right) - \varepsilon(P)$ is the energy absorbed or emitted.

The scattering amplitude is given by:

$$V_{P_1,P_1'} = U_q + |M(q)|^2 \frac{\hbar\omega_q}{(\delta\varepsilon)^2-(\hbar\omega_q)^2} \qquad (2.5)$$

The equation is very important in the interpretation of the phonon spectra in terms of whether the contribution is negative or positive. The contribution is said to be negative if $|\delta\varepsilon| < \hbar\omega_q$ which means that the interaction of the electron pair will be attractive as a result of the contribution from the Coulomb interaction being too small. Further, this means that ω_q is smaller than the Debye frequency ω_D. However, this does not factor in the operation of superconductivity at a low temperature so well. The interaction becomes weak as the superconducting temperature becomes low. When the interaction is weak the bound states fail to exist hence this theory fails to work. Through the work of Cooper 1956 (Pavlidis *et al.*, 2003), it was suggested that this can work on free particles and not those that are in a state of Fermi gas because they exist in the form of Fermi spheres. Free particle is considered to exist in a vacuum space, and the density of the state is always small to allow the existence of bound states because their energy is small. This is completely different from the Fermi gas at $T = 0K$.

To illustrate these two particles existing at the Fermi-sphere, we consider their momenta to be opposed and represented by, $P_1 \; and -P_2$ meaning their total energy must be larger than $2\varepsilon_F$ and they will be in a bound state where $(2\varepsilon_F - E)$ is the binding energy. The boundary separating the bound states from the continuous spectrum is $2\varepsilon_F$ which is larger than that proposed by the mechanical theorem for particles in a vacuum space.

Excitation energy for an ideal gas is achieved by the condition that the particle is transferred from the Fermi surface to a given state of momentum and is given by equation;

$$\varepsilon(P) = \frac{P^2}{2m} - \frac{P_q^2}{2m} \cong v_F(P - P_F) \qquad (2.6)$$

Where m is the mass of the particle, v_F is the Fermi velocity, P_F is the Fermi momentum and the condition of $P < P_F$ must hold.

This works on the assumption that the energy is small. When $P > P_F$, the particle is transferred from a state with momentum to a Fermi surface and the energy is given by;

$$\varepsilon(P) = (\frac{P_E^2}{2m} - \frac{P^2}{2m}) \cong V_F(P_F - P) \qquad (2.7)$$

Taking the potential of interaction to be small, it will mean that the binding energy will also be small such that:

$$U(|r_1 - r_2|) = -g\delta(r_1 - r_2) \qquad (2.8)$$

Where r_1 and r_1 are the distance of particles 1 and 2 and $g\delta(r_1 - r_2)$ is the binding energy. By considering two bound states, the Schrödinger equation can represent the excitation;

$$[\varepsilon(\widehat{P_1}) + \varepsilon(\widehat{P_2}) - g\delta(r_1 - r_2]\psi(r_1, r_2) = (E - 2\varepsilon_F)\psi(r_1, r_2) \qquad (2.9)$$

Where Ψ is the wave function and E is the ground state energy for the system.

The assumption in equation 2.9 is that the excitation energy is defined by the Fermi energy. If the sum of the momentum will be zero, then the quantum mechanical basis set must be invariant (remains unchanged when a specified transformation is applied) with respect to change in space which results to the equation;

$$\psi(r_1, r_2) = (r_1 - r_2) \tag{2.10}$$

So this means that the bound states will always form even when the interaction is weak. If the formation of pairs happens under the influence of energy, then the unpaired particles will never be in the ground state in a quantum mechanical system. To move the paired particles into a higher excitation state, then the pairs must be broken.

2.2 Thermodynamic Properties of a Superconductor

The thermodynamic properties determine the variation of particles at the energy gap with temperature and pressure. At absolute zero temperature the governing equation for the energy gap is given by;

$$\frac{g}{2}\int \frac{1}{\varepsilon(P)}\frac{d^3P}{(2\pi\hbar)^3} = 1 \tag{2.11}$$

Where g is the energy gap and P is pressure.

If the temperature is zero($T = 0$), then the above equation will only have a solution if the integral is over a wide range. As $g_0 \rightarrow 0$ the integral diverges near $n_p = 0$ which means at small g_0 the pressure is approximately equal to Fermi pressure $p \approx P_F$. Then in terms of pressure at the Fermi level, equation 2.11 becomes equation 2.12.

$$\frac{gP_F^2}{2\pi^{2\hbar^{3\hbar_F}}}\int_0^{\hbar\omega_D} \frac{dn_P}{\sqrt{g_0^2+n_P^2}} = 1 \tag{2.12}$$

Where $g_0 = 2\hbar\omega_D \exp(\frac{-2}{gv_F})$

The density of state at the Fermi surface v_F is represented by;

$$v_F = \frac{mP_F}{\pi^2\hbar^3} \tag{2.13}$$

2.3 Thermodynamics of Superconductors in Magnetic Fields

The external magnetic field plays a role in the transformation of material between the normal phase and the superconducting phase (Cbers *et al*., 2005; Karaca *et al*., 2009; Shapiro & Shapiro, 2019). At a relatively higher magnetic field, the material loses superconducting properties due to the penetration of the fields into the material. When the material has zero magnetic fields H_0, the normal conducting state becomes electrodynamically unstable. This only happens below the superconducting transition temperature (T_c) which is pressure dependent. The pressure at which the thermodynamic potential energy (Φ) is lower ensures the stable state of the material at $(H_0$. The degree of the low energy for stability is determined by the Fermi surface energy by the condition that the superconducting transition temperature must be lower than the Fermi surface energy $(\varepsilon_F < T_c)$ (Lugovskoi et al., 2019; Ruhman & Lee, 2016). The thermodynamic potential for the two states is related by the equation;

$$\Phi_s(T,P,H_0) = \Phi_{s0}(T,P) + V_{s0}(T,P)\frac{H_0^2}{8\pi} \tag{2.14}$$

Where $\Phi_{s0}(T,P)$ is the thermodynamic potential at H_0 while V_{s0} is the volume of the superconductor. At the boundary of transition from the normal state to the superconducting state the governing equation of the thermodynamic potential is;

$$\Phi_s(T,P,H_0) = \Phi_{so}(T,P) + V_{so}(T,P) + \frac{H_C^2(T,P)}{8\pi} \tag{2.15}$$

Where $H_C(T,P)$ is the critical transition magnetic field in terms of temperature and pressure $T_C(P)$. As $T \rightarrow T_C\, the\ \ H_C(T_C,P)$=0 and hence the free energy is given by;

$$F_n(T,V) = F_{s0}(T,V) + V\frac{H_c^2(T,V)}{8\pi} \tag{2.16}$$

The equation of the free energy implies that $H_C(T_C, P)$ characterizes the latent heat and the change in volume at the transition boundary. The transition latent heat expressed in terms of entropy given by;

$$S_s = (-\frac{\partial \Phi_{s0}}{\partial T})_P - (\frac{\partial V_{s0}}{\partial T})\frac{H_0^2}{8\pi} \tag{2.17}$$

The volume change under the influence of pressure and the latent heat of transition are given by equations; 2.18 and 2.19 respectively.

$$V_s - V_n = \frac{V_S H_C}{4\pi}(\frac{\partial H_C}{\partial T})_P \tag{2.18}$$

$$S_s - S_n = \frac{V_S H_C}{4\pi}\left(\frac{\partial H_C}{\partial T}\right)_P \tag{2.19}$$

2.1 The Ginzburg-Landau Theory

The theory which was established in 1962 by Ginzburg and Landau gives the characteristic quantitative behavior of a superconductor from normal to the superconductivity transition phase. According to the theory, the free energy increases is described by a superconductivity order parameter ($\wedge$) in which the free energy expansion is given by;

$$F = F_n + d|\nabla \wedge|^2 + A|\wedge|^2 + \frac{B}{2}|\wedge|^4 \tag{2.20}$$

Where F_n is the free energy for the normal state and the coefficients d, A and B are dependent on the temperature and pressure of the material in which A and B must be positive.

For easy computation, a quantity Θ is introduced which must be proportional to the quantity $\wedge$ such that the gradient (∇) in the above equation is proportional to the quantum mechanical kinetic energy.

$$\Theta = \left(\frac{4m}{\hbar d}\right)^{1/2} \wedge \quad (2.21)$$

If the internal energy of the superconducting material is free of any magnetic field (H_0), then the free energy of the superconductor is given by;

$$F = F_n + \int \left(\frac{\hbar^2}{4m}|\nabla\Theta|^2 + A|\Theta|^2 + \frac{b}{2}|\Theta|^4\right)dV \quad (2.22)$$

Where F_n is free energy at Θ=0,

Considering a superconductor of equal uniformity, the above equation becomes;

$$F = F_n + A|\Theta|^2 + \frac{BV}{2}|\Theta|^4 \quad (2.23)$$

To achieve equilibrium of the order parameter the stable state temperature must have minimum energy such that;

$$\frac{\partial^2 F}{\partial \Theta^2} = 2a\Theta \quad (2.24)$$

For a normal state and for superconducting state as;

$$\varepsilon(P) = \left(\frac{P_E^2}{2m} - \frac{P^2}{2m}\right) \cong V_F(P_F - P) \quad (2.25)$$

This works on the condition that Θ is real when $\frac{\partial F}{\partial \theta} = 0, \Theta = 0,$ and $\Theta^2 = -\frac{a}{b}$. Therefore, we expand the order parameter near the boundary of the superconducting transition temperature in the integral power of $(T - T_C)$ such that; when $a = \alpha(T < T_C)$ the number of a superconducting electrons becomes:

$$n_s = \frac{2\alpha}{b}(T_c - T) \tag{2.26}$$

And the superconducting free energy becomes;

$$F_s = F_n - V\frac{A^2}{2B} = F_n - \frac{V\alpha^2}{2B}(T_C - T) \tag{2.27}$$

Thus, the thermodynamic potential energy and the critical magnetic field can be expressed by the equations 2.28 and 2.29 respectively.

$$\Phi_s = \Phi_n - V\frac{\alpha^2}{2B}(T_C - T)^2 \tag{2.28}$$

$$H_C = \left(\frac{4\pi\alpha^2}{B}\right)^{1/2}(T_C - T) \tag{2.29}$$

2.5 Mechanical Properties of Materials

Mechanical properties of a material describe the elastic behavior of a material when subjected to external stress. The thermodynamic properties of a material which are associated with the mechanical properties are well explained if the elastic constant of a material is considered as a function of temperature and pressure. This explains why elastic waves are the most important properties that can explain electron coupling and other mechanisms that are related to mechanical properties. The mechanical properties determine the various phase transition that is possible in a material which includes the superconducting transition temperature and the polymorphic transition temperature. The ultrasonic sound wave normally generates mechanical vibrations in material under consideration which can affect materials in all states of matter. The wave is a summation of the vibrations from all atoms or molecules in the crystalline material. In solid material, we have both longitudinal and transverse waves which are never the case in liquid. The properties are very useful in determining the suitability of a material for various applications.

2.6 Elastic Constants and Elastic Moduli

When the material of a crystalline or amorphous nature is stressed by external forces (stress) which is usually represented by σ_{ij}, it undergoes either elastic or plastic deformation. The kind of deformation depends on the magnitude of the applied force. As a result, the material gets geometry deformation and this is described by the strain tensor usually represented by Hooke's law which relates the two tensors as given in equation 2.30.

$$\sigma_{ij} = C_{ijkl}\varepsilon_{kj} \tag{2.30}$$

The constant C_{ijkl} describes the ability of the material to resist stress and is referred to as the elastic constant of a material. The elastic constant is unique for every material and its value can be used to deduce all the mechanical properties associated with the material. The internal energy of a crystal is also related to the constant and the relationship can be expressed as;

$$U = V_o + V\sum_i \sigma_i\varepsilon_i + \frac{1}{2}V\sum_i\sum_j C_{ij}\varepsilon_i\varepsilon_j \tag{2.31}$$

The properties associated with the elastic constant that are of interest to researchers and industrial applications are Young's moduli *B*, elastic moduli *E*, Poisson's ratio σ, and the shear moduli *G*. The elastic constant is a descriptive term used to represent the linear combination of all the elastic consents in a crystal lattice. The use of averages such as the Reuss and Voigt ensures a better value for the elastic constants to be used in the calculation of the aforementioned properties.

2.7 The Theoretical Strength of a Perfect Crystal

The strength of a crystal and its stress resistance entirely depends on the arrangement of the particles in the crystal lattice when subjected to any stress conditions and the strength is determined by such factor as the elements that constitute the crystal, the type of bonding that bind the elements and the crystallographic structure of the material (Kanel *et al.*, 2004; Panin *et al.*, 2015). A material is considered to be in a state of theoretical stress when its stability is about a transition from stability to instability. This is represented in terms of uniaxial tensile loading σ_{iut}, hydrostatic tensile loading σ_{iht}, and pure shear σ_{is}. Theoretical stress is calculated on the assumption that the strain is directly proportional to stress provided the maximum limit has not been exceeded.

2.8 Mechanical Stability

Mechanical stability can be attributed to the effect of the stress tensor components (Burtch *et al.*, 2018; Karlsruhe & Berichte, 2006; Sureshkumar & Beris, 1995). For a periodic crystal, the central force in the crystal acts through all the neighboring particles. For a three-dimensional structure, the crystal energy is lowered by microscopic deformation resulting from the external mechanical loads and internal thermal stress in what is referred to as soft phonons. The phonons give a full description of the movement of particles in the crystal lattice. Depending on the movement of the particles, the soft phonons can cause dynamic instability which is brought about by the polymorphic phase transition resulting from either temperature or pressure changes.

2.9 Intrinsic Hardness

Intrinsic hardness depends on the type of bonding existing in a material. The bonding determines the magnitude of the elastic moduli and therefore this kind of hardness is calculated from the elastic moduli of the material. It is predominant in the covalent bond and not metallic and ionic bonding. This is because in the two bonding, there exists impurities and grain boundaries which bring about extrinsic factors which make a material not exhibit the intrinsic behavior. Both bulk and shear moduli play a part in determining the hardness of a material (Ding *et al.*, 2004). Vicker which is the measure of the intrinsic hardness of a material is given by;

$$H_V = CK^M G^n \tag{2.32}$$

Where $C, M,$ and N are constants and K is Pugh's modulus ($\frac{G}{B}$), and G and B are the shear and bulk moduli respectively. This only occurs when the electron-electron pair is shifted from the conduction band to the valence band in which case the activation energy becomes twice that of the band gap energy (E_g). This establishes a strong relationship between bond strength and E_g hence the intrinsic hardness is expressed as;

$$IH(GPa) = AN_eE_g = 350\left[(N_e)^{\frac{2}{3}}\exp(-1.191f_i)\right]/2.5d_b \tag{2.33}$$

Where A is a constant, N_e represents the number of the valence electrons per cubic angstrom, d_b is the bond length in angstrom and f_i is the ionicity of the chemical bond.

2.10 Intrinsic Brittleness and Ductility

The mechanical brittleness and ductility of the material give the measure of material to resist fracture. Some of the quantities that are used to estimate this measure are Pugh's ratio and the Cauchy pressure. The criterion varies from one material to the other.

2.11 Materials at High Pressure

The study of materials at high pressure has attracted a lot of attention due to intense scientific and technological interests such as understanding phase transition under pressure and the discovery of superconductors and hard materials. The basic quantity that determines the stability of a given phase in a system is Gibb's free energy which is given by;

$$G = E + PV - TS \tag{2.34}$$

Where E is the energy, P is the pressure, T is the temperature, V is the volume and S is the entropy. For the normal cases of application, P and T are applied externally and E, V, and S are adjustable to attain a minimum value of G. The implication of the equation (2.34) is that upon application of pressure, a structure with a smaller volume will always have a small G even if their energy is of higher magnitude and thus exist in high pressure. When Gibb's free energy becomes the same at two polymorphic phases, a phase transition occurs. If the operating conditions are such that $T = 0$, the pressure-induced phase transition is supposed to be a function of E(V). Apart from the structural changes, materials under pressure also undergo electronic changes. As a result, a material may transform from insulator to conductor, semiconductor to a conductor, or become a superconductor due to the broadening of the energy bands brought about by the interatomic interactions under pressure. As a result, modification of atomic orbitals and the bonding arrangements can occur.

2.12 Pressure-Induced Superconductivity

Superconductors can be divided into two: conventional superconductors and non-conventional superconductors. The mechanism of superconductivity is explained by the Bardeen-Coopers-Schrieffer (BCS) theory. The theory attributes superconductivity to the pairing initiated by phonons and as a result, the pairs behave like a superfluid. Most conventional superconductors are a result of high pressure. These non-conventional superconductors are not described by the BCS theory. The pressure-induced doping in these superconductors can improve the T_C and thus make them better high-temperature superconductors especially in the cuprate superconductor. For insulators and semiconductors, pressure may cause the band gap to close and the material to undergo metallization.

2.13 Historical Background of Superconductivity

Superconductivity is a phenomenon where the material becomes free of electric fields and magnetic field and hence becomes a perfect diamagnetic material below a critical temperature (Rosenstein & Li, 2010) and thus achieve zero resistance to electrical conductivity. This happens because of the stability of the charge carriers that have zero resistance to electrical conductivity. In his discovery of superconductivity in 1911, Heike Kamer-Lingh (Delft & Kes, 2010) realized the electrical conductivity of mercury dropped to zero after subjecting the material to a temperature of 4.2K.

In 1933, Walther Meissner and Robert Schoenfeld discovered the diamagnetic nature of type I superconductors. They found that magnetic fields are completely expelled from the interior of the superconductor once the superconductor achieves the superconducting state (Hirsch, 2017; Manuscript, 2020). The Meissner effect, which is this feature, proved that superconductors are not simply ideal conductors since superconductivity needs a vital temperature and vital current in addition to magnetic fields. The nature of the expulsion of the magnetic field can be considered in terms of type-I superconductors and type-II superconductors. In type-I superconductors, the superconductivity vanishes rapidly upon exceeding the critical magnetic field (H_c). In type-II superconductors, once the applied field exceeds the H_{c1} the material attains a vortex state in which further application of the magnetic field does not lead to zero electrical resistance provided the flowing current is small in magnitude (Babaev & Speight, 2005; Qd & Qd, 2003). At the second critical magnetic field H_{c2} leads to the destruction of the superconductivity. Most of the type-I superconductors are pure elements while the type-II comprises mainly of the impure compound superconductors and thus the $GdBa_2Cu_3O_{7-1}$ belongs to this category of materials.

In 1935 Fritz and Heinz London proposed the London theory which brought forth equations that were consistent with the Meissner effect (T he E Lectro m Ag n Etic E q u a Tio n s o f Th e S u p Ra c o n d u c to *R*, 1934). The equations explain how the field of magnetic particles as well as surface current rely on the superconductor's distance from its surface when combined with Maxwell's equations. These electrodynamics properties depend on two- fluids; the normal fluid and the superfluid concentrations whose sum is the total fluid representing the total number of electrons in the system such that: $n_s + n_n = n$ (Barišić *et al*., 2010). Where n

is the total number of conducting electrons per unit volume. The normal fluid is thought to carry the ohmic current and is described by;

$$j_n = \sigma_n E \tag{2.35}$$

Where σ_n is defined by Drude's theory and given as $\sigma_n = \frac{e^2 n_n \tau}{m}$. and E is the electric field. On the other hand, the superfluid ohmic current for a superfluid is given by;

$$j_s = -en_s V_s \tag{2.36}$$

Then the first London equation is obtained from Newton's law of motion given by the equation 2.37 and 2.38 respectively.

$$\frac{d}{dt} v_s = \frac{F}{m} = \frac{eE}{m} \tag{2.37}$$

Thus we get,

$$\frac{\partial j_s}{\partial t} = \frac{e^2 n_s E}{m} \tag{2.38}$$

The assumption of the first London equation is that n_s and n_n are constant in terms of time and space. The restriction is only solved by the application of the Ginzburg-Landau theory. Taking the curl of the first London equation to be given by equation;

$$\frac{\partial}{\partial t} \nabla \times j_s = \frac{e^2 n_s}{m} \nabla \times \mathrm{E} = -\frac{e^2 n_s}{mc} \frac{\partial B}{\partial t} \tag{2.39}$$

Which upon integration gives;

$$\nabla \times j_s = -\frac{e^2 n_s}{mc} \mathrm{B} + \mathrm{C(r)} \tag{2.40}$$

Where C(r) represents the constant of integration at each point within the superconductor.

When there is no application of magnetic field in a superconductor, the $j_s = 0$ and $B = 0$ meaning the constant becomes zero. According to the Meisner-Ochsenfeld effect, the material can only become a superconductor within some applied magnetic field which cannot apply in the case of the London theory based on the fact that the electron density of the superfluid n_s is constant with time as given in equation (2.40). For equation 2.40 to work, London made an assumption letting C(r) be zero as expressed in equation 2.41 such that;

$$\nabla \times j_s = -\frac{e^2 n_s}{mc} B \tag{2.41}$$

In the second London's law, Ampere's law is incorporated and led to the equation;

$$\nabla \times B = \frac{4\pi}{c} j_s + \frac{4\pi}{c} j_n \tag{2.42}$$

If the current does not undergo displacement, then;

$$\nabla \times \nabla \times B = -\frac{4\pi e^2 n_s}{mc^2} B + \frac{4\pi}{c} \sigma_n \nabla \times E = -\frac{4\pi e^2 n_s}{mc^2} B - \frac{4\pi}{c} \sigma_n \frac{\partial B}{\partial t} \tag{2.43}$$

Since the interest is in the stationary state, the last term can be omitted, and we get;

$$-\nabla(\nabla . B) + \nabla^2 B = -\frac{4\pi e^2 n_s}{mc^2} B \tag{2.44}$$

If we take the London penetration depth to be given by the equation;

$$\lambda_L = \sqrt{\frac{mc^2}{4\pi e^2 n_s}} \tag{2.45}$$

Then,

$$\nabla^2 B = \frac{1}{\lambda_L^2} B \tag{2.46}$$

If we let the penetration depth be presented by x and we let $x > 0$, the applied magnetic field becomes parallel to the surface and can be presented as;

$$B_{apl} = H_{apl} = B_{apl}\hat{y} \tag{2.47}$$

And if $x \geq 0$ the governing equation becomes;

$$B(x) = B_{apl}\hat{y}e^{\frac{-x}{\lambda_L}} \tag{2.48}$$

The equation implies that there is an exponential decrease in the magnetic field with the penetration depth from the surface of a superconductor. For bulk superconducting materials $B \to 0$ as the depth increases as shown in Figure 2.1.

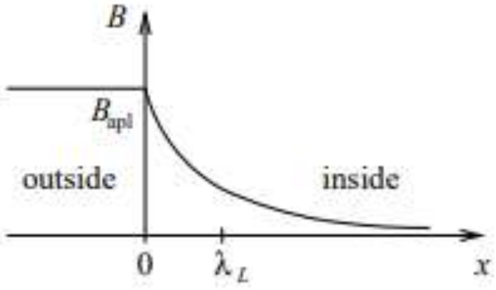

Figure 2.1: The variation of the penetration depth with the magnetic field.

This London penetration depth indicates an exponential decay of the applied magnetic field from the surface of the superconductor to the interior of the superconductor. This behavior is associated with the density of the superconducting electrons in the superconductor. The

London equation gave an elaborate explanation of the way the superconducting particles behave in electronic fluid when subjected to either the dc or ac electromagnetic field. However, by 1940 it was discovered that the theory failed to explain one key thing; the negative surface energy the theory predicted for a bulk superconductor $\boldsymbol{\sigma_{n_s}}$. The implication of such assumption was that when the superconductors are subjected to an external magnetic field, the external magnetic field could lead to a reduction of the total energy hence leading to an interchange between the normal and the superconducting regions within the material. The reported experimental results indicated that for such interchange to occur for the normal and superconducting regions the material must have a demagnetization factor of greater than zero. Also, another contradiction arose from the fact that for thick layers (~1mm) the surface energy is greater than one ($\boldsymbol{\sigma_{n_s} > 0}$).

Ginzburg and Landau created a phenomenological theory in 1950 that was effective in explaining the superconductivity's microscopic feature taking into account the quantum theory (Mayssara A. Abo Hassanin Supervised, 2014). They assumed there was some wave function(Ψ) that gives a full quantum mechanical description of a particle, say an electron. With that, amplitude squared of the function is supposed to be proportional to the superconducting electron density (n_s) and must be equal to zero in the normal region and will continue to increase through the normal-superconducting interface and finally have a state of superconductivity in the superconducting region. The implication of this is that Ψ can only describe the quantum mechanical properties when it takes the value it attains at equilibrium. Considering the fact that the density of kinetic energy in quantum mechanics is described by $|\Psi|^2$, then the effect of quantum mechanics results in additional energy that is stored at the interface which leads to the establishment of the surface energy to be greater than zero ($\sigma_{n_s} > 0$). The Ginzburg-Landau theory considers the full description of the superconductors to be based on quantum mechanics. As such, it assumes that the superconducting electrons can be fully described by a wave function of the spatial coordinates described by $\Psi(r_1 r_2, \dots \dots .. r_n)$. This explains the coupling aspect of the superconducting electrons. Since the single electron in the superconducting state is described by $\Psi(\mathrm{r})$ and assuming the superconducting electrons are described by n_s and all of them are free of interaction, then a wave function of a single electron can be used to give a full description of the whole system. This allowed the use of the superconductivity quantum effect while observing the macroscopic characteristics of the material.

Abrikosov applied the Ginzburg–Landau theory and as a result, he came up with a theory of type II superconductors which proved that $\sigma_{n_s} > 0$ was not a necessary condition for all superconductosr (Abrikosov, 1957). According to the theory, the materials that must achieve this condition to superconduct are the type I superconductors and indeed it was proved that most alloys have $\sigma_{n_s} < 0$ and are type II superconductors. The theory further explained that superconductivity in type two supeconductors does not depend on the Meissner effect, meaning that magnetic fields penetrate into this material through quantized vortex lines which can be described as a quantum effect on the macroscopic scale.

In 1957, Bardeen Coopers and Schrieffer established a microscopic theory of superconductivity (Schrieffer, 2018). According to the theory, superconductivity is treated as a microscopic effect caused by the condensation of the Cooper pairs which interact within a distance of a microscopic scale. For the pairs to form an attractive interaction the electrons must exist at the ground state of a superconducting material. This is made possible by the exchange of the virtual phonons which give an attractive energy range around the Fermi level. In some cases, the attractive energy may be dominant over the Coulomb repulsion. The related states in non-superconductors possess less condensation energy in comparison with the superconducting states. The theory also applies the concept of nuclear physics to illustrate how nucleons interact in an atomic nucleus quantum theory explaining superconductivity.

The materials classified as superconductors with high temperatures (HTS) have a superconducting temperature of transition (Tc) greater than 30K, or -243oC. Thirty-k was considered the maximum theoretical value of T_c from 1960 to 1980. In ceramic lanthanum and barium oxide at 35 Kelvin, researchers Karl Muller and Johannes Bednorz of IBM developed the first high T_c superconductor in 1986. 2008 saw the discovery of Fe-based superconductors, replacing the cuprite compound as the association for a high-temperature superconductor till then. HTS are type II superconductor that allows magnetic fields to penetrate their interior in quantified units and fields are required to suppress superconductivity.

In the 1959 Gor’kov made more development on the microscopic theory of superconductivity by explaining the use of the Green’s function to solve the BCS problem. The method was successfully applied in explaining the phenomenological quantum parameters explained in the Ginzburg–Landau theory and giving the proper microscopic interpretation. It also gave the range in which the theory can be accurately applied without a large margin of error.

In the year 1964 Ginzburg came up with non–phonon mechanism of superconductivity that could be applicable on the low–dimensional (1D and 2D) systems only. According to him, substation of the phonons with excitons can lead to an increase of T_C to the scale of up to 50-500K.

In the year 1984, Brizhik and Davydov designed the soliton (or bisoliton) model of superconductivity. The model was capable of explaining the superconductivity in low dimensional (quasi-1D) organic conductors. This was a development from the work of J´erome *et al* who discovered organic superconductors in the year 1979.

Based on the 1979 discovery of superconductivity in heavy fermions, Miyake et al. (1986) identified the mechanism of superconductivity as the interchange of antiferromagnetic spin fluctuations. Their work showed that the anisotropic even-parity nature of the superconductors is not aided by the antiferromagnetic nature of the material while the isotropic even-parity nature is done by the spin fluctuation. The same year the history of superconductivity got a boost when the first high temperature superconductor was discovered by Bednorz and Muller, but unfortunately, the BCS theory was not able to explain most of the properties that were associated with the superconductors.

In the year 1987, Krezin and Wolf came up with a model that explained superconductivity on the basis of the superconducting energy gap and the pressure induced energy gap in layered superconductors. Even though the experiment that was done shortly after that discovery showed that the two gaps existed, still both of them were considered to be of the superconducting origin.

In the year 1988, Davydov attributed the cause of high temperature superconductivity to the formation of bisolitons and the condition occurs in organic superconductors only. In the year

1990, he came up with a theory of high temperature superconductivity based on strong electron phonon coupling. The theory bases it argument on the concepts of the bisolitons (hole) pairs coupled with a single state due to the distortion of the –O-Cu-O-Cu- chain in the CuO_2 planes. In the year 1990, Anderson made an assumption that in the cuprates the mechanism for coupling and formation of phase coherent are different. That year theorists explained the coupling mechanism that has a different origin but the origin of the long range phase coherence can be attributed to the spin fluctuation within the cuprate superconductors. In the year 1994, Alexandrov and Mott established that there was a difference between the wave function that describes the Cooper pairs and the order parameter of the Bose-Einstein condensate whose symmetries vary.

In the year 1995, Emery and Kivelson demonstrated that long range phase coherence was a requirement for the mechanism of superconductivity in the cuprates. They further demonstrated the possibility of coupling above the T_C without phase coherence. In the same year, Tranquada *et al* discovered the existence of coupled, dynamical vibrational charges (holes) and spins in Nd-doped $La_{2-x}Sr_xCuO_4$ cuprate superconductor by application of the neutron diffraction technique.

In the year 1997, Emery, Kivelson, and Zachar formulated a theoretical model of the HTSC that was basing superconductivity on the strips of charge in the CuO_2 planes.

In the year 1998, Chakraverty *et al* tried to disapprove of the theory of the bi-polaron superconductivity of HTSC by stating that it was contradicting the experimental concepts on the same but failed to prove the same.

In the year 1999, Mourachkine established another theory of HTSC, in which he did an analysis of neutron tunneling and neutron scattering measurement and proved that in $Bi_2Sr_2CaCu_2O_{8+x}$ and $YBa_2Cu_3O_{6+x}$ the phase coherence is as a result of spin excitations which leads to the formation of magnetic resonance peaks in inelastic neutron scattering spectra. The same year, Cronstrom and Noga came up with a new way of solving the BCS theory, by means of approximating the mean field which proved the existence if superconducting films and layer superconducting bulks.

In the year 2001, Kivelson came up with a new way of increasing the superconductivity transition temperature. He proposed the creation of a multilayered HTSC having different concentrations of charge carriers in each layer. In this case, the layers with a low concentration of the carriers will be responsible for coupling while the one with a high concentration of the charge carries will be responsible for the phase rigidity. The coupling interactions become weaker while the concentration of the charge carriers is increased in relation to the Mott’s dielectric while the superfluid density which is responsible for the rigidity of the HTSC as related to the phase fluctuations increases with the increase of the charge concentration. Meaning the maximum T_C is achieved at the state where there is equal prevalence for the phase fluctuation and coupling interactions.

Cui 2002, proposed the relativistic mechanism of superconductivity. According to him, there exist two ways that determine the movement of the electrons in a superconductor which results in suppression of the electrons-electron repulsion and coulomb-coulomb repulsion and instead leads to predominant attraction. The free movement of these charge carriers results in superconductivity in the HTSC superconductors in what is referred to as electron gas because of the balance between the attraction and repulsion of the electrons which leads to the theory of non-interacting particles in superconductivity. In the same year, it was shown that the cuprate HTS in the undoped regime are considered as non-dielectrics with high superconducting energy gap and small super-fluid density which then were referred to the gossamer superconductors. In this superconductor the brittle characteristic resulting from their coupled state hinders superconductivity. In the year 2004, Hussey *et al*, while investigating the angle of oscillation between the magnetic resistance in the HTS $CuO_{6+\delta}$, discovered that 3D superconductors exist in such superconductors. This was proof of coherency against incoherency in the c direction of the layered superconductor.

In the year 2004, another universal scaling relationship that characterizes both the normal and the superconducting state was discovered by Homes in which the expression that governs superfluid component was given as $\rho_s = AS_{dc}T_c$ (Homes *et al*., 2004). where S_{dc} is the static specific conductivity and T_c is the critical temperature and this was supposed to be carried out for all the HTS, with disregard to the magnitude of the T_c , the type of carriers involved whether (holes or electrons), the extent of doping done, the nature of the crystal structure and the direction of current which is determined by the CuO_2 planes and they are usually parallel or perpendicular in orientation. The value of the proportionality factor depends on the units of measurement involved. If the ρ_s is measured in s^{-2}, S_{dc} in $(\Omega\text{cm})^{-1}$ and T_c is K, then it takes the value of 120 ± 25. The relationship applies even in superconductors operating at very low temperatures. The dependence is anisotropic in nature in such a way that the value of ρ_s may differ from one direction to the other, especially in the *c* axis.

In the year 2007, Alexandrov again explained the physics behind HTS in terms of the bi-polarons mechanism (Hague *et al.*, 2007). According to him, the HTS behaviors are different from those of a usual metal by the way that only quasi particles transfer current. For the metals, the mechanism of magnetic superconductivity exists, but the subsequent electron phonon coupling does not exist.

2.14 Mechanism of Superconductivity

The mechanism of superconductivity is associated with spin fluctuations within the atoms in the superconducting material. The mechanism can be explained using the following concepts.

2.15 Cooper Pairs Effect

When a material is subjected to very low-temperature equivalent to or less absolutely zero Kelvin, its electrons merge in twos to form cooper pairs. In most cases, this can be attributed to high pressure. The formed pairs are always free from collision with each other, and cannot be deviated even in the presence of impurities within the material. This makes their movement to be of zero electrical resistance. In metals and semiconductors of narrow band gap, the paired electrons always remain in a stable path even with the repulsion existing because they are of the same electrostatic kind. The explanation for this was given by Leon Coopers, Robert Schrieffer, and John Bardeen in what is referred to as BSC theory. The stability results because of two reasons:

Firstly, the presence of other electron ions in the lattice acts as a shield to prevent more repulsion and scattering. Secondly, phonon which temporarily distorts the lattice during vibrational modes may create regions with positive ions that will end up attracting the electron pairs. For this to happen the electrons must possess more kinetic energy than the phonon ions. For this reason, the BCS theory fails to explain superconductivity in high-temperature superconductors such as cuprate ceramics. The superconducting properties of the materials can only be attributed to the structure of the material which has a layer and there exists the hopping ions along with them later.

2.16 Landau Theory

This explains the dependence of superconductors on magnetic flux. The theory explains the variation of the magnetic flux with the penetration depth in a lattice. This can be represented in equation 2.49 before tunneling and equation 2.50 after tunneling.

$$\varphi_0 = \frac{hc}{2e} \tag{2.49}$$

$${}^{\varphi} = \left(n + \frac{1}{2}\right)\frac{hc}{2e} \tag{2.50}$$

where$(n = 0 \pm 1 \ldots\ldots\ldots..)$

This theory was followed by the Josephson tunneling theory in which the superconductors are assumed to form barriers between the lattice of the nearest neighbors and the cooper pairs tunnel between the barrier. The critical current at the superconducting state is given by:

$$J_c = J_o + \Delta J(\Delta^{\varphi}) \tag{2.51}$$

Where $\Delta^{\varphi} = {}^{\varphi}{}_2 - {}^{\varphi}{}_1$ is the difference between two phases at a length of separation of the tunnel barrier.

$$\Delta^{\varphi} = {}^{\varphi}{}^0_2 - {}^{\varphi}{}^0_1 - (2e\text{ђ}C)\int_1^2 dxA_x \tag{2.52}$$

The cooper pairs current at $A = 0$ and the voltage V are calculated as:

$$J_c = J_0 + J_1 \sin(\varphi_2^0 - \varphi_1^0 - \frac{2e}{\hbar} V_{21} t) \qquad (2.53)$$

where $V_{21} = \frac{\hbar}{2e} \varphi_{21}$

The penetration influence below B_{C2} and due to the Meissner effect below B_{C1} can be attributed to the external field due to the cooper pairs held by the critical magnetic fields. The type II superconductors with magnetic penetration flux B_{C2} and Meissner effect below B_{C1} is, as a result of external fields on the cooper pairs shown in Figure 2.2.

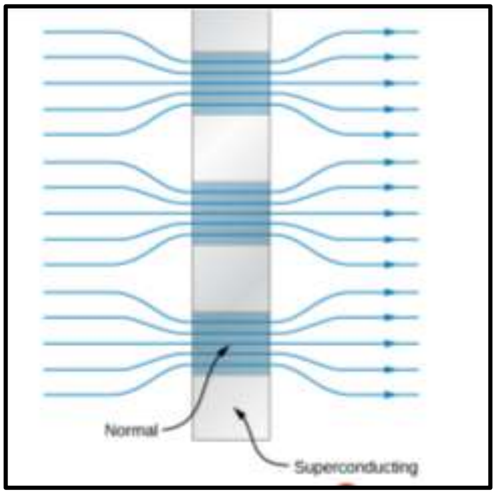

Figure 2.2: A diagram indicating the superconducting state free of magnetic field and the normal state with magnetic fields. (Single-Slit Diffraction – University Physics Volume 3, n.d.).

Type II superconductors are characterized by B_{C1} and B_{C2} magnetic fields while type one is characterized by B_{C1}. At Hci type two superconductors are in a mixed state while type I are pure superconductors.

The above behavior illustrates the strong link between superconductivity and magnetic behavior. For practical application, superconductors whose magnetic behavior grows proportionately are preferred. For high transition temperature superconductors, the T_C can be calculated from Mc Millan’s equation.

$$T_C \propto < \omega_{ph} > exp\left\{\frac{-1}{\lambda} - \mu^*\right\} \tag{2.54}$$

Where μ^* is the characteristic effective Coulomb interaction between the paired electron. Electron-phonon coupling parameter is used to characterize superconductor semi metals and metals by using the density of states at the Fermi level (ε_F).

$$\lambda = 2\int_0^\infty \frac{\alpha^2 F(\omega)}{\omega} d\omega \tag{2.55}$$

where $F(\omega)$ describes the phonon modes.

2.17 Novel Superconductors

The popular classes of novel high-temperature superconductors are cuprate superconductors. Their discovery was a milestone because of their practical capability. Among the first ones to be discovered were: $La_{2-x}Sr_xCuO_4$ and $YBa_2Cu_3O_7$ by Bearnoz and Muller in the year 1986 (“Examination of Patent Applications That Include Claims Containing Alternative Language,” 2007). Higher T_C ranging from 35K to 160K was achieved when these materials were subjected to high pressure in $\mathrm{HgBa_2CaCu_2O_{7-x}}$ (Physical Properties of Tissue: A ... - Google Books.)

The materials portray very unique characteristics which include: an abrupt change in behavior by varying the hoping oxygen concentration in the $\mathrm{CuO_2}$ plane in the layered structure, lack of Fermi liquid behavior, and structural phase transition.

The dependence of $\mathrm{T_C}$ on the oxygen concentration is an indicator that the phase changes which result from the fluctuation of the cooper pairs especially for under doped cuprates which are proportional to the quasi- particles as shown in the equation:

$$T_C \alpha n_s \tag{2.56}$$

Where n_s denotes how the variation of atomic concentration (doping) and depends on the superfluid density. This can also occur when a material is subjected to electron doping. Experimental and theoretical reports have shown that increasing the oxygen concentration increases the hole concentration but will decrease again due to the disappearance of the antiferromagnetic excitation of the spin. It should be noted that doping by the introduction of electrons (electron doping) in the d-orbitals of copper disorients the Cu-spins while varying the oxygen concentration (hole doping) at the p-orbitals destroys the long-range anti-ferromagnetism hence improving the carrier transport for this group of materials (C. Chan *et al*., 2017).

2.18 Related Studies In Re123 Superconductors

The finding of the LaBaCuO superconductor ceramic system, which has a critical transition temperature between 30 and 40, led to the synthesis of other families of copper oxide-based ceramics that have elevated critical temperatures (Alecu, 2004). These oxides include the YBaCuO series (T_c=90K), the BiSrCaCuO series (T_c=80-115K), and the TiBaCaCuO T_c=85-125K.

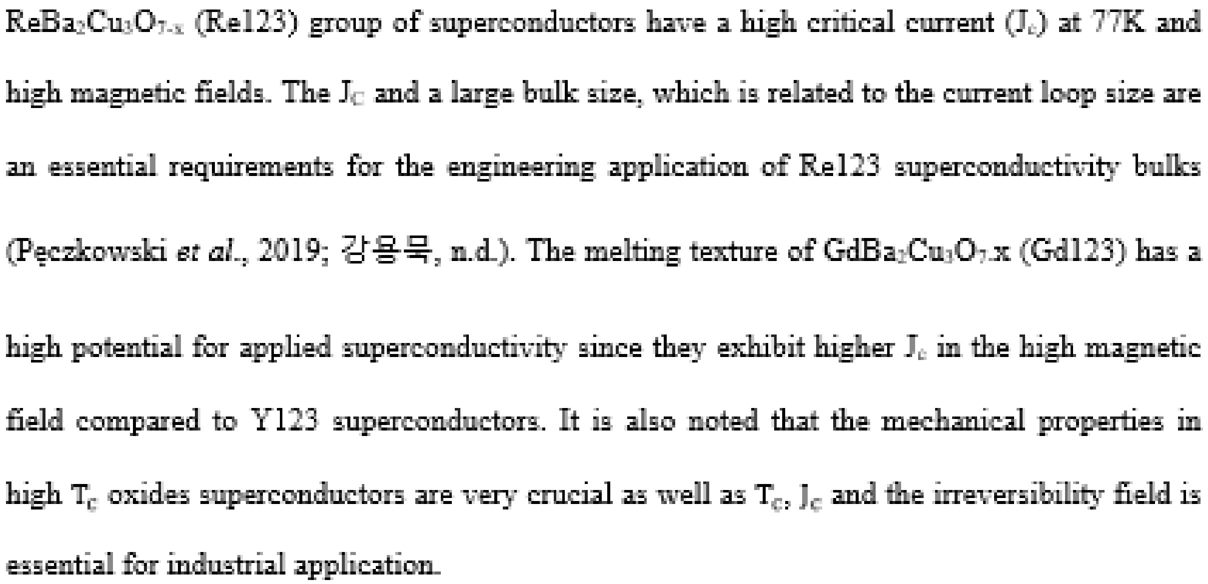

ReBa$_2$Cu$_3$O$_{7-x}$ (Re123) group of superconductors have a high critical current (J_c) at 77K and high magnetic fields. The J_C and a large bulk size, which is related to the current loop size are an essential requirements for the engineering application of Re123 superconductivity bulks (Pęczkowski *et al.*, 2019; 강용묵, n.d.). The melting texture of GdBa$_2$Cu$_3$O$_{7-x}$ (Gd123) has a high potential for applied superconductivity since they exhibit higher J_c in the high magnetic field compared to Y123 superconductors. It is also noted that the mechanical properties in high T_C oxides superconductors are very crucial as well as T_C, J_C and the irreversibility field is essential for industrial application.

Second generation (2G) high-temperature superconductivity HTS wires, also known as coated conductors (CCs), have the potential to significantly transform the electric power industry by enabling the creation of environmentally friendly devices with high efficiencies and smaller sizes and footprints (Arute et al., 2019; Sung et al., 2008). ReBa2Cu3O7-x superconducting coating on textured metallic templates with functional buffer layers makes up 2G HTS wires.

According to (Goldacker *et al.*, 2014; Senatore *et al.*, 2016) the availability of ReBaCuO second-generation high-temperature superconductor (2G HTS), can revolutionize novel electric machines and devices such as powerful motors, generators, and transformers. Improvement can be made in $\mathbf{J_c}$ versus magnetic field performance of the 2GHTS wires through the replacement of the other rare metals with gadolinium.

2.19 Properties of High T_C Superconductors

Superconductivity is majorly characterized by the superconductivity transition temperature. Apart from the transition temperature, there are other factors that also contribute to the processes of superconductivity. They include; the critical magnetic field, penetration depth, coherence length, critical current density, weak link, and the energy gap.

2.19.1 Anisotropy

Almost all crystal structures of high temperature superconductors are highly anisotropic (Ando *et al*., 2002; Van Harlingen, 1995). This property plays a better role in both the physical structure and also the mechanical structure properties that are associated with superconductivity. The charge carriers in high temperature superconductors are usually holes that are brought about by the hopping oxygen in the crystal when that crystal is subjected to the conditions that will favor such hoping. This happens in the CuO_2 plane. The flow of electricity in such a plane is highly anisotropic in which conduction parallel to the CuO_2 plane experience more electricity than in the direction normal to the plane. Also, other properties such as; penetration depth, and energy gap are also anisotropic in nature. The elastic properties of high temperature superconductors and associated mechanical properties are also anisotropic. The anisotropic factor in these high temperature superconductors, when they are optimally doped has a relationship with the spacing between CuO_2 and the layers in the crystal of the unit cell. However, the anisotropy in these superconductors can be reduced by; doping by either applying pressure or varying the ion concentration of some of the elements within the compound of the materials.

2.19.2 Energy Gap

The energy gap is a characteristic feature that is associated with all high temperature superconductors (Rieck *et al.*, 1990, 1995). The energy gap exists in the low energy excitation within the crystal structure of the superconductor. In any superconductor, external energy ($E \geq 2g$), where g is the energy gap, must be provided to move the electron-hole pair close to the Fermi surface. For the BCS high temperature superconductors that are weakly coupled the energy gap is related to the superconductivity transition temperature at 0K (Monthoux *et al.*, 1992; P. Monthoux, A. V. Balatsky, 1992; Rieck *et al.*, 1995). The relationship is expressed by the equation;

$$\frac{2g(0)}{K_B T_c} = 3.52 \qquad (2.57)$$

Where K_B is the Boltzmann constant.

Anisotropy in terms of the energy gap is also observed in these superconductors in which the gap value along the c axis and the $a - b$ plane are noticed. For example for the YBCO, a ratio of $\frac{2g(0)}{K_B T_c}$ has been found to be ~3.5 when tunneling normally to the Cu-O plane and ~6 when tunneling parallel to the Cu-O plane.

Also, experiment done using the magnetic resonance and photoemission measurement in the regime of under doping of the high temperature cuprates superconductors indicated the existence of an energy gap in the spin excitation state. The pseudo gap which is a major characteristic of superconductors occurs well above the superconductivity transition temperature. The experiment further indicates that a spin gap is not found in the optimally doped cuprate superconductors.

2.19.3Critical Current Density and Weak Links

Apart from the superconductor transition temperature (T_c) and the critical magnetic field (H_c), the critical current density (J_C), and weak links also play a major part in determining the transition from normal to the superconducting state of the superconductors. At the time of the discovery of the high temperature superconductors it was found that for bulk T_c materials, the current density is supposed to range from 10-100 A/cm2 at 77K. This was remarkably small in magnitude and was basically dependent on the method of synthesis of the superconductor. The low critical current density was attributed to the natural grain boundaries whose behavior was likened to the Josephson weak link. The Josephson weak link is basically localized regions within a superconductor where the superconducting properties of the superconductor get degraded. The effects of the weak links in critical current for the high temperature superconductors are different from that of low temperature superconductors. In the low temperature superconductors the weak link, the defects associated with the grain boundary increases the spinning effect and therefore increase the critical current but for the polycrystalline high temperature superconductor the grain boundary leads to reduction in the magnitude of the critical current. In high temperature superconducting materials where grain boundaries are absent, the critical current has been observed to be high in magnitude.

2.19.4 Critical Magnetic Field

The transition from normal to a superconducting state is defined by not only the transition temperature but also the magnetic field strength. The critical magnetic field is the field beyond which the superconductivity ceases to exist. For example, if a paramagnetic material is placed in a magnetic field, the magnetic lines of force will penetrate through the material. But when the material is subjected to very low temperatures such that it acquires the superconducting properties, the magnetic lines of force get expelled from the interior of the superconducting material. The effect is called the Meissner effect. According to the Meissner effect materials can be considered as either type I superconductors or type II superconductors. Type I superconductors are characterized by a sharp transition from the superconducting state to the normal state when subjected to an external field. For type II, there are two types of critical fields, lower (H_{C1}) and upper (H_{C2}). The material only transforms from a superconducting state to a normal state at H_{C2}. The difference between the two fields is considered to be a mixed state.

2.19.5 Penetration Depth

Below the lower critical field (H_{C1}) the external magnetic fields are completely expelled from penetrating into the superconductor due to the fields created by the super-current in the surface region, which induces a field that is exactly the same or greater than the applied field. The penetration depth is then considered to be the depth of the surface and the external field penetrates this surface in a decaying manner. For a material that is isotropic in nature, the relationship between the lower critical field and the penetration depth is given as;

$$H_{c1} = \frac{\Phi_o}{\lambda^2} \tag{2.58}$$

Where Φ_o is the flux quantum.

Flux decoration and magnetic torque experiments have established the anisotropic nature of the penetration depth in high temperature superconductors. For these types of superconductors, the penetration depth along the c axis is different from those in the $a - b$ plane. For example, YBCO single crystal, the value of $\lambda_{ab}(T \rightarrow 0)$ is found to be 1400Å.

2.19.6 Coherence Length

Coherence length describes the performance of a superconductor and it tells the correlation of the charge carrier in a superconducting medium. This means that it represents the magnitude of the cooper pairs. It can be presented in terms of the Fermi velocity (v_F), the superconducting transition temperature T_c, Boltzmann constant kB, and Planck's constant h as:

$$\xi = \frac{hv_F}{2\pi^2 k_B T_c} \tag{2.59}$$

From equation 2.59, it can be inferred that the high T_C recorded in the high temperature superconductors is supposed to correspond to the low value of coherence length. This is observed in the cuprate superconductors which record low values of coherence length. The value of coherence length has been found to be very highly anisotropic for the high temperature superconductors. For example, the coherence length parallel to the c axis for a typical high temperature superconductor has a range of 2-5Å and in the plane a-b it has a range of 10-30Å. This means that normal to a-b plane the wave function is in an actual sense confined to the few adjacent unit cells. However, when considering the low temperature type I superconductors, it is found that the coherence length is $> 1000\acute{\text{Å}}$ which is far much high than the range of the high temperature superconductors. When the value of the coherence length is low like in the case of the high T_C, it means the coherence volume will contain a few cooper pairs which further means the fluctuation of the cooper pairs will be larger in these superconductors than in the conventional superconductor. Low coherence length makes a material to be sensitive to the available defects in the crystal such as the oxygen vacancies, dislocations, and deviation from the stoichiometry which promotes the phenomenon of superconductivity.

2.20 General Properties of Superconductivity

An electric field $\vec{\mathrm{E}}$ in a metal establishes a current. The current density $\vec{\mathrm{J}}$ and the electric density field are related by Ohm's law:

$$\vec{J} = \sigma\vec{E} \tag{2.60}$$

σ represents the electric conductivity. Electrical resistivity, ρ, is the reciprocal of conductivity. In metals, the charge carriers are the electrons. Electrons and discrete modes of vibration in lattices of crystals (phonons) collide intrinsically to provide resistance to electrical conduction in metals, while electrons conduction and defects and impurities within the crystal lattice collide extrinsically to produce resistance to conduction of electricity.

The resistivity as described by Matthiessen's rule is given by the equation 2.61.

$$\rho = \rho_L + \rho_i \qquad (\ 2.61)$$

Where ρ_L is resistivity due to electron-phonon scattering and ρ_i is resistivity from imperfections. In general, resistivity decreases with decreasing temperature in conductors. A superconductor exhibits zero resistance for direct current; an ordered state of electron pairs is responsible for the supercurrent. As conductivity tends to infinity for finite J, $\rho \rightarrow 0$, electrical conduction is not described by Ohm's law in superconductors. Instead, in the absence of an applied magnetic field, certain materials become superconducting when the temperature is lowered to a specific value called the critical temperature T_c where the superconducting state magnetic induction $\vec{B} = 0$. The expression of the magnetic field does not come as a natural consequence of perfect conductivity. It is shown that:

$$\lambda^2 = \frac{m}{\mu_o n e^2} \qquad (2.62)$$

And the solution for the equation is:

$$\frac{\partial \vec{B}(Z)}{\partial t} = \frac{\partial \vec{B}}{\partial t} e^{-Z/\lambda} \qquad (2.63)$$

Where the constant λ is the penetration depth and Z is the distance from the surface of the conductor. This result implies $\vec{\mathrm{B}}$ is a constant in the interior of the perfect conductor but not necessarily zero. If a perfect conductor was in a magnetic field and then reached a perfect conducting state, that magnetic flux is maintained inside the material. In a superconductor, the magnetic flux density is always zero.

Not only $\frac{\partial B}{\partial t} = 0$ but $\vec{B} = 0$ at all times inside the superconductor. Values of the random penetration depth are on the order of 100nm. On the surface of the superconductor, a current is formed which generates a magnetic field to exactly cancel any effect that the external applied magnetic field has inside the superconductor.

2.21 General Properties of Perovskites

These are compounds with the general formula of ABO_3 and the structure of a simple crystal of the perovskite material is shown in Figure 2.4. Four factors determine the stability criterion of a perovskite crystal namely; the Charge balance in the crystal, number of atom balance (stoichiometry), Oxygen balance, and Ionic radii balance (tolerance factors).

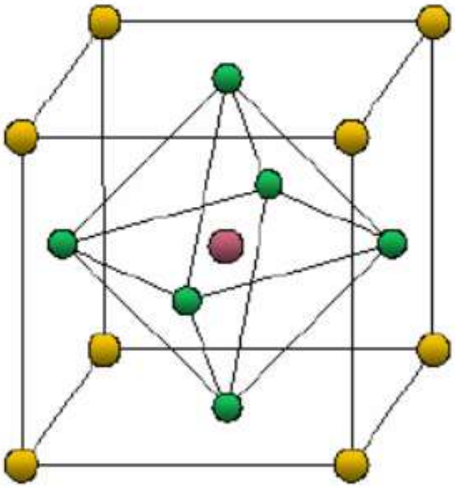

Figure 2.3: Single crystal structure of a perovskite crystal. The yellow, red, and green elements represent the sites A, B, and O respectively.

In considering the charge balance in the perovskite structure, charge balance is from the interaction between the positively charged ions and the negatively charged oxygen ions in the crystal. The ions occupying the positions of A and B (Figure 2.4) possess a charge of 2+ and 4+ respectively such that these can balance the charge of 6- provided by the three oxygen atoms. When the balance is established the ABO_3 structure becomes neutral.

For the number of atoms in a perovskite structure to be considered balanced, the ratio of 1:1:3 or its multiple must be maintained. However, for some layered perovskite structures, the concentration of some atoms may be reduced to achieve stability. For a single perovskite crystal, the allowed number of atoms is five.

To avoid the existence of defects in the crystal, there must be a balance in the oxygen concentration. A very slight change in the concentration of oxygen leads to a charge imbalance in the crystal affecting either site A or B. an equal balance of oxygen usually prevents such defects.

The tolerance factor is the measure of the balance in the ionic radii of A, B, and O atoms in the crystal. It is possible to substitute atoms at sites A and B provided the ionic radii of the substituted atoms correspond with the radii of atoms in the sites. For example in the $GdBa_2Cu_3O_{7-x}$, the Gd atom replaces one of the Ba atoms in the structure, and for the balance to occur the Gd must have a radius corresponding to Ba. The tolerance factor for the ABO_3 structure is given by;

$$\tau = \frac{R_A + R_0}{\sqrt{2}(R_B + R_0)} \tag{2.64}$$

The allowed values for a stable perovskite structure are $0.8 \leq \tau \geq 1.1$ (Navrotsky, 1998; Priya *et al*., 2003; Vickery & Klann, 1957; Vittayakorn *et al.*, 2003).

2.22 Double Perovskite Structures

The double perovskite structures are formed when two different atoms say. B_1 and B_2 occupy the B site of the crystal structure. An example of a double perovskite structure is shown in Figure 2.4 below;

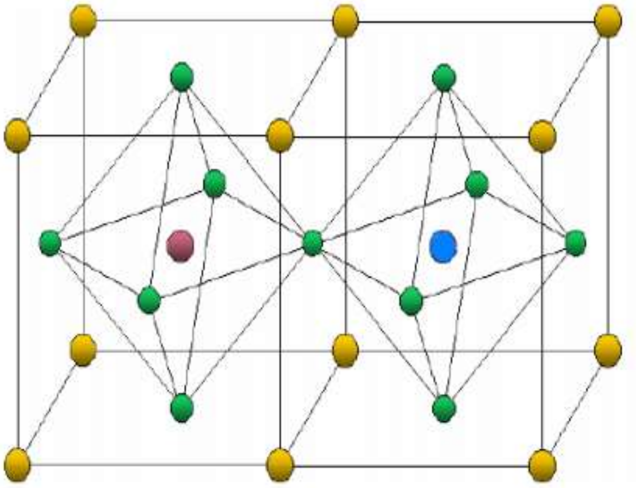

Figure 2.4: $A_2B_1B_2O_6$ double perovskite material.

In the Figure 2.4, the red and the blue elements present the B_1 and B_2 respectively. The yellow and the green elements occupy sites A and O respectively. In the double perovskite structures, the contribution of the atoms B1 and B2 are the same hence the preferred ratio is 1:1 and the balance of the formula is equal between the two. The average charge for site B resulting from the two should also be 4+ meaning the atomic ions for B1 and B2 should have the charge of 2+ and 6+ or 5+ and 3+ or 4+ and 4+ such that the average becomes 4+. The tolerance factor of the double perovskite structures is given by equation 2.65.

$$\tau = \frac{(R_A + R_O)}{\sqrt{2}\left(\left(\frac{R_{B_1} + R_{B_2}}{2}\right) + R_O\right)} \qquad (2.65)$$

In some cases, the ratio of B_1 to B_2 may be unequal meaning the contribution of B_1 to atomic balance is not the same as the contribution of B_2. The preferred ratio for this case is 1:2 such that the formula can take the form $AB_1\frac{1}{3}B_2\frac{2}{3}O3$.

2.23 Applications of Perovskites

The perovskite structure comprises rich metallic phases which can be expressed by ABO_3 in which the A site is occupied by the main metallic elements in the periodic table while comprising mainly of the transition metals. Also, the perovskites can be considered in terms of the variation of the anions and cations which measure the degree of stability. The ability of these structures to vary the number of ions affects the physical properties of the structures which can determine their various areas of application. Examples of the perovskites that readily form the anion and cation vacancies include $NaxWO_3$, $Sr_2SrTaO_{5.5}$, high Tc cuprates superconductors, Aurivilius phases, and brownmillerite structures. These perovskites portray good magnetic, dielectric, electronic, elastic, and catalytic properties for various technological and industrial applications.

The $BaTiO_3$ perovskite has been reported to have very high dielectric properties (Galasso, 1969; Shirane *et al.*, 1957). This property finds application in the manufacturer of capacitive components. Oxide perovskites that are not cuprate in nature such as $Ba(Bi_{1}\text{-}Pbx)O_3$ and $(La_{1-x}Ca_x)MnO_3$ portray superconducting and magnetostrictive properties (Fontcuberta *et al.*, 1996; Hwang *et al.*, 1995).

Chemical substitution of one or more atoms in the oxygen site in the structure of the perovskite material can also improve the properties for technological and other applications. One such application includes the development of dielectric resonators and filters which can be used in microwave signal devices such as mobile phones and other wireless devices (Dutta & Sinha, 2011). A high dielectric constant coupled with the permittivity of these perovskites can also be used to make the electro-optic modulators. The electro-optic form special components in the transient field electroluminescence TFEL panels which form part of the computer display panel.

The electrostrictive actuators which are the components that modify electrical signals based on the magnitude of the frequency have a perovskite structure. Upon application of an external field in these materials, the atomic positions can undergo a slight shift which can lead to permanent polarization of the material. Electrostrictive actuators are used in projectors for submarines and surface vessels which enhances communication.

Perovskite with giant magnetoresistance (GMR) is characterized by high sensitivity in the presence of the magnetic field. This class of materials is applied in magnetic data storage and retrieval (Vickery & Klann, 1957).

If site B of a double perovskite material is substituted by two different transition metals the structure of the perovskite changes leading to changes in different properties of the newly formed material. Some of the new properties that can be formed include; stable structure, ferromagnetic, magnetoresistance, and magneto capacitive properties (Kumar *et al.*, 2019; Mitra *et al*., 2018). Examples of the materials that belong to this class of materials are the high-temperature cuprate superconductor (HTS). This class of materials can be used in the fabrication of HTS thin film devices, thermoelectricity, solar applications, energy conversion systems, and photocatalysis.

2.24 Structure and Classification of Superconductors

Materials with a general structure of the form ABO_3 are considered to have a perovskite structure. The site occupied by elements usually comprises of the rare earth metals to the alkaline earth metal and the site is usually at the corner of a crystal lattice. Site B is usually occupied by the ions from 3d to 5d transition metal elements. At a stable state, the orthorhombic and the tetragonal crystal lattice are the ones that form the majority of members of this group. Some perovskites undergo distortions while others do not. The degree of distortions is determined by the elements that occupy site A. For example In $GdBa_2Cu_3O_{7-}$ which is a layered perovskite the Cu-O-Cu change of bond angle happens and as a result, the crystal undergoes lattice distortion.

2.24.1 Classification of Perovskite

Based on the unique properties that are displayed by the perovskite both in the theoretical and application spectrum they can be categorized as Superconducting perovskites, colossal magnetoresistance perovskites, Piezoelectric & ferroelectric perovskites, and other categories.

2.24.2 Superconducting Perovskites

There are many superconducting superconductors but a well-studied group is the cuprate superconductors because of the potential practical application based on the high superconducting transition temperature they are capable of achieving. These cuprates are characterized by distortions, and deficiency of oxygen and are usually made of layers that alternate between the Cu-O_2 planes where superconductivity takes place in the layers. This is made possible because of the changes in the spin from the antiferromagnetic spin when they are doped. Some of the possible areas of application of these perovskites include; electrical transmission, reducing the power loss in transformers, and Superconducting digital circuits.

2.24.3 Colossal Magneto Resistance Perovskites

These are perovskites that depend on the magnitude of temperature and magnetic field in their efficiency. An example of this class of perovskites is the $LaMnO_3$ which is an antiferromagnetic (AFM) insulator in which the ferromagnetic (FM) coupling lies in the MnO_2 planes and the antiferromagnetic (AFM) coupling between the planes. When the material is doped with Ca in the range of $0.2 < \times < 0.5$ the material undergoes paramagnetic to ferromagnetic transition upon cooling or metal to insulator (MI) transition. When the concentration of Ca is kept high, at the ground state the material remains antiferromagnetic and thus a nonmetal(Progress, 2016).

The interest of these superconductors lies in their potential applications in electronic, magnetic, and structural properties. Some of the applications of these superconductors include; Hybrid cells, Sensors, and Magnetic data storage.

2.24.4 Piezoelectric and Ferroelectric Perovskites

These perovskites can either have a center of geometry or lack to have a center of geometry. Some of those which lack the center of geometry exhibit polarization on the application of mechanical stress and this is attributed to the electrical dipole moment that exists in their crystal lattice. If the electric dipole moment is reversed by the application of an electric field then the material is ferromagnetic and is referred to as ferroelectric (FE) and if the temperature is used to reverse the electric dipole moment then the material is said to be pyroelectric (PE). Some of the applications in this category include microphone sensors, piezoelectric motors, and Vibration dampers. The Figure below shows the variation of magnetization with temperature for $La_{1-x}CaMnO_3$.

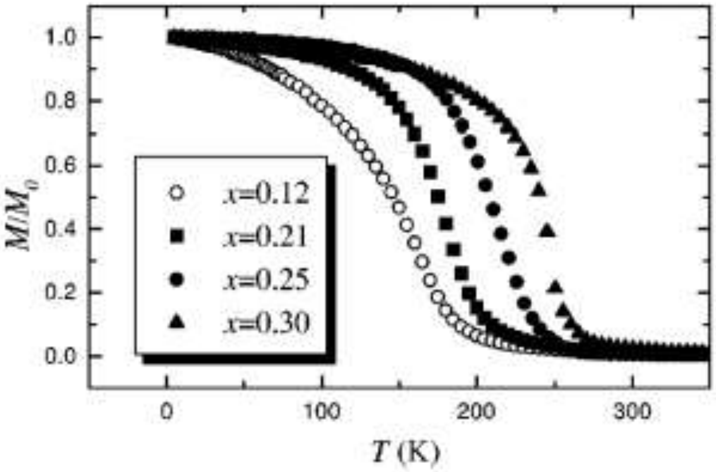

Figure 2.5: Normalization of magnetism (M) as a function of temperature (T).

The curve eventually normalizes with the variations of concentration as indicated in the legend presented in Figure 2.5.

2.25 Gadolinium Barium Copper Oxide ($GdBa_2Cu_3O_{7-x}$)

$GdBa_2Cu_3O_{7-x}$ has a perovskite structure. The structure is cubic and may possess some distortion. The orthorhombic and tetragonal phases are the most common variants. The structure of the material is presented in Figure 2.6.

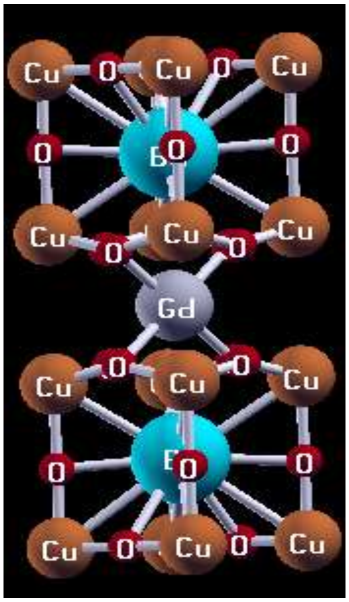

Figure 2.6: The structure of gadolinium barium copper oxide perovskite structure.

$GdBa_2Cu_3O_{7-x}$ is of interest as an example of a magnetic ion-containing superconductor (Xie, 2014). Compared to other rare earth metals 123 perovskites, it exhibits maximum known Neel temperature, T_N=2.2K. Experimental data show that it has T_c=90K. In 2011 the perovskite sample was applied in making more flexible cables than ever before (Литовцы, 2018). It is believed that GBCO exhibits high irreversible magnetic fields and high critical current density under a high magnetic field as compared with YBCO, and hence more promising for application (J. P. Zhou *et al.*, 2002). The superconducting properties change reversibly with strain even before mechanical damage occurs. Reversible change is caused by the pressure dependence of T_c of the superconductor.

Taking the analogy of $YBa_2Cu_3O_{7-x}$, the structure of $GdBa_2Cu_3O_{7-x}$ is considered a defect perovskite lattice based on the fact that it has three copper (Cu) cubes at the center with oxygen (O) vacancies ordering and Gadolinium-barium (Gd-Ba) along the c axis of the crystal (Beno *et al.*, 1987). The expected perovskite formula for the crystal is $(GdBa)_3Cu_3O_{9-x}$ to match the expected perovskite order. Of the two vacancies (x=2) one occurs in the third CuO plane, along the a axis for example at the site (0.5, 0, 0). This gives the crystal orthorhombic symmetry. The gadolinium (Gd) and the two barium (Ba) ions are ordered along the c axis and the other oxygen vacancy occurs along the Gd plane. The CuO_2 planes and the CuO chain give the characteristic property of the crystal structure. The chain consists of O1 and Cu1 atoms located at the $(0,\frac{1}{2},0)$ and (0,0,0) respectively. The O4 atom is located between the Cu1 atom at the coordinates (0,0,zO4) along the z axis. In comparison with other copper-Oxygen bond lengths, it is found that Cu1-O4 has the shortest distance of separation. Cu1 is fourfold coordinated with the oxygen (O) ions and every O1 ion is shared among two Cu1 atoms. Cu2 which is located at (0,0,zCu2) along the c axis of the crystal and has O2 and O3 lying side by side at the sites $(\frac{1}{2},0,zO2)$ and $(0,\frac{1}{2},xO3)$ respectively. Taking the measurements in the units of c, then for $YBa_2Cu_3O_{7-x}$ we have zCu2=0.3574, zO2=0.3767, zO3=0.3804, and zO4=0.1542 (Beno et al., 1987). By varying the concentration of oxygen in such a way that the value of x in the $GdBa_2Cu_{7-x}$ takes a value of $x > 0.5$ the structure undergoes polymorphic transformation to a tetragonal phase. The ideal symmetry for this phase occurs when $x = 1$ and the formula becomes $GdBa2CuO_6$ which happens by the removal of O1 from the CuO chain. The same effect of polymorphic transition can occur when the orthorhombic phase of the structure is subjected to high temperatures.

2.26 The Electronic Structure of the Cuprate Perovskites

In cuprate superconductors, it is the ionic forces and size that determine the structure and the stability if their crystal structure. For this reason, most of the known perovskites are ionic insulators. In this group of materials, the formal valence is closely related to the actual charge. The total charge over a given unit cell must vanish due to its integral nature. The assignment of the formal valence for the high temperature superconductor such as $GdBa_2Cu_3O_{7-x}$ derived from the fact that Alkaline earth metals are dispositive; rare-earth metals and lanthanides are tripositive and oxygen is doubly negative.

2.27 Superconductivity and Hole Concentration in the $GaBa_2Cu_2O_{7-x}$

Previous studies have indicated that the substitution of the O^{2+} ions in the cuprate perovskites can cause an increase in the hole concentration in the Cu-O layer that influences superconductivity in the perovskite (Antipov *et al*., 2002; Manuscript, 1972). The introduction of more holes in the copper layer can be based on the position of Cu^{2+} cation in the structure. The increase of the hole concentration to $x = 0.5$ explains the ability of the Cu-doping in concentrating mobile holes which play a major role in inducing superconductivity on the non-superconducting $GaBa_2Cu_2O7_{-x}$ with $x = 0$. The effect of increasing the hole concentration results in to increase in the superconducting transition temperature when the resistance is zero ($T_C^{R=0}$). By varying the concentration of the oxygen ions in the structure, changes in the physical and electronic properties are noted. The changes can be attributed to the change in the charge balance in the Cu-O layer and the CuO_2 plane. During the flow of electrons in the process of conductivity, the layer serves as a reservoir of the charges from which the copper planes receive the outflow. The decrease in oxygen concentration results in a decrease in the T_c. The effect of the hole concentration leads to the changes in the structure of the material and the phenomenon of superconductivity disappears as the value of x goes beyond 0.5. It is therefore important to note the shift of the electronic structure to the metallic phase can be explained in terms of the structural changes that affect the shift of the Fermi level and so the density of states at the Fermi level.

2.28 The Diffusion of the Hoping Oxygen in $GdBa_2Cu_3O_{7-x}$

The hopping oxygen in cuprate superconductors is one of the factors that influence the properties of the superconductors and thus plays a big role in determining the potential application of the superconductor in different fields. The basic mechanism of diffusion of oxygen is largely linked to point defects. The diffusing oxygen obeys the equation of diffusion given by;

$$\frac{\partial}{\partial x}\left(D\frac{\partial C}{\partial x}\right) = \frac{\partial C}{\partial t} \qquad (2.66)$$

The equation represents a one dimensional diffusion in which the concentration of the diffusing element, x is the space coordinates, t is the time taken for the diffusion to take place and D is the diffusion coefficient. There are two types of diffusion gradient; the tracer diffusion gradient and the chemical diffusion gradient. Of interest is the chemical diffusion gradient which gives a description of the diffusion under a chemical potential. The chemical diffusion can be looked at in terms of the sample being equilibrated to less than two oxygen partial pressure (P_{O2}) and the sample being equilibrated to a new (P_{O2}) under the influence of the diffusing oxygen defined by a different diffusion coefficient ($\overline{D}$) which gives a measure of oxygenation. The value of $(\overline{D})$ is calculated from the time dependent properties such as the electrical resistivity of the sample as oxygen equilibrates with the new partial pressure (P_{O2}), calculation of relaxation time t and the diffusion coefficient from t, and the use of the linear space dimension x under which the diffusion takes place using the relation;

$$D = \frac{x^2}{6t} \tag{2.67}$$

D is a second rank tensor and takes three values for an orthorhombic crystal structure (Dissertations, 2015), one parallel to the principle crystallographic axis. This helps to explain the differences in the diffusion coefficient in different directions especially, in the anisotropic crystal structures such as the cuprate superconductors.

2.29 Transport Properties of the Cuprate Perovskites

The transport properties of the cuprate perovskite superconductors are based on the existence of the cooper pairs which is basically the attraction between the nearest neighbor electrons. This can be explained in terms of the way the other toms respond to the first electron. This happens when the atoms get attracted to the first electron in pairs and as a result of that, they start to fall off around the position of that electron. On the arrival of the second electron, the atoms get disturbed and in the process, they provide it with a strong attractive force. In this model, the first electron is said to turn over with a sudden quick movement of the spin of one atom in the crystal lattice and in the process the atom interacts with the second electron. In the $GdBa_2Cu_3O_{7-x}$ the electrons which are the charge carriers are conducted along the CuO planes. The directional resistivity is much more in the direction normal to the plane and that parallel to the plane is lower.

2.30 Point Defects

Atomic transport is enhanced through the motion of point defects and therefore is related to the thermodynamics of the defects through the concentration and the defect equilibrium (Bolse, 1994; Freysoldt *et al.*, 2014). The stoichiometry of all the superconducting oxides deviates from the normal because of the point defects in those superconductors (Cava RJ, 1990; Gazquez *et al*., 2016). Majorly the defects are more on the oxygen but can also occur in the other cations and electronics defects electrons and holes. The cation and the electronic defects coupled with the electronic mobility term lead to the normal electrical properties of the structure which may include; conductivity, thermoelectric power, and the Hall Effect (Chung *et al*., 2012; Witting *et al*., 2019). These defects also affect the critical transition temperature and the conductor to superconductor transition. By incorporation of the interstitial oxygen, the equilibrium can be expressed by the equation;

$$\frac{1}{2}O_2 \Leftrightarrow O_i + 2\dot{h} \tag{2.68}$$

Or by filling the oxygen vacancy;

$$\ddot{V}_O + \frac{1}{2}O_2 \Leftrightarrow O_o + 2\dot{h} \tag{2.69}$$

In which the Kröger–Vink notation has been used in the description (Kröger & Nachtrieb, 1964).

2.31 Diffusion in $GdBa_2Cu_3O_{7-x}$: Structure and Point Defects

The structure of the $GdBa_2Cu_3O_{7-x}$ plays a vital role in enhancing oxygen diffusion which brings about the phenomenon of superconductivity (Mccoy, 2020; Pereiro *et al.*, 2011). The Cu and O in the orthorhombic crystal of $GdBa_2Cu_3O_{7-x}$ are arranged in CuO_2 planes such that we have O(2), O(3) and Cu(2) and the CuO chains (Cu(1) and O(1), with additional oxygen around the Ba2+ ions O(4). When the value of x in the structure is zero, the O(1) is fully occupied while the O(5) site is empty (Liuermore et al., 1990). As the value of x increases as a result of either increasing partial oxygen pressureP_{O_2}, some O(1) sites become vacant. At high pressure, some O(5) sites are filled and a few of the O(4) sites become vacant. During the phase change from the orthorhombic to tetragonal an equal amount of the O(1) and O(5) are filled. The orthorhombic phase which is the most stable phase has a majority of oxygen vacancies $\ddot{V}_O$ in the O(1.).

The oxygen vacancies come not by means of doping the structure by cation but by changing the condition of either partial pressure or temperature on oxygen and a corresponding charge of the $\ddot{V}_O$ is compensated by the resulting hole concentration changes (Fay, 1967). Random distribution of the $\ddot{V}_O$ occurs when x is nearing zero (Engineering et al., 1991). When the magnitude of x becomes finite, $\ddot{V}_O$ tends to align in a string like format since the Cu ions are on the opposite side of $\ddot{V}_O$ and tend to form unfavorable configuration (Mehta et al., 1992). The full and empty strings also reorder at $x = 0.5$ in which case the O(1) alternates between full and empty rows.

2.32 The Future Prospects of Perovskites Materials

The expected future dimension on the perovskites is anchored on coming up with uncombined perovskites through methods such as the optimized interface of materials. This is geared towards increasing both the performance and stability and other properties which are likely to shift the organic compounds to inorganic compounds. The driving factor in the manufacture and modification of perovskites is majorly based on increasing efficiencies. With it invention of the 2D perovskites and the improved interface materials, there have been reduced drawbacks and increased efficiency.

In relation to perovskites solar cells, the effect of the external environmental conditions they have on the lead halide perovskite greatly affects the performance of the solar cell as it reduces the stability of the cell. As a resul,t there is a need to have devices with strong stability, light absorbing substrate, and electron and hole substrate which are very crucial in terms of the practical implementation of the device. Secondly, the hole carrying device for the device is very costly and affects the synthesis process for the cells. Thirdly, it is difficult to deposit thin films of the perovskites in the solar cell using the traditional method and hence some other methods should be devised to allow high quality perovskites for solar cells, especially for commercial use. Fourthly, the radioactive nature of the lead element that is used in perovskite solar cells is extremely harmful and may affect the production of such cells. Lastly, there is insufficient information on the micro-mechanic system to clearly describe the perovskite solar cells. Therefore, there is a great need to come up with theoretical models to give a full description and at the same time define how the efficiency of such a cell can be achieved. Also, research should be increased to not only increase the performance of the peroveskte solar cells but also come up with new materials that are simpler and more effective.

CHAPTER THREE

METHODOLOGY

3.1 Theoretical Methods

3.1.1 Many Body Schrödinger Equation

Properties of quantum materials whose properties cannot be described by semi classical means can only be addressed by a quantum mechanical system (Woolley & Sutcliffe, 1977). For these groups of materials, electronic structure is analyzed by solving the Schrödinger equation. In quantum mechanics, it is the wave function that holds all the information about a system. Once the wave properties have been obtained other associated properties can be predicted. Some of these properties include; the polymorphic phase transition, elastic properties, magnetic properties, nuclear vibrational modes, and charge density. This is obtained by solving the time-independent Schrödinger equation.

$$H\psi(r,R) = E(R)\psi(r,R)$$

Where,

$$H = -\sum_j^N \frac{\hbar^2}{2M_j}\nabla_j^2 - \sum_i^n \frac{\hbar^2}{2m_i}\nabla_i^2 + \sum_j^N \sum_{p>j}^N \frac{Z_j Z_p}{|R_j - R_P|} - \sum_{i=1}^n \sum_{j=1}^N \frac{Z_j e}{(r_i - R_j)} + \sum_{i=1}^n \sum_{q>1}^n \frac{e^2}{|r_i - r_q|} \tag{3.1}$$

The equation can be solved to get the desired properties of a system. The problem with the equation is that the potential experienced by each electron is influenced by all other electrons and the nuclei within a given system. Solving the time-independent Schrödinger equation directly for all electrons cannot be achieved accurately and thus approximations have to be made. The approximations are based on a mean-field approximation that factorizes the many-body equation into a set of the single-electron equation, in which an electron moves in an even field generated by all the other electrons. These approximations are discussed below:

3.1.2 The Born-Oppenheimer Approximation

The approximation treats electrons to be far light in mass as compared to the ions. This means that the kinetic energy of the electrons is much higher compared to those of the ion. The response of the electrons to the ions represents the true ground state which then can be used to calculate the ground state energy of the system. The position of the ions is assumed not to vary because if they do so, it will lead to a multidimensional ground-state potential energy surface. In this case, the motion can better be described by classical mechanics because of the particle-like behavior of the classical particle in the electrostatic potential. The approximation further explains that potential energy due to nuclei and nuclei repulsion has a constant value which then changes the Hamiltonian to become an electronic Hamiltonian equation 3.2.

$$\widehat{H}_e = -\frac{1}{2}\sum_{i=1}^{N} \nabla_i^2 - \sum_{i=1}^{N}\sum_{A}^{M}\frac{ZA}{r_i\,A} + \sum_{i=1}^{N}\sum_{r_{ij}}^{N} 1 = \hat{T} + \hat{V}_{Ne} + \hat{V}_{ee} \tag{3.2}$$

The wave function ψ_e becomes the solution for equation 3.2 where $\widehat{H}_e$ is the total Hamiltonian for the system. Since the nuclear coordinates are not presented in the ψ_e the wave function, the total energy then becomes the total sum of the electron energy and that which results from the electrostatic repulsion between the nuclei.

$$E_N = \sum_{B>A}^{M}\sum_{A}^{M}\frac{Z_A Z_B}{R_{AB}} \tag{3.3}$$

Therefore,

$$E_{Total} = E_e + E_N \tag{3.4}$$

The operator $\hat{V}_{Ne}$ in the equation 3.2 is the external electron-nuclear electrostatic attraction potential. This external potential can be influenced by external magnetic or electric fields.

3.1.3 Density Functional Theory

The density functional theory (DFT) is anchored on the principle that for a system of many interacting particles, their properties are basically the functional of their ground state density

(ρ). The ground state density determines all the information about all the wave functions for the ground state and even the exited states. The main objective of the density functional theory is to calculate the ground state energy of a many-body system. This is achieved by solving the time-independent Schrödinger equation based on the Born-Oppenheimer approximation such that;

$$H\Psi(r_1, r_2 \ldots \ldots r_n) = E\Psi(r_1, r_2 \ldots \ldots r_n) \tag{3.5}$$

In the equation, the Hamiltonian is a sum of the kinetic energy, interaction with the external potential (V_{ext}), and the electron-electron interaction (V_{ee}) and thus;

$$H = -\frac{1}{2}\sum_i^N \nabla_i^2 + \hat{V}_{ext} + \sum_{i<j}^N \frac{1}{|r_i - r_j|} \tag{3.6}$$

In computational DFT, the external potential of interest is the interaction between the electrons and the nuclei and is expressed as;

$$\hat{V}_{ext=-\sum_{\alpha}^{Nat}\frac{Z_{\alpha}}{|r_i-R\alpha|}} \tag{3.7}$$

3.1.4 The Independent Electron Approximation

The independent electron approximation can be considered in two ways; the non-interacting and the Hartree-Fock. The two approaches apply the same concept in explaining the behavior of electrons in a system by assuming that the electrons are not related and do not interact and therefore considered to obey the Pauli's Exclusion principle. The only difference is that in the Hartree Fork approximation, the coulomb potential resulting from the interaction between electrons is considered while the energy of correlation that results from those interactions is ignored. Generally even when considering the non-interacting situation, the theories try to bring in some aspect of real interaction that incorporates the real interaction in the effective Hamiltonian. According to Hartree, there exists a different potential for each electron because He was subtracting a certain term from the electron based on the orbital. Later an improvement was done on the same to come up with an effective potential in what we call the Hartree-Fork method.

3.1.5 The Non-Interacting (Hartee-Like) Electron Approximation

3.2 The calculations that are involved in the treatment of the non-interacting electrons involve the solution of the Schrӧdinger equation;

$\widehat{H}_{eff}\,\Psi_i^\sigma(r)=E_i^\sigma\Psi_i^\sigma(r)$ (3.8) Where $\widehat{\mathrm{H}}_{\mathrm{eff}}$ is the effective Hamiltonian whose effective potential acts on the two spin in an electron presented by σ at a distance r. Just like any quantum mechanical system, the ground state for the non-interacting electrons is usually taken to be that with a minimum energy value of the Schrӧdinger equation and at the same time obey the Pauli's exclusion principle. In the event the Hamiltonian does not depend on the spin up or the spin down, then the system is considered to be degenerate, and in computation, the spins are considered as a factor of two.

3.2.1 Hartree Fork Theory

The theory provides a better scheme for solving the many electrons wave function. This is because Electron-electron potential energy in it is the main complication in electronic structure calculation. The method is built on the fundamentals of molecular orbital theory, in which every single electron motion can be described by a single wave function that is independent of the motion of other electrons. It is built after applying the Born Oppenheimer approximation as discussed above. We start by writing the wave function in the form of the Hartree product as by equation 3.9.

$$\psi_{HP}(r_1, r_2, \dots \dots \dots \dots .., r_N) = \emptyset_1(r_1)\emptyset_2(r_2) \dots \dots \dots . \emptyset_N(r_N) \qquad (3.9)$$

The equation fails to obey the antisymmetric principle (half integral spin) which states that any wave function describing fermions should be antisymmetric to the interchange of the intrinsic space-spin coordinates within the system. Letting α and β be the spin coordinates ω the space-spin coordinate can be expressed as; $x = \{r, \omega\}$. Also, the spatial orbitals $\emptyset(r)$ are transformed to $\chi(x)$ spin-orbital. The spin functional possess a very important feature; they should be orthonormal and hence makes the computational process become possible. The overall energy is the sum of one-electron energies and the overall wave function will be expressed as a product of the one-electron wave function. Thus, the Hartree product can be written as:

$$\psi_{HP}(x_1, x_2, \dots \dots \dots \dots .., x_N) = \chi_1(r_1)\chi_2(r_2) \dots \dots \dots . \chi_N(x_N) \qquad (3.10)$$

For the equation to satisfy the antisymmetric principle, we introduce the concept of the Slatter which ensures that the wave function does not vanish if any more than two spin orbitals become equal. The Slatter determinant is expressed as by the equation;

$$\psi = \begin{bmatrix} \chi_1(x_1) & \cdots & \chi_N(x_1) \\ \vdots & \ddots & \vdots \\ \chi_1(x_N) & \cdots & \chi_1(x_N) \end{bmatrix} \qquad (3.11)$$

The equation is an approximation against Fermi Dirac statistics and the Pauli Exclusion Principle. To solve the problem, an n-electron wave function is written not as a simple product of one electron spin-orbital, but as a Slater determinant built on the n spin orbitals. The Slater determinant ensures that the Pauli principle is obeyed which is anti-symmetrical under the interchange of any pair of electrons.

The variation principle is applied in the formation of the Slater determinant to ensure the wave function yields minimum energy. This is achieved by varying the spin-orbital under conditions that they will remain orthonormal such that the resulting energy will always be minimal.

The combination of factorization of the wave function into one-electron orbital to the mean-field approximation gives rise to the Hartree Fork method.

Hartree Fork equation is solved iteratively via the self-consistent field (SCF) method. In this method, a trial set of spin-orbital is formulated to construct the fork operator which is then used in the Hartree Fork equations to produce a new set of spin orbitals. The spin orbitals are put back through a method and the cycle continues until some numeral convergence criteria are satisfied. The Slater determinant built from the occupied spin orbital is the Hartree fork ground state.

The limitation of the Hartree fork is that; it does not take into account the correlation existing between the movements of the electrons due to the independent particle model upon which it is based. The correlation is defined as the difference between the external energy of the system and the calculated by Hartree Fork approximation at the Hartree limits (with an infinite basis set).

The theory is based on analyzing ground state properties by the use of electron density ρ. By integrating the density of overall space, we find the total number of electrons, N:

$$N = \int \rho(r) dv \tag{3.12}$$

Density is given by the square of the wave function. The method considers a system of non-interaction electrons with uniform density, acted on by a potential V(r). the total energy is formed of the kinetic energy and the potential energy parts such that;

$$E_{Tot} = E_{kin} + E_{pot} \tag{3.13}$$

$$E_{Tot} = \frac{\hbar^2 \alpha}{m} \int \rho(r)^{\frac{5}{3}} dr + \int V(r)\rho(r) dr \tag{3.14}$$

where $\alpha = \frac{3}{10}(3\pi^2)^{2/3}$

Also includes electron-electron interaction which comes in two ways.

Coulomb interaction:

$$E_{coul} = \frac{e^2}{8\pi\varepsilon_o} \iint \frac{\rho(r)\rho(r')}{|r-r'|} \tag{3.15}$$

Exchange energy per unit volume of position:

$$E_{ex} = \frac{e^2\beta}{8\pi\varepsilon_o} \rho(r)^{\frac{4}{3}} \tag{3.16}$$

If integrated over the whole space the exchange energy is;

$$E_{ex} = \frac{e^2\beta}{8\pi\varepsilon_o} \int \rho(r)^{\frac{4}{3}} dv \tag{3.17}$$

The correlation is the difference between exact electron-electron interaction and the contributions from Coulomb and exchange.

3.2.2 Thomas and Fermi Model

This is purely a quantum statistical model of electrons in a system in which the kinetic energy of the electrons is considered while the electron-electron interactions and the nuclear-electron interactions are considered to be classical. The kinetic energy functional is given by the equation;

$$T_{TF}[\rho\overrightarrow{r}] = \frac{3}{10}(3\pi^2)^{\frac{2}{3}} \int \rho^{\frac{5}{3}}(\vec{r})d\vec{r} \tag{3.18}$$

The kinetic energy is then combined with the classical equation in which the nuclear-electron attractive Coulomb potential and the electron-electron repulsive Coulomb potential give the total Fermi energy for the system and given by the equation;

$$E_{TF}[\rho(\vec{r})] = T_{TF}[\rho\overrightarrow{r}] = \frac{3}{10}(3\pi^2)^{\frac{2}{3}} \int \rho^{\frac{5}{3}}(\vec{r})d\vec{r} - Z\int \frac{\rho\vec{r}}{r}d\vec{r} + \frac{1}{2}\iint \frac{(\rho\vec{r}_1,\rho\vec{r}_2)}{r_{12}}\mathrm{d}\vec{r}_1 dr_2 \tag{3.19}$$

The equation is the true definition of the density functional theory. It tells how the density of a system can be used to compute the ground state energy without any additional information including the wave function and basis sets.

3.2.3 Hohenberg-Kohn Theorem

Energy can be described exclusively using electron density. Considering several electrons and nuclei, enclosed in a large box and moving under the influence of external potential V(r) and mutual interaction. The Hamiltonian of such a system can be described by the equation;

$$\widetilde{H} = \widetilde{T} + \widetilde{U} + \widetilde{V} \tag{3.20}$$

The first Hohenberg-Kohn theorem states that the external potential is univocally determined by the electronic density, besides an additive constant. A uniform shift in V(r) by an arbitrary constant has no physical effect. Also, two different potentials can't give the same ground-state density meaning that all properties of a system can be calculated from the electronic density.

The second theorem shows that the density obeys a variation principle; that is, given an external potential V(r), the electronic density of the system is the one that minimizes the energy. Since the ground state expectation value of $\hat{H}$ is a functional of the density, ρ(r) also the single contribution to $\hat{H}$ can be expressed as functional of ρ(r). We, therefore, have: functional is given by the equation;

$$E_{(g)}[\rho(r)] = \int V(r)\rho(r)dr + F[\rho(r)] \qquad (3.21)$$

$\hat{F} = \hat{T} + \hat{U}$ Represents kinetic energy and electron-electron interaction. Because of the long-range Coulomb interaction, it is convenient to separate from Fρ(r), the classical Coulomb energy between electron and have thus we have;

$$F(\rho_r) = T[\rho(r)] + U[\rho(r)] \qquad (3.22)$$

The energy can be expressed explicitly by electron-electron interaction in $U[\rho(r)]$ and the energy for the system of interacting electrons is given by:

3.2.4 Kohn-Sham Method

As observed from the Schrödinger equation, energy functions have uniquely three parts; the kinetic energy of the electrons, the interaction with the external potential, and the electron-interaction. This can be expressed as;

$$E[\rho] = T[\rho] + V_{ext} + V_{ee} \qquad (3.23)$$

The Khon-Sham method defines a practical way to solve the Density functional theory equation by approximating the kinetic energy and the electron-electron interaction functional to ensure proper minimization of energy. The method introduces a system defined by N electrons that are free of interaction and described by a single determinant wave function of $\emptyset_i$ orbitals as explained in the Hartree-Fock method. The kinetic energy of the system and the electron density are known exactly from the knowledge of the orbitals. Thus, the Kinetic energy is given as;

$$T_s = -\frac{1}{2}\sum_i^N \langle \emptyset_i | \nabla^2 | \emptyset_i \rangle \qquad (3.24)$$

Where the electron density is given by;

$$\rho(r) = \sum_i^N \left| \emptyset_i^2 \right|^2 \qquad (3.25)$$

Considering the electron-electron interaction from the classical perspective, the Hartree coulomb potential is given by;

$$V_H = \frac{1}{2}\iint \frac{\rho(r_1)\rho(r_2)}{|r_1 - r_2|} dr_1 dr_2 \qquad (3.26)$$

The energy functional can then be written as:

$$E[\rho] = T_s[\rho] + V_{ext}[\rho] + V_H[\rho] + E_{xc}[\rho] \qquad (3.27)$$

Where E_{xc} is the exchange-correlation functional term that is supposed to take care of the inaccuracies made by using the non-interacting kinetic energy and by giving the electron-electron interaction a classical treatment. The energy functional equation 3.27 can be written in terms of the density of non-interacting electrons and by application of the vibrational principle, the orbitals that lead to the minimization of the energy can be expressed as;

$$\left[-\frac{\hbar^2}{2}\nabla^2 + V_{ext}(r) + \int \frac{\rho(\acute{r})}{|r-\acute{r}|} + V_{xc}(r)\right]\emptyset(r) = E_i\emptyset_i \qquad (3.28)$$

The V_{xc} is given as:

$$V_{xc} = \frac{\delta E_{xc}[\rho]}{\delta\rho} \qquad (3.29)$$

If the vibrational principle is applied in equation (3.28) under the constraint that the total number of electrons remains constant, we get the equation;

$$\frac{\delta E[\rho]}{\delta\rho(r)} = \frac{\delta T}{\delta\rho(r)} + V_{ext}(r) + \int \frac{\rho(\acute{r})}{|r-\acute{r}|} + \frac{\delta E_{XC}}{\delta\rho(r)} = \mu \qquad (3.30)$$

The necessary condition for the Lagrange multiplier μ is that the number of particles must be conserved. The above equations indicate the possibility of creating a system of the interacting electron as a non-interacting system.

The theory on which density functional theory is based is formally exact, however, relies on the knowledge of the exchange and correlation functional whose exact definition is unknown. The most important step is therefore to decide on a suitable approximation for exchange energy. The main aim of DFT is to define a more accurate approximation for the exchange energy.

3.2.4 The Kohn-Sham Equation

The Kohn Sham equation is generated by the introduction of three terms in the energy functional:

i. The kinetic energy of the non-interacting N-electron system term $T_s(n)$ thus kinetic energy becomes:

$$T[n] = T_s[n] + T_c[n] \tag{3.31}$$

$T_c[n] \ll T[n]$ hence $T_s[n]$ contributes the majority of the kinetic energy.

ii. The atomic coulomb $V[n]$ can be presented as the sum of the Hartree term $E_H[n]$ and another contribution $\Delta U[n]$ which results from the quantum nature of the interacting electrons:

$$U[n] = E_H[n] + \Delta U[n] \tag{3.32}$$

iii. The exchange-correlation:

$$E_{xc}[n] = T_C[n] + \Delta U[n] \tag{3.33}$$

The exchange correlation is supposed to account for the Pauli repulsion for electrons with similar spin and the correlation that compensates for the self-interactive term. Thus, the exact energy functional should be as by equation 3.34.

$$E[n] = T_S[n] + \int d^3\, r V_{ext}(\vec{r}) + E_H[n] + E_{XC}[n] \tag{3.34}$$

The variation equation for the exact functional is thus;

$$\frac{\delta E[n]}{\delta n(\vec{r})} = \frac{\delta T_S[n]}{\delta n(\vec{r})} + V_{ext}(\vec{r}) + e^3 \int d^3 \acute{r}\, [n] + E_{XC} \frac{n(\overrightarrow{\acute{r}})}{\left|\vec{r} - \vec{\acute{r}}\right|} = \mu \tag{3.35}$$

3.2.5 Pseudopotential Plane-Wave Method

The method solves the DFT by considering the valence electrons and treating the core electrons as frozen. Being frozen means that their charge density is never affected by the chemical processes in an atom. This approximation scheme is based on the fact that a pseudopotential is always weaker in the core region than the true coulomb potential of the nucleus and does not bear singularity to the nucleus. As a result, the pseudo wave functions at the core region become smooth and nodeless therefore, the pseudopotential and the pseudo waves can be presented using the plane-wave basis sets in which fewer electronic states are used in the calculation. The pseudopotential is generalized in such a way that they satisfy the norm conservation criteria which ensures that the charge concentration in the core region of the pseudo-atom is similar to that of the actual atom. For accurate results when using the plane-wave pseudopotential method, an accurate representation of the wave function from the basis sets is necessary. Based on the Bloch theorem, the Khon-Sham equation can be expanded in plane waves if the system is considered to be periodic, which gives a three-dimensional Fourier series expansion. The convergence of the expansion depends on the highest kinetic energy (kinetic energy cutoff value) of the plane wave when the series terminates.

3.2.6 Pseudopotentials

The pseudopotentials are formed based on the orthogonalized plane waves (OPW). In this case, the valence wave functions are expanded by utilizing the basis sets of plane wave functions that are orthogonal to the core states wave functions (φ_c) such that;

$$\emptyset_{OPW}(k+G) = \emptyset_{PW}(k+G) - \sum_{\alpha,c} < \varphi_c | \emptyset_{OPW}(k+G) > \varphi_{\alpha,c} \qquad (3.36)$$

Where $\emptyset_{PW}$ is the plane wave and $\emptyset_{OPW}$ is the corresponding orthogonalized plane and the sum is done over all the atoms and core states. From the above equation, a pseudopotential can be constructed by considering a Hamiltonian (H) with both the core (φ_c) and the valence (φ_v) wavefunctions. The pseudo-states for the system then can be presented as;

$$\varphi_{c(PS)} = \varphi_{\alpha,c} + \sum_{\alpha,c} a_{c,v}\varphi_{\alpha,c} \tag{3.37}$$

Applying the Hamiltonian in equation 3.37, above,

$$H\left|\varphi_{c(PS)}\right> = E_v\left|\varphi_{c(PS)}\right> + \sum_{\alpha,c} a_{c,v}(E_{\alpha,c} - E_v)|\varphi_{\alpha,c}> \tag{3.38}$$

Where $E_{\alpha,c}$ and E_v are the core and the valence eigenvalues respectively. By defining $a_{c,v}$ as: $a_{c,v} =< \varphi_{\alpha,c}|\varphi_{c(PS)} >$, we can have;

$$\left[H + \sum_{\alpha,c} a_{c,v}(E_v - E_{\alpha,v})||\varphi_{\alpha,c} >< \varphi_{v(PS)}|\ \right]\varphi_{v(PS)} = E_{v(PS)}\varphi_{v(PS)} \tag{3.39}$$

The pseudo-states satisfy the above equation which is similar to the Schrödinger equation by the introduction of the additional potential defined by:

$$V_R = \sum_{\alpha,c} a_{c,v}(E_v - E_{\alpha,v})||\varphi_{\alpha,c} >< \varphi_{v(PS)}| \tag{3.40}$$

The difference between the normal potential and V_R is based on the dependence of V_R on the valence eigenvalue (E_v). This additional potential to the initial potential V gives the Phillips-Kleinman pseudopotential which is defined by:

$$V_{tot} = V_R + V \tag{3.41}$$

Where V_{tot} is the Phillips-Kleinman pseudopotential.

3.2.7 Types of Pseudopotentials

The pseudo potentials can be classified into three types namely; the norm-conserving, ultra soft and projector-augmented waves (PAWs). The choice of any of the pseudo potentials depends on the accuracy desired when working in different systems.

3.2.8 Norm-Conserving Pseudopotentials

The basic requirement for this type of pseudopotentials is that the norm of the pseudo functions is the same as the norm of all electron wave function. This is supposed to ensure that the exchange-correlation energy that will be by the pseudopotential is very accurate. In order to achieve this, a non-local pseudo potential in which every angular momentum uses different potentials is used. The pseudopotential that use the non-local norm conserving pseudopotentials is able to describe the scattering properties associated with ions in different structures.

3.2.9 Ultrasoft Pseudopotential

In this type of pseudopotential the cutoff radius is made large than that of the norm conserving pseudopotential. This is supposed to be an approximation where the norm conservation constraints are relaxed. With this, the kinetic energy cutoff value is reduced resulting into smoother valence electrons. The smoothness of the valence electrons reduces the wave function describing the system thus making the solution of the Khon-Sham equation faster.

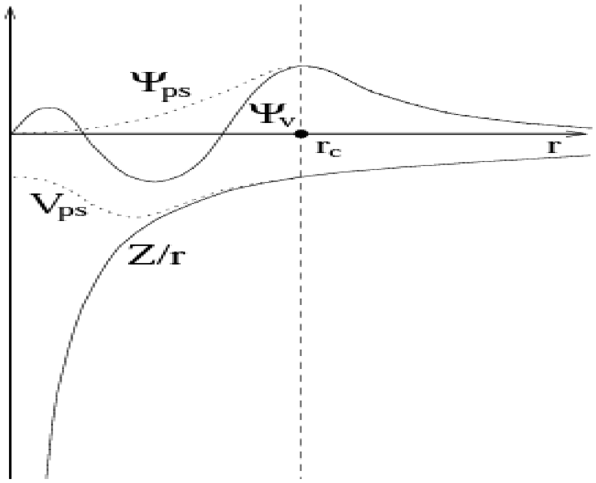

Figure 3.1: The graph of pseudo wave functions and all electron wave function and the pseudopotential and all electron potential as a function of radius.

The Figure 3.1 above presents the replacement of stronger ionic potential with the pseudo potential and this gives the same valence electron wave functions when the radius is greater than the critical radius (r_c) $(r > r_c)$. Beyond r_c, the scattering properties for both the pseudo and the all electron wave function become the same. Below the r_c the pseudo wave function has no nodes.

3.2.10 Electron Density

We consider N-electron particles in a Coulomb potential $V_{ext}(\vec{r})$ for a spin compensated system. The Hamiltonian for a many-body Schrodinger equation is presented as;

$$H = \sum_{i=1}^{N} \left[-\frac{\hbar^2}{2m} \nabla_i^2 + V_{ext}(\vec{r}_i) \right] + \sum_{i>j} \frac{e^2}{\vec{r}_i - r_j} \tag{3.42}$$

Taking the ground state energy E_0 to be a functional of the external potential (V_{ext}) we have V_{ext}: $E_0 = E[V_{ext}]$. Then we can easily transform the state $|\varphi >$ of the energy $E[\varphi]$ to the ground state $|\varphi_0 >$ of energy $E[\varphi_0]$. If we take the wave function of N electrons to be $\psi(\vec{r}_1, \dots\dots\dots\dots . \vec{r}_N)$, the electron density for the system will be given by;

$$n(\vec{r}) = N \int d^3r_2 \dots\dots\dots .. \int d^3r_N \left|\psi(\vec{r}_1, \vec{r}_2 \dots .. \vec{r}_{1,} \vec{r}_{N,}\right|^2 \tag{3.43}$$

The equation implies that if we have the Hamiltonian to solve the Schrodinger equation to get the wave function, we can be able to get electron density meaning$H \Rightarrow n(r)$. Similarly, we can use the wave function to get the Hamiltonian of a system $n(r) \Rightarrow H$. In this case, we consider an electron gas whose density is $n_0(\vec{r})$ and the corresponding Hamiltonian will take the form of:

$$H = \sum_{i=1}^{N}\left[-\frac{\hbar^2\nabla_i^2}{2m} - \frac{Ze}{|\vec{r}_i-\vec{R}|} + \sum_{i>j}\frac{e^2}{|\vec{r}_i-\vec{r}_j|}\right] \tag{3.44}$$

Where Z, and R are the positive charges of the nucleus and the position of the nucleus respectively. The number of electrons N is calculated by taking the integral over space of the electron density as;

$$N = \int d^3 n_0(\vec{r}) \tag{3.45}$$

And Z is determined by:

$$Z = \left[\frac{a_0}{2n_0\vec{r}}\,\frac{\partial n_0}{\partial r}\right] \tag{3.46}$$

Where a_0 is the Bohr radius of hydrogen. Hence with the knowledge of N and Z we can get $n(r) \Rightarrow H$. According to Hohenberg and Kohn in 1963, they generated the two possibilities and concluded that provided there is a fixed number of electrons, and arbitrary potential, both $n(r) \Rightarrow H$ and $H \Rightarrow n(r)$ is possible and it led to two theorems:

i. For degenerate ground states, two different Hamiltonian energy cannot have the same ground-state electron density. Therefore, it is possible to define the ground state energy as a functional of electron density $n(r)$; $E = E[n]$.

ii. $E(n)$ is minimal when $n(\vec{r})$ is the actual ground-state electron density.

The ground state energy is achieved by minimizing $E(n)$. This is possible by application of the Hohenberg and Kohn second theorem in which $E[n]$ is required to be minimum when the electron density $n(\vec{r})$ is at ground state with the condition that:

$$\int d^3 rn(\vec{r}) = N \tag{3.47}$$

This condition is achieved when we use the Langrage multiplier as follows:

i. A functional with a constraint is introduced on the electron density such that;

$$E[n] = \mu \int d^3\, rn(\vec{r}) \tag{3.48}$$

Where μ is the Langrage whose function is to maintain the number of electrons N.

ii. Another functional is also formed in which the Langrage is kept as a free parameter while searching for zeros:

$$0 = \frac{\delta}{\delta n(r)}\left[E[n] - \mu \int d^3\, rn(\vec{r})\right] = \frac{\delta E[n]}{\delta n(r)} - \mu \tag{3.49}$$

iii. The constraint μ is determined. At $T = 0K$ μ can be determined from the Fermi energy.

3.2.11 Vibrational Principle

The variation principle provides means of establishing approximations up to the lowest energy eigenstate and in some cases the excited states (McClean *et al.*, 2017; Slater & Johnson, 1972). Therefore it provides means in which wave functions can be better approximated. For the principle to be applied in solving the Schrödinger equation an appropriate Hamiltonian operator for the system is set. From the Schrödinger equation (3.42), it is important to note that actual information about a system is contained in the number of electrons N and the external potential V_{ext}. The external potential is determined by the position and charges of all the nuclei in a system. The other parts such as the electron-electron repulsion are not specific for a particular system. Considering an expectation value of a particular observable can be presented by the operator $\hat{x}$ and by using a complex wavefunction, the normalized equation takes the form.

$$< \hat{x} >= \int \ldots\ldots\ldots \int \boldsymbol{\varphi^{*}_{trial}} \hat{x}\, \varphi_{trail}\, dx_1 dx_2 \ldots\ldots\ldots dx_N = \langle \varphi_{trail} | \hat{x} | \varphi_{trail} \rangle \qquad (3.50)$$

Where φ^{*}_{trial} is the conjugate of φ_{trail} .

If the above equation is used to calculate in the calculation of energy as the expectation value of the Hamiltonian operator $\hat{H}$ then for any trial wave function (φ_{trail}) will be an upper bound to the true energy of the ground state and this is described by equation 3.51.

$$\langle \varphi_{trail} | \hat{H} | \varphi_{trail} \rangle = E_{trial} \geq E_0 = \langle \varphi_o | \hat{H} | \varphi_o \rangle \qquad (3.51)$$

Where φ_o and E_0 are the functions that gives the lowest energy and the lowest energy respectively.

For one to get the ground state energy, it is required that the functional $E[\varphi]$ be minimized by the way of searching the wave functions that fulfill the properties of a quantum mechanical wave function for the N electrons. This is supposed to make the normalization of equation 3.51 possible. The ground state energy can then be expressed by equation 3.52.

$$E_0 = \min_{\varphi \rightarrow N} E[\varphi] = \min_{\varphi \rightarrow N} \langle \varphi | T + V_{Ne} + V_{ee} | \varphi \rangle \tag{3.52}$$

Where $\varphi \rightarrow N$ is the allowed N electron wave function;

3.2.12 Ground State Properties

Total ground state energy helps to characterize important properties that can be used to give a full description of different materials. Some of these properties are discussed below.

3.2.13 Equation of state

It is based on the assumption that the first derivative of the pressure of a bulk modulus does not depend on the pressure but if it does the dependence is near negligible. This can be expressed by equation 3.53 such that;

$$\frac{\partial B}{\partial P} = B_O' = \int_V^{V_O} \frac{\partial B}{\partial P} \tag{3.53}$$

Where V_O is the equilibrium volume.

$$B(V) = B_o \left(\frac{V_o}{V}\right)^{B_o'} \tag{3.54}$$

By integrating V_O several times the equation lead

Repeated integration gives pressure of the system;

$$P(V) = \left[\frac{B_O}{B_O'} \left(\frac{V_O}{V}\right)^{B_O'} - 1\right] \tag{3.55}$$

The total energy involved then becomes.

$$E(V) = E_o + \frac{B_o}{B_o'} V \left(\frac{(V_o/V)^{B_o'}}{B_o'-1} + 1 \right) - \frac{B_o V_o}{B_o'-1} \qquad (3.56)$$

Where E_o is the energy at equilibrium volume.

The second-order equation of state is given by ;

$$\text{P(V)}=\frac{3}{2} B_o \left[(\frac{V_o}{V})^{\frac{7}{3}} - (\frac{V_o}{V})^{\frac{5}{3}} \right] \left\{ 1 + \frac{3}{4} (B_o' - 4) \left[(\frac{V_o}{V})^{\frac{2}{3}} - 1 \right] \right\} \qquad (3.57)$$

Equally, we can use the Morse type of equation of state. The total energy is fitted by an exponential function.

$$E(\omega) = a + be^{-\lambda\omega} + ce^{-z\lambda\omega} \qquad (3.58)$$

The equation is expressed in terms of Wigner-Seitz radius ω; $\lambda, a, b \; and \; c$ are the Morse parameters.

3.3 Exchange - Correlation Functional

3.3.1 Local Density Approximation

This approach provides means by which the exchange-correlation functional for a homogeneous electron gas can be approximated by the use of local density. For this method, the exchange-correlation functional is given by the equation;

$$E_{XC}^{LDA}[\rho] = \int \rho(r) \varepsilon_{XC}\,(r) dr$$

(3.59)

In which ε_{XC} represents the exchange-correlation energy of the homogenous electron gas moving around the nucleus without interactions and whose density is given by $\rho(r)$ at every point r. Local density assumes the absence of the derivative of $\rho(r)$ in the equation of the exchange energy functional which means it only applies in the situation where the electron density varies slowly with the position. Local spin-density approximation (LSDA) is an improvement on the local density approximation (LDA) to include the spin to ensure the Pauli Exclusion Principle is obeyed in the calculation. The accuracy of the function is much contributed by the fact that there exists cancellation of errors in the exchange and correlation estimations; LDA overestimates the E_X and underestimates E_C. The overestimation of E_X and underestimation of E_C is a result of the $\mathrm{LDA}_{\mathrm{XC}}$ hole satisfying the sum rule in the homogenous electron gas system as opposed to the individual exchange-correlation. This happens when the integrated error in the correlation cancels that in the exchange. LDA has the potential of achieving a high degree of accuracy for metallic solids whose electrons are delocalized. However, the LDA has a challenge when used for materials with strongly localized and correlated electrons such as the transition metal oxides and the rare earth metal compounds (Ernzerhof & Scuseria, 1999). For localized electrons, the functional overestimates the binding energies and underestimates the bonding distances between atoms.

3.3.2 Spin Local Density Approximation

The exchange-correlation function can be expressed in terms of the spin density instead of the electron density alone. The two spin densities ρ_α and ρ_β are in such a way that their sum is the total electron density of the system$\rho_\alpha + \rho_\beta = \rho$. From the theoretical point of view, the spin densities may not contribute much to the exact functional if the external potential does not depend on the spin but it adds the advantage of flexibility by having two variables instead of one. The spin functional has the advantage when dealing with a system with an even number of electrons which allows the breaking of symmetry. The spin local density approximation exchange-correlation energy is given by the equation $\rho_\alpha(r) = \rho_\beta(r) = \frac{1}{2}\rho$ (in the case of spin compensated situation) and we can have a spin-polarized case which is characterized by, $\rho_\alpha(r) \neq \rho_\beta(r)$ and the degree of spin polarization depends on the difference between the two. Polarization is given by the equation (3.60).

$$\xi = \frac{\rho_\alpha - \rho_\beta}{\rho}$$

(3.60)

Where ξ takes a value of zero for the spin compensated case and a value of one for fully spin polarization in the situation where the electron density comprises the same kind of spin.

3.3.3 Generalized-Gradient Approximations in Density-Functional Theory

The LDA only gives better estimations when dealing with a system of uniform electron distribution but is poorly estimated for non-uniform electron distribution. This means that the exchange-correlation energy $E_{XC}\rho(\vec{r})$ depends only on the electron density at all points in the system. The incorporation of the electron density gradient along with the electron density $\rho(\vec{r})$ in a functional known as the generalized gradient approximation GGA gives better results.

In the GGA method, the exchange-correlation energy $E_{xc}^{GGA}(\vec{\rho})$ is a function of the local spin electron densities and their gradients (Peverati & Truhlar, 2012).

$$E_{XC}^{GGA}\big(\rho(\vec{r})\big) = \int \rho(\vec{r})\varepsilon_{XC}\big(\rho(\vec{r})\big), \nabla\big(\rho(\vec{r})\big)\vec{r}$$

(3.61)

Generalized gradient approximation is a powerful tool in computational material science. Its strength is based on the improvement in the efficiency of local density approximation. The commonly used GGA approximation is based on the Perdew, Burke, and Ernzerhlo of the (PBE) functional. This approximation has the potential of correcting the interaction energies for massive molecules and solids and can give a better estimation of bond length irrespective of the bond strength. This new version of the GGA functional, which shares several properties with the exact exchange and correlation functional, has relatively good accuracy. However, the scheme tends to underestimate the bulk modulus in solid systems (Madsen & Singh, 2006). GGA in the computational study is implemented using the plane wave code in which the Fourier transform is used to the reciprocal lattice in space of the potential energy and density of the material. The accuracy of the GGA functional used depends on the type of pseudopotential used. The formation of the pseudopotential is moderated by its proper choice and that it will fit the all-electron system. A good cell parameter is obtained by matching the pseudo potential eigenvalues with a good wave function in the GGA and this is achieved by minimizing the cutoff radius in the pseudopotential (Rivero *et al*., 2015). The generalized gradient approximation is built by considering the exchange correlational functional, in which the exchange energy is considered in terms of the Coulomb interaction energy of an electron and its exchange-correlation hole. The application of GGA in computational DFT has been found to improve properties such as the ground state energy, bond length, and the dissociation energy for molecules and solids which are made up of light atoms (J. Sun et al., 2016; Yu *et al*., 2016). The lattice parameters calculated using GGA are found to agree with experimental results as opposed to those calculated using the LDA which are found to have an error of the range of 1-4% below the experimental value (Cococcioni et al., 2003). In the estimation of the exchange and correlation energies, the LDA and GGA are reported of having an error of 14% and 1% respectively.

3.3.4 Exchange Correlation and Band Gap Approximation

The application of the DFT using the LDA and GGA functional is known to underestimate the band gap of a crystal when the results obtained are compared with the experimental values (Marlow *et al*., 2018; Piskunov et al., 2004; Stampfl *et al*., 2001). If we consider an electron in the state Φ and assume that it is removed from the system such that;

$$E_N - E_{N-1} = \epsilon_\Phi$$

(3.62)

Where E_N is the total energy of the system having N electrons. Also, we can have a situation where an electron is added to a state say, $\emptyset$ which gives$E_{N+1} - E_N = \epsilon_\emptyset$. From the two equations, the band gap can be defined by the difference between the largest additional energy and the smallest removal energy. The energy gap is defined by the equation;

$$E_g = \epsilon_\emptyset - \epsilon_\Phi = E_{N-1} + E_{N+1} - 2E_N$$

(3.63)

In solid materials, this marks the onset of optical transition, in the event the gap is direct; where the lowest empty state and the highest occupied state lie in the same high symmetry points (Larson *et al*., 2007; Meng *et al*., 2017). The highest occupied and the lowest unoccupied states are called the highest occupied molecular orbital (HOMO) and lowest unoccupied molecular orbital (LUMO) respectively (Rajalakshmi *et al*., 2015; Silvarajoo *et* *al*., 2020). The additional and removal energy is referred to as electron affinity (A) and ionization potential (I) respectively. Because of the discontinuity of the exchange and correlation potential, then we can well say, E_g =I-A. This can be expressed by the equation;

$$E_g = \mu(N+\delta) - \mu(N-\delta) = \left.\frac{\delta E}{\delta n(r)}\right|_{N+1} - \left.\frac{\delta E}{\delta n(r)}\right|_{N-1}$$

(3.64)

Where $\delta \rightarrow 0$. The equation is substituted into the Khon-sham form for the energy functional given as, E$[n(r)]$. The Hartree and external potential do not play any part in the determination of the E_g of the system because they do not yield discontinuity. Considering a system of non-interacting electrons, only the kinetic term contributes the energy and the gap for such a system is given by the equation;

$$E_g^0 = \left.\frac{\delta T_0}{\delta n(r)}\right|_{N+1} - \left.\frac{\delta T_0}{\delta n(r)}\right|_{N-1} = \epsilon_{LUMO} - \epsilon_{HOMO}$$

(3.65)

It should be noted that the kinetic energy of the non-interacting electrons considered as a functional of density must have a discontinuous derivative when crossing an integer number of electrons. This makes it absolutely difficult to produce a functional of charge density for T_0 that can give results which are exact.

For the system comprising of interacting particles, the band gap energy can be expressed as;

$$E_g = \left.\frac{\delta T_0}{\delta n(r)}\right|_{N+1} - \left.\frac{\delta T_0}{\delta n(r)}\right|_{N+1} + \left.\frac{\delta E_{XC}}{\delta n(r)}\right|_{N+1} + \left.\frac{\delta E_{XC}}{\delta n(r)}\right|_{N-1} E_g^0 + E_g^{xc}$$

(3.66)

The above equation shows that the kinetic energy term is evaluated at the same charge density as the non-interacting system and so it coincides with the non-interacting system gap. From equation (3.66) it implies that the energy gaps calculated by DFT are not the same as the true gaps because they are lacking the E_g^{xc} term resulting from the XC functional. This is what leads to the underestimation of the band gap by the DFT.

3.3.5 Computational Methods

In this work, all the computational calculations were carried out in the framework of density functional theory (DFT) as implemented by the Quantum Espresso package. The atomic orbitals were expanded by the use of the plane wave basis sets. The plane wave pseudopotentials were used to treat the electron-ion interaction to reduce the computational cost by reducing the number of wave functions to be solved. We employed the local density approximation (LDA) and generalized gradient approximation (GGA) to calculate the ground state energy of the system. GGA in the computational study is implemented using the plane wave code and the pseudopotential method. The pseudopotential plane-wave self-consistency field package scripted within the Quantum Espresso code executed the self-consistency field calculations. The cut-off kinetic energy for the calculation was set at 60Ry after optimization of the simple orthorhombic structure. A full description of the valence electrons was achieved by using the PBE pseudo-potentials of Perdew-Burke-Enzenhof kind formulated by Vanderbilt code. The convergence threshold in the solution of the Khon-Sham equation was set at 10^{-12} (eV) for the self-consistency calculations. The valence configuration used for $GdBa_2Cu_3O_{7-x}$ was 4f7 5d1 6s2 for Gadolinium, 6s2 for Barium, 3d104s1 for Copper, and 2s2 2p4 for Oxygen. The Brillouin sampling was based on the Monkhost scheme. The K-point mesh in the Brillouin zone was set to 6× 6×2 generated based on the reciprocal scheme. During the optimization, the lattice parameters for the three axes were varied. A plot of energy versus cell dimensions was drawn to establish the minimum energy followed by minimizing other parameters. Proper atomic positions were established by relaxing their position (relax), and the proper volume was established by varying the cell volume (vc-relax). Relax, and vc-relax is calculations implemented by quantum espresso.

3.3.6 Computation of the Ground States

In most cases, there is aneed not to go about minimizing all the Khon-Sham states in the solution of the Schrödinger equation. Since the interest of solving the Schrödinger equation lies on the occupied bands only, there is a need to find a minimization method that will suit that interest and this is achieved through computation of the ground states.

3.3.7 The Ground State

The ground state energy forms the basis for calculating any physical property in the density functional theory (DFT) (Hafner & Wolverton, 2006; Mazin *et al.*, 2008). Therefore this quantity must be precisely calculated with efficiency and in a way that makes the computational cost in terms of time to be cheap.

3.3.8 The Total Ground State Energy and the Electron Density

For the DFT to properly make a good argument on the algorithm that it operates on, the total ground state energy must be self-consistence. This means that the input parameters must give the output which then is ploughed back as an input. For example, the occupied Khon-Sham states generate density which again depends on the potential which is generated from the density. Therefore the ground state will be only achieved when the self-consistence has been achieved. Based on the relationship between the ground state energy and the ground state density, it can be inferred that self-consistence can only be achieved at the minimum energy.

The process is done by starting with a set of wave functions $\Psi_{i,k}$ which generates a trial density $n(r)$. The trial density is then used to calculate the Khon–Sham $V(KS)$ and the starting energy E. The total energy is then minimized in relation to the wave function in the Khon-Sham potential to give another set of wave functions $\Psi_{i,k}$ which upon solution give a new ground state density $n(r)$ and new total energy E. This total energy is compared with the one for the previous iterations. In the event the energy is within the tolerance level, the convergence is assumed to have occurred since the energy variation between the cycles is within the tolerance level (convergence threshold). The flow chart showing the process is presented in Figure below;

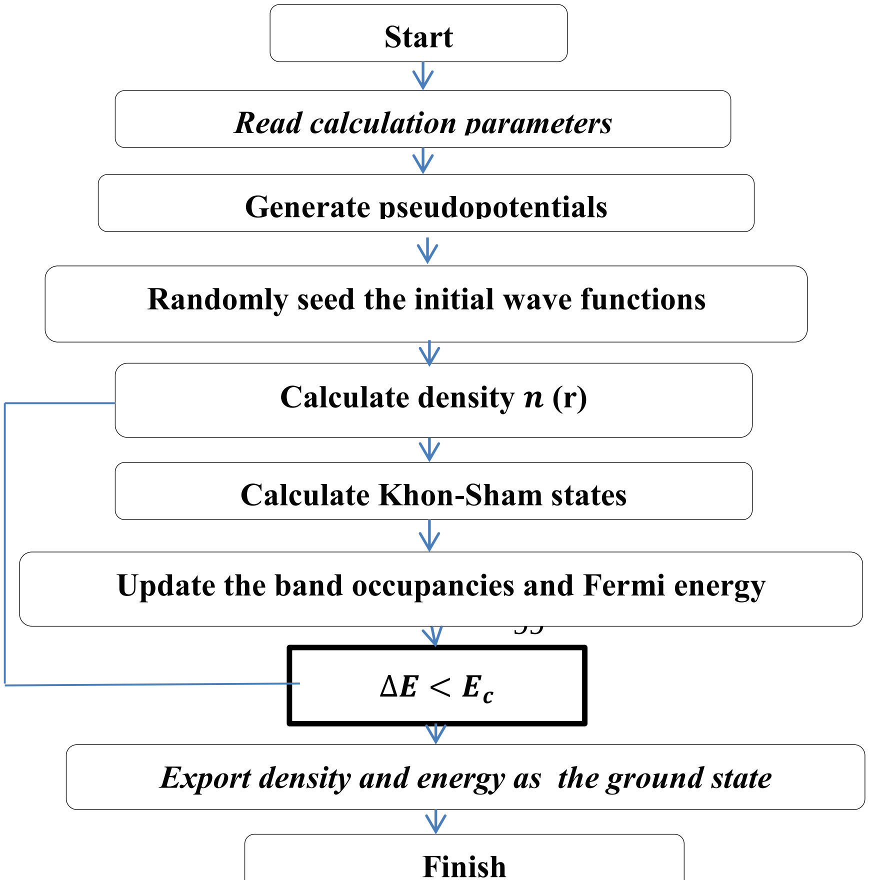

Figure 3.2: A flow chart diagram for the DFT computation process.

3.3.9 Wave Functions

The Khon-Sham wave function is the exact solution to an electron gas in the Khon-Sham equation. The equation can be solved by writing it in matrix form where it becomes an eigenvector problem and this is achieved through matrix diagonalization in which an assumption is that they will generate degenerate eigenvalues. In the matrix diagonalization, the direct matrix diagonalization is proportional to the n_{pw}^3 where n_{pw} is the number of the basis sets. By using plane wave basis sets, the value of n_{pw} may be approximately hundreds of thousands which is like to make the diagonalization become expensive in terms of the computational time required. Taking a Hamiltonian matrix to be of the form n_{pw}^2, the resulting direct diagonalization gives lower value of wave functions to the range of tens which is much lower than the occupied states. Another possible way to make the computation less expensive is by the use of the iterative technique. The technique provides a way in which the lowest number of wave functions can be found by direct minimization of their energy by the use of the Khon-Sham Hamiltonian. For a spin polarized system in insulators, the number of bands can be restricted to the number of the available electrons. But for metallic conductors, the number of electrons must be so large in order to cover for the bands which are normally partially occupied.

3.3.10 Real Space Grid

Since there is never enough memory to hold all the wave functions to be used in the computation process, a finite Fourier series is normally used. According to the Nyquist-Shannon sampling, the series is represented in the real space by the use of a discrete set of points. The points are able to represent all the wanted information stored in the Fourier series. Taking the Fourier space grid to be of the form; Nx, Ny, Nz components, then the real size of the space grid is given as $N_x \times N_y \times N_z$ On this, fast Fourier transform (FFT) uses the divide and conquer algorithm to reduce the computational complexity of the matrix. The fast Fourier transform operates in such a way that the number of coefficients is a small multiple of a small prime number. By application of the convolution theorem, those terms that are products of the wave function such as the electron density, high order Fourier components are usually produced to a magnitude that is twice those of the wave function. For this to be achieved the basis sets must be large and the real space must be fine. The finer grid plays a role in determining the derivative of quantities on the grid even in high order terms. Furthermore, the fine detail has got a small influence on the total energy and density of the system which makes it possible to limit the number of the Fourier series the product term to the number of the wave functions.

3.3.11 Reciprocal Space Sampling

There is always a need to sample the occupied electronic state by selecting some points in the Brillouin zone. The selection must be done accurately so that they can enable accurate solutions of the wave functions in a given system. In the solution of the Khon-Sham equation, the selected points interact with the electron density resulting in an efficiency solution of the Khon-Sham equation by keeping updates at the end of the Khon-Sham minimization. The usual criterion of sampling is by the use of the unbiased grid which bears evenly distributed points in a 3 dimensional grid called the Monkhurst-Pack grid. It is usually presented as $n \times n \times n$ and captures interactions between the nearest neighboring cells.

3.3.12 Orthonormality

For the proper solution of the Khon-Sham equation, the sampled electronic which are the eigenstate of the Hamiltonian are required to be orthogonal. However, orthogonality is never achieved by direct diagonalization of the Hamiltonian and therefore, must be imposed on the wave functions. This is made possible by the application of the orthogonalization scheme to both trial wave functions and to the direction of search by application of the Gram-Schmidt scheme. The scheme is chosen due to its simplicity and ease of implementation. Each vector in turn is orthogonalized to the set of vectors that have been already orthogonalised. This is done by calculating the 59 projectors of the vector onto this set and removing this projection from the original non-orthogonal vector.

3.3.13 Phase Transitions under Pressure

Technological advancement has made it possible to study material with wide variation of pressure thus altering the properties associated with the material. The changes in the material properties are attributed to the decrease in the inter atomic distances in the structure which can possibly lead to the material changing from a semiconductor to a metallic-like structure due to the close packing factors at higher pressure. Under high pressure, the material undergoes volumetric change and as a result, stability of the structure gets affectd. It is of great importance that the theoretical approaches and experimental approaches are used to accurately predict the stability of the polymorphic changes that are associated with the volumetric changes resulting from the bonding changes as a result of pressure. The density functional theory provides means of getting accurate estimation of the stable structure and the exact pressure when the material undergoes the phase transition. The experimental approach is limited to the magnitude of the applied pressure and the nature of the structure that can be formed. The degree of stability of the different phases in a solid state is determined by the free energy as a function of temperature and pressure or temperature and volume.

3.3.14 Structural Phase Transition

Phase transition can be expressed in terms of enthalpy as a function of pressure: This relationship is given by the equation;

$$H(P) = U(V,P) + \mathrm{PV} \tag{3.67}$$

Where H is the enthalpy, U is the internal energy, and V is the volume, Gadolinium Barium Copper Oxide occurs in orthorhombic and tetragonal phases (Cankurtaran *et al*., 1990; Stolyarova *et al*., 1992) in which the orthorhombic phase is the most stable. Polymorphic phase transition can occur with increased pressure under which a material changes from one step to another (Goryainov *et al*., 2005; Ma *et al*., 2009; Wei *et al*., 2019). Therefore, the orthorhombic phase changes to the tetragonal phase at high pressure. The induced stress reduced the volume and the lattice parameter for the crystal lattice, resulting in a variation in the total energy. The effect on the volume change was attributed to the evolution of the atomic positions to their equilibrium position for all the atoms in the crystal. This led to crystal deformation by the placement of the particles in their new atomic positions. The relationship between the changes in the atomic position vector was established by the equation;

$$R = x + ER_0$$

(3.68)

The term x represents the displacement of a particle within the crystal and ER_0 is the strain tensor deformation in its six-component vector. To establish the stability of the two structural phases, it was better to do aproper calculation of the Gibbs free energy (G) which is given by equation 3.69 (Doan *et al.*, 2020);

$$G = E_0 + PV + TS$$

(3.69)

The equation (3.69) above implies that at the structural phase transition, the Gibbs free energy is equal to the enthalpy because the computational calculations were carried out at $T = 0K$. The minimal computed enthalpy implies the stability of the material (F. Otto *et al*., 2013; T. Zhu & Gao, 2014).

The total energy as a function of the reduced volume (V/Vo) is related to pressure by Murnaghan’s equation of state (EoS) given by;

$$P = 1.5B_O\left[\left(\frac{V_O}{V}\right)^{\frac{7}{3}} - \left(\frac{V_O}{V}\right)^{\frac{5}{3}}\right][1 + 0.75\left(B_O^{'} - 4\right)(\left\{\frac{V_O}{V}\right\}^{\frac{2}{3}} - 1)]$$

(3.70)

Where P is the applied pressure, V_O is the volume at zero pressure, V is the reduced volume upon application of pressure, B_O is the bulk modulus and $B_O^{'}$ is the derivative of the bulk modulus with respect to pressure. The ground state energy was then obtained using the energy equation 3.71 given below;

$$E(V) = E_o + \frac{9V_OB_O}{16}\left\{[\left((\frac{V_O}{V})^{\frac{2}{3}}\right) - 1]^3B_o^I + [(\frac{V_O}{V})^{\frac{2}{3}} - 1]^2(6 - 4(\frac{V_O}{V})^{\frac{2}{3}}]\right\}$$

(3.71)

The above equations were used to calculate the reduced volume, ground state energy, and enthalpy for the material under hydrostatic pressure.

The electronic density of state was used as the basic quantity in describing the electronic structure of the material. The total number of the available state are calculated on the assumption that every electron is behaving as a homogenous electron gas. The electronic states are then presented in the form of a vector in K-space.

The energy associated with a single electron in the system is given by;

$$E = \frac{\hbar^2}{2m}\left(k_x^2 + k_y^2 + k_z^2\right) = \frac{\hbar^2}{2m}|\boldsymbol{K}|^2$$

(3.72)

This means, for vectors that have the same magnitude, their energy is supposed to be the same. As opposed to classical treatment where all energies are allowed, for quantum consideration, the uncertainty and Pauli's exclusion principles are applied to get the discrete energy states. This means that the chosen wave functions must satisfy the time independent Schrödinger equation in relation to the boundary conditions. DOS is characterized by the degeneracy factor in which it is possible for some allowed energy levels; there can be two or more combinations of the k-space yielding the same energy. DOS for a crystalline material is expressed by the equation;

$$g(E) = \frac{2}{V_{BZ}} \sum_n \int \delta\big(E - E_n(\boldsymbol{k})\big)\, d\boldsymbol{k}$$

(3.73)

Where the integral is over the volume in the reciprocal space covering all the k-points in the reciprocal space and n represents the band index. Factor two accounst for the spin up and spin down in accordance with Pauli's exclusion principle. The sum is over the bands.

For a crystalline structure that comprises more than one atom type the contribution of each atom to the total density of state can be assessed by considering the projected density of states of the atoms and the orbital contribution from each of them. The projected density of state for atom h is given by;

$$g_l^t(E) = \frac{2}{V_{BZ}} \sum_n \int Q_l^t \delta(E - E_n(\boldsymbol{k})) d\boldsymbol{k}$$

(3.74)

Where Q_l^t is the partial charge of the atom while l is the index representing specific orbitals. The contribution of each orbital of the projected DOS to the total DOS is established by matching the two. Of interest are those which contribute most to the DOS and give the characteristic electronic structure for the material. Apart from the DOS, the band structure is also used to characterize the electronic structure properties of a material by evaluation of the band gap, Fermi level, and the Fermi energy. In a band structure, the energy of electronic state is presented along lines (bands) in a reciprocal space obtained from the sampled k-points.

In this study, the electronic structure properties and the DOS for $GdBa_2Cu_3O_{7-x}$ were calculated using the optimized lattice parameters. The Khon-Sham equations were expanded on a plane wave basis set up to a kinetic energy cutoff value of 60Ry by iterative self-consistent field calculations in a k-grid of 6x6x2.

3.3.15 Convergence of the PwSCF

The optimized kinetic cutoff energy determines the number of basis sets to be used in an SCF calculation. By application of the Bloch theorem in electronic states, the electron wave function can be given as by equation;

$$\psi_k(r) = \sum_G C_{k,G} exp[i(k+G).r] \tag{3.75}$$

Where G is the reciprocal vector for the reciprocal space. The kinetic energy for each state is given by the equation;

$$E = \frac{\hbar^2}{2m}$$

(3.76)

By truncating the infinite sum in equation 3.72 above, the kinetic energy is related to the kinetic cutoff energy by the equation;

$$\frac{\hbar^2}{2m}|k+G|^2 < E_{ecut}$$

(3.77)

Where the E_{ecut} is the cutoff kinetic energy and the sum takes the form of an equation;

$$\psi_k(r) = \sum_{|k+G|<G_{ecut}} C_{k,G} exp[i(k+G).r]$$

(3.78)

The kinetic cutoff value used for this work was 60 Ry for the orthorhombic phase of the $GdBa_2Cu_3O_{7-x}$ crystalline structure. For convergence to be achieved the real space is related to the reciprocal space by equation;

$$\frac{\Omega}{(2\pi)^3}\int H(k)dk = \frac{1}{\acute{\Omega}}$$

(3.79)

Where Ω and $\acute{\Omega}$ represent the volumes in the real space and reciprocal space respectively while IBZ is the irreducible Brillioun zones. For this computational work, the integration of the Brillioun zone was done by the use of upshifted the Monkhorst-Pack scheme grid of k-points 6x6x2. The Monkhorst-Pack scheme grid is popular for DFT computational because it has the advantage of giving a uniform set of points expressed by the equation;

$$k_{n1,n2,n3} = \sum_{i}^{3} \frac{2n_i - N - 1}{2N} G_i$$

(3.80)

Where G is a vector representing the reciprocal space and $n_i = 1, 2, \ldots\ldots..N$. for materials without band gap or those with a very narrow band gap, the k-grid becomes discontinuous about the Fermi surface and they may make the convergence of the total energy to take more time. To solve this problem, we apply the smearing method and for this study we applied the Gaussian smearing since the material has a narrow band gap.

3.3.16 Calculation of the Elastic Constants

The elastic constant gives information on how a material responds to stress resulting from the applied energy in solid materials. The basic law is Hooke's law which defines the second-order elastic constants that are generalized to give the third-order elastic constants. The theory also addresses the effect of crystal symmetry in characterizing elastic properties.

The strain is set in such a way that the volume does not change except for the bulk modulus. This is because the total energy is determined by volume more than strain and this ensures that the two do not contribute to strain. The strain and stress matrix is expressed as:

$$\varepsilon = \begin{bmatrix} \varepsilon_1 & \frac{\varepsilon_6}{2} & \frac{\varepsilon_5}{2} \\ \frac{\varepsilon_6}{2} & \varepsilon_2 & \frac{\varepsilon_4}{2} \\ \frac{\varepsilon_5}{2} & \frac{\varepsilon_4}{2} & \varepsilon_3 \end{bmatrix}$$

(3.81)

$$\sigma = \begin{bmatrix} \sigma_1 & \sigma_6 & \sigma_5 \\ \sigma_6 & \sigma_2 & \sigma_4 \\ \sigma_5 & \sigma_4 & \sigma_3 \end{bmatrix}$$

(3.82)

The energy change for the strain is given by:

$$E(\varepsilon_1, \varepsilon_2 \dots \dots \dots \dots \dots \varepsilon_6) = E_o + \frac{1}{2} V \sum_{i,j=1,6} C_{ij}\, \varepsilon_i \varepsilon_j + Z(e^3)$$

(383)

Where the energy of the unstrained lattice is $Z(e^3)$ denotes the term proportional to e^k with k≥ 3 and the vector $r = (x, y, z)$ representing the dimensions of the lattice under strain are transformed to $r' = (x', y', z')$.

3.3.17 Stress

When a body is subjected to some external force of a given magnitude, there is a corresponding introduction of internal forces within the body that tend to exert force on every part of the surrounding, and the body is said to be in a state of stress. Stress is considered to be homogenous if the forces acting on the surface of the body together with the orientation of the body are not dependent on the position of the particles in the body.

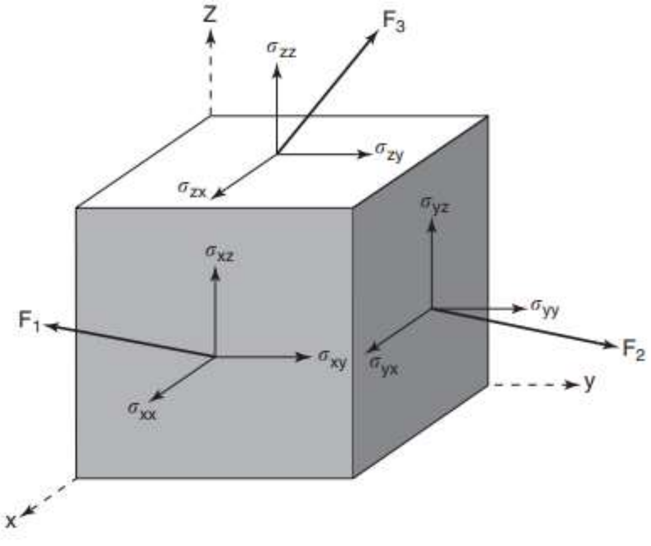

Figure 3.3: The Figure represents the force components in a body under stress (Keaton, 2018).

Figure 3.3 above gives the force components acting on the planes of the body which represent the stress components on the body surface. The stress component σ_{ij} represents the force component tending to the direction $+x_i$ and directed from the face that is normal to $+x_j$. The σ_{ii} components form the normal stress component while σ_{ij} components where $\sigma_{ij} \neq j$, form the shear stress component on the body. The σ_{ij} components are of a second-rank tensor and thus can be expressed in a 3x3 matrix form;

$$\sigma = \begin{bmatrix} \sigma_{xx} & \sigma_{yx} & \sigma_{zx} \\ \sigma_{xy} & \sigma_{yy} & \sigma_{zy} \\ \sigma_{xz} & \sigma_{yz} & \sigma_{zz} \end{bmatrix}$$

(3.84)

The positive value for σ_{ii} infers tensile stress acting on the body while the negative value for σ_{ii} infers compressional stress. For the body to acquire the state of equilibrium, the infinitesimal volume elements within the body must achieve a state of mechanical stability. Meaning the net force acting on each element reduces to zero and this can be expressed as:

$$\sum_{i=1}^{3} \sigma_{ij} + f_i = 0$$

(3.85)

Where f_i is the i^{th} componemt of the external force per unit area. Since no net torque will be acting on the body at the equilibrium state, the shear components will be related by;

$$\sigma_{ij} = \sigma_{ji}$$

(3.86)

3.3.18 Strain

The strain is a property that tells the deformation that the body undergoes due to the applied stress. Consider a particle in the body occupying a reference point defined by $\boldsymbol{r} = \sum_{i=1}^{3} x_i \widehat{n_i}$. The coordinates are referred to as the Lagrangians of the system. When subjected to stress, a particle at point $\boldsymbol{r}$ shifts to another position $R = \sum_{i=1}^{3} X_i \widehat{n_i}$. The displacement of the particle is defined as $u(r) = \boldsymbol{R} - \boldsymbol{r}$**.** This describes the vector field occupied by a particle in the reference configuration. From this perspective, the position of the neighboring particle can also be described as $\boldsymbol{r} + \Delta\boldsymbol{r}$ and the new positions will be expressed as;

$$\boldsymbol{R} + \Delta\boldsymbol{R} = \boldsymbol{r} + \Delta\boldsymbol{r} + u(\boldsymbol{r} + \Delta\boldsymbol{r})$$

(3.87)

From the above equation, the displacement of the neighboring particle is given by;

$$\Delta\boldsymbol{R} = \Delta\boldsymbol{r} + u(\boldsymbol{r} + \Delta\boldsymbol{r}) - u(r)$$

(3.88)

And the individual component displacement;

$$\Delta\boldsymbol{X_i} = \Delta\boldsymbol{x_i} + u_i(\boldsymbol{r} + \Delta\boldsymbol{r}) - u_i(r)$$

(3.89)

If $\Delta\boldsymbol{r}$ **i**n equation 3.82 tends to zero such equation can be written as;

$$u_i(r - \Delta r - u_i(r) \approx \sum_{j=1}^{3} \frac{\partial u_i(r)}{\partial x_i} \Delta x_j$$

(3.90)

The displacement gradient resulting from the body strain is given by;

$$\alpha_{ij} = \frac{\partial u_i(r)}{\partial x_j}$$

(3.91)

Each component in the new position becomes;

$$\Delta X_i = \Delta x_i + \sum_{j=1}^{3} \alpha_{ij} \Delta x_j$$

(3.92)

$$\text{And } \; d\boldsymbol{X} = (1 + \alpha) d\boldsymbol{x}$$

(3.93)

The above equation implies that the deformed configuration X can be established provided the reference matrix $\boldsymbol{x}$ and $\boldsymbol{\alpha}$ are known. If the particle, whose displacement is given by the vector**,** is assumed to be in an infinitesimal neighborhood, then the deformation of the resulting configuration can be expressed in terms of the held positions. The square of the length $d\boldsymbol{R}$ becomes;

$$|d\boldsymbol{R}|^2 = d\boldsymbol{R}.d\boldsymbol{R} = d\boldsymbol{X}^{\boldsymbol{2}} d\boldsymbol{X} = |dr|^2 + dx^T 2\eta dx$$

(3.94)

In which η is given by;

$$\eta = \frac{1}{2}(\alpha + \alpha^T \alpha)\epsilon$$

(3.95)

This can also be expressed as;

$$\boldsymbol{\eta_{ij}} = \frac{\mathbf{1}}{\mathbf{2}}\left(\boldsymbol{\alpha_{ij}} + \boldsymbol{\alpha_{ji}} + \sum_{\boldsymbol{k=1}}^{\mathbf{3}} \alpha_{kj}\alpha_{kj}\right)$$

(3.96)

The matrix element η is the Lagrangian strain matrix and gives a full description of how a body undergoes deformation through the displacement of particles from their equilibrium state and gives a measure of how the new configuration of the particle differs from the original. Homogenous deformation occurs when the Lagrangian strain $\boldsymbol{\eta}(r)$ remains constant under stress, and this is only achieved when α_{ij} remains constant or $\boldsymbol{u}$ becomes directly proportional with $\boldsymbol{r}$**.** In terms of the symmetric (ϵ) and antisymmetric strain (ω) matrix, the Lagrangian strain can be expressed as;

$$\eta_{ij} = \epsilon_{ij} + \frac{1}{2}\sum_{k=1}^{3}(\epsilon_{ik}\epsilon_{kj} + \epsilon_{ik}\omega_{kj} - \omega_{ik}\epsilon_{kj} - \omega_{ik}\omega_{kj})$$

(3.97)

Where $\alpha_{ij} = \epsilon_{ij} + \omega_{ij}$

From the above equation, it can be inferred that if the magnitude of ϵ_{ij} and ω_{ij} tends to zero, the value $\boldsymbol{\epsilon}$ is a better approximation of $\boldsymbol{\eta}$**.** If $\epsilon = 0$, then $\alpha = \omega$ and thus**;** $d\boldsymbol{X} = (1 + \omega)dx$. In such a situation, the square of displacement is given as;

$$|d\boldsymbol{R}|^2 = dx^T(\boldsymbol{1}+\boldsymbol{\omega})^T(\boldsymbol{1}+\boldsymbol{\omega})dT = dx^2dx = |dr|^2$$

(3.98)

Where ω is the rotational deformation and does not affect the interparticle distance in the deformed body. ϵ is the physical strain, and the particle in the body under this strain undergoes displacement from their equilibrium configuration. The degree of displacement upon deformation is given by the physical strain tensor such that the Lagrangian strain is given by;

$$\eta = \epsilon + \frac{1}{2}\epsilon^2$$

(3.99)

Finally, the strain is related to the stress by the Lagrangian stress ($\boldsymbol{\tau}$) expressed as;

$$\boldsymbol{\tau} = \det(1+\epsilon)\,(1+\epsilon)^{-1}.\sigma.(1+\epsilon)^{-1}$$

(3.100)

Where σ is the physical stress.

3.3.19 Polycrystalline Elastic Properties

A material is considered to be polycrystalline when it comprises many crystals grains with random orientation within a crystal. The bulk modulus B and the shear modulus G give the directional properties for the isotropic crystal. The Young's modulus E and the Poisson's ratio are calculated using the following equations:

$$B = \frac{9BG}{3B+G}$$

(3.101)

$$v = \frac{3B-2G}{2(3B+G)}$$

(3.102)

For accurate calculation of the elastic moduli, averaging methods based on the computed elastic constants are used. The methods are:

3.3.20 The Voigt and Reuss Averaging Method

Elastic constants describe a crystal lattice that is continuous and periodic without any grain boundary in between. Due to the random variation of the grain orientation, a polycrystalline solid material may be considered to be isotropic with uniform values of elastic constants in all directions. The ability of the material to resist deformation under stress is associated with the averages of the bulk and shear moduli. To determine how the stress and strain are distributed in a polycrystalline solid, the aggregate average of the Voigt and Reuss are two extreme cases are considered: letting the uniform strain in the polycrystalline solid to be equal to the external strain (Voigt approximation) and the uniform stress to the equal to the external stress (Reuss approximation).

The Voigt average method operates on the assumption that the strain will remain constant, while the Reuss average operates on the assumption that the stress will remain constant during deformation. The Voigt averages are based on elastic constants, while the Reuss averages are based on elastic compliance. The averages are given by;

$$B_V = \frac{1}{9}[(C_{11} + C_{22} + C_{33}) + (C_{12} + C_{13} + C_{123})]$$

(3.103)

$$G_V = \frac{1}{15}[(C_{11} + C_{22} + C_{33}) - (C_{12} + C_{13} + C_{23}) + 3(C_{44} + C_{33} + C_{66})]$$

(3.104)

The Reuss averages are given by:

$$B_R = [(S_{11} + S_{22} + S_{33}) + 2(S_{12} + S_{13} + S_{23})]^{-1}$$

(3.105)

$$G_R = \left[15[4(S_{11} + S_{22} + S_{33}) - (S_{12} + S_{13} + S_{23}) + 3(S_{44} + S_{55} + S_{66})]\right]^{-1}$$

(3.106)

3.3.21 The Hill's Average

According to Hill, the Voigt and Reuss moduli are upper and lower bound, respectively, hence the Bulk and shear moduli can be calculated by using the upper and the lower limits.

$$B_H = \frac{B_V + B_R}{2}$$

(3.107)

3.3.22 Born Stability Criterion

According to the criterion, the softening of the shear moduli causes instability in the crystal structure and can lead to distortion. For a crystal at equilibrium, the free energy associated with elasticity is given as;

$$E = \frac{1}{2}\sum_{i,j} C_{ij} e_i e_j$$

(3.108)

For a lattice to be stable, the free energy should be positively defined concerning the strains e_i and e_j respectively. The condition for this to be achieved is that the constant elastic matrix must be positive. If in the computation of the constant elastic one or more eigenvalues become zero the crystal will tend to instability resulting from the lattice distortions to the symmetry of the eigenvector. For the simple orthorhombic crystal of $GdBa_2Cu_3O_{7-x}$, which has a lower symmetry and a relatively high number of the independent elastic constants, the diagonalization of the constant elastic matrix gives eigenvalues that satisfy the Born stability criteria by the conditions given as;

$$C_{ii} > 0 (i = 1,4,5,6) > 0, (C_{22} + C_{33} - 2C_{23}) > 0, (C_{11} + C_{22} - 2C_{12}) > 0,$$

$$\frac{1}{3}(C_{12} + C_{13} + C_{23}) < B < \frac{1}{3}(C_{11} + C_{22} + \ C_{33})$$

(3.109)

From the criteria, it is noticed that the trivial eigenvalues for the matrix C44, C55, and C66 need to be positive for the criteria to represent a stable crystal condition.

3.3.23 Lattice Optimization

A crystal structure is fully described by the length of the primitive vectors$a$, b and c and the angles between the primitive vectorsα, β andγ. For proper relaxation of the lattice parameter to minimize the ground state energy, different optimization cycles are undertaken in each degree of freedom in a systematic sequential way. Every step in the sequence involved minimizing the ground state energy to the volume, $\frac{b}{a}$ and $\frac{c}{a}$ Ratios and the angles α, β and γ.

For the volume optimization, the lattice parameters a, b, and c undergo the same percentage degree of distortion. To achieve this, we used the deformation matrix presented as;

$$\begin{pmatrix} \frac{1}{\sqrt{1+\epsilon}} & 0 & 0 \\ 0 & 1+\epsilon & 0 \\ 0 & 0 & \frac{1}{\sqrt{1+\epsilon}} \end{pmatrix}$$

(3.110)

Where ϵ is the physical strain on the body, the volume of the crystal at equilibrium is calculated from the least square fit of Birch-Murnaghan's equation of state:

$$E(V) = E_0 + \frac{9V_0B_0}{16}\left\{\left[\left(\frac{V_0}{V}\right)^{\frac{2}{3}} - 1\right]^3 \acute{B}_0 + \left[\left(\frac{V_0}{V}\right)^{\frac{2}{3}} - 1\right]^2 \left[6 - 4\left(\frac{V_0}{V}\right)^{\frac{2}{3}}\right]\right\}$$

(3.111)

Where E_0, B_0, and $\acute{B}_0$ are the minimum energy, the bulk modulus, and the derivative of the bulk modulus for pressure. Optimization of the $\frac{b}{a}$ the ratio was done in such a way the volume of the crystal and the ratio $\frac{c}{a}$ Remain unchanged.

To get the equilibrium physical strain, a fourth-order polynomial fit on the energy function was done for all the distorted points within the structure. Optimization of the $\frac{c}{a}$ ratio was achieved by maintaining the volume and $\frac{b}{a}$. The ratio was unchanged during the deformation. The angle α is measured between the length primitive vectors b and c. During the optimization process, the volume is maintained unchanged. The deformation matrix used for this optimization is given by;

$$\begin{pmatrix} \frac{1}{1-\epsilon^2} & 0 & 0 \\ 0 & 1 & \epsilon \\ 0 & \epsilon & 1 \end{pmatrix}$$

(3.112)

The equilibrium angle is obtained by the fourth-order polynomial fit on the energy function. The angle β which is measured between the length primitive vectors a and c is optimized by using the deformation matrix that maintains the volume of the crystal. The matrix is given as;

$$\begin{pmatrix} 1 & 0 & \epsilon \\ 0 & \frac{1}{1-\epsilon^2} & 0 \\ \epsilon & 0 & 1 \end{pmatrix}$$

(3.113)

The equilibrium angle is obtained by the fourth-order polynomial fit on the energy function. The angle γ is a measure between the length of primitive vectors b, and c. The deformation matrix used to optimize this angle was (Ravindran et al., 1998);

$$\begin{pmatrix} 1 & \epsilon & 0 \\ \epsilon & 1 & 0 \\ 0 & 0 & \frac{1}{1-\epsilon^2} \end{pmatrix}$$

(3.114)

The fitting procedure was done the same way as for the other parameters to get the equilibrium angle. Then, the exact process is repeated until proper equilibrium parameters are obtained.

3.3.24 Computation of the Elastic Constant by the Code

The calculation of the elastic constant for this work adopted the criterion of a full potential linear muffin-tin orbital method and use the exchange correlations; local density approximation (LDA) and generalized gradient approximation (GGA) (Ravindran et al., 1998). Before undertaking the computation, structural optimization for the parameters of the simple orthorhombic structure by use of the LDA and the GGA was performed. The initial values for optimization were adopted from the experimental values and upon optimization there was a good match between the obtained value and the other experimental values. Optimization was properly achieved by minimizing the enthalpy of the system. This is done by varying the lattice vectors while maintaining the angle and the atomic positions of the atoms in the crystal in a fixed position. The equilibrium volume contribution to the total energy assumes zero-point movement of the particles and no thermal expansion upon application of stress by applying the volume conserving strains. the equilibrium elastic constants were calculated from the equilibrium relaxed structure in accordance with the volume conserving strains, by allowing the internal degree of freedom through the cell relaxation and evaluating the changes in the total energy resulting from the strain in relation to its magnitude. After distortion, the crystal was relaxed to achieve an equilibrium state in which no force was acting on any atom. The elastic constants were then calculated by variation of strain to the equilibrium position of the lattice parameters. For crystalline solids, the change in energy as a result of strain is given by:

$$\Delta E = \frac{V}{2} \sum_{i=1}^{6} \sum_{j=1}^{6} C_{ij} e_i e_j$$

(3.115)

Where V represents the volume of the cell before distortion, ΔE is the change in energy resulting from strain for the vectors $e = (e_1, e_2, e_3, e_{4,} e_{5,} e_{6,})$ and C_{ij} is the elastic constant matrix.

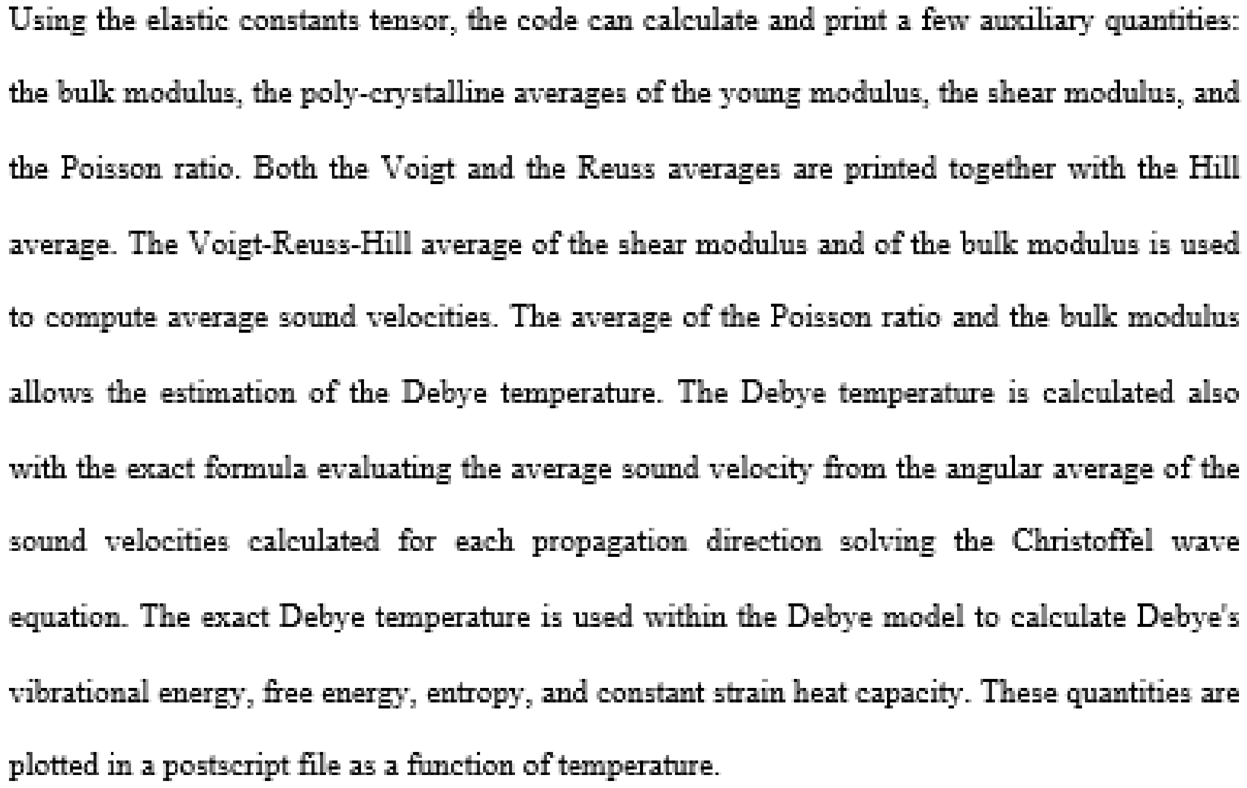

Using the elastic constants tensor, the code can calculate and print a few auxiliary quantities: the bulk modulus, the poly-crystalline averages of the young modulus, the shear modulus, and the Poisson ratio. Both the Voigt and the Reuss averages are printed together with the Hill average. The Voigt-Reuss-Hill average of the shear modulus and of the bulk modulus is used to compute average sound velocities. The average of the Poisson ratio and the bulk modulus allows the estimation of the Debye temperature. The Debye temperature is calculated also with the exact formula evaluating the average sound velocity from the angular average of the sound velocities calculated for each propagation direction solving the Christoffel wave equation. The exact Debye temperature is used within the Debye model to calculate Debye's vibrational energy, free energy, entropy, and constant strain heat capacity. These quantities are plotted in a postscript file as a function of temperature.

3.3.25 Elastic Constants of an Orthorhombic Crystal

For this crystal structure, the Bravais lattice vector in the form of the lattice parameters is given by (Ravindran et al., 1998):

$$R = \frac{1}{2}\begin{pmatrix} \frac{\sqrt{3}}{2} & \frac{1}{2} & 0 \\ \frac{\sqrt{3}}{2} & \frac{1}{2} & 0 \\ 0 & 0 & \frac{c}{a} \end{pmatrix}$$

(3.116)

A linear combination of the elastic constant can be determined by straining the vector R according to the relationship: $\acute{R} = RD$ in which case, R is the matrix containing the lattice vectors and D is a matrix representing the symmetric distortion of the system.

The orthorhombic crystal has nine independent elastic constants and therefore, it requires nine strains to correspond to the nine distortions. The nine strains correspond to nine distortions given below (Ravindran et al., 1998):

$$D_1 = \begin{pmatrix} 1+\delta & 0 & 0 \\ 0 & 1+\delta & 0 \\ 0 & 0 & 1 \end{pmatrix}$$

(3.117)

The energy change associated with this distortion is given by:

$$\frac{\Delta E}{V_0} = (C_{11} + C_{12})\delta^2$$

(3.118)

This type of distortion leads to compression or expansion of the lattice with conservation of the symmetry but there is a change in the volume. The second distortion is presented as;

$$D_2 = \begin{pmatrix} \frac{1}{\sqrt[3]{1+\delta}} & 0 & 0 \\ 0 & \frac{1}{\sqrt[3]{1+\delta}} & 0 \\ 0 & 0 & \frac{1}{\sqrt[3]{1+\delta}} \end{pmatrix}$$

(3.119)

This distortion gives symmetry conserving variation of c/a. The ratio of the energy change to volume is given by the equation;

$$\frac{\Delta E}{V_0} = (\tau_1 + \tau_2 + \tau_3)\delta + \frac{1}{9}(C_{11} + C_{12} - 4C_{13} + 2C_{33})\delta^2$$

(3.120)

Where τ_i is an element in the stress tensor.

The third distortion is given by:

$$D_3 = \begin{pmatrix} \frac{1+\delta}{\sqrt[3]{1-\delta^2}} & 0 & 0 \\ 0 & \frac{1-\delta}{\sqrt[3]{1-\delta^2}} & 0 \\ 0 & 0 & \frac{1}{\sqrt[3]{1-\delta^2}} \end{pmatrix}$$

(3.121)

The ratio of the energy change to volume for this distortion is given by:

$$\frac{\Delta E}{V_0} = (\tau_1 - \tau_2)\delta + \frac{1}{9}(C_{11} - C_{12})\delta^2$$

(3.122)

This type of distortion acts in a way that elongates side a of the crystal with proportionality that ensures the volume of the crystal is not changed. The equation (3.119), (3.120), and

(3.22) were used to calculate the elastic constants C_{11}, C_{33}, and C_{33} respectively.

$$\frac{\Delta E}{V_0} = \tau_1\delta + \frac{C_{11}\delta^2}{2}$$

(3.123)

$$\frac{\Delta E}{V_0} = \tau_2\delta + \frac{C_{22}\delta^2}{2}$$

(3.124)

$$\frac{\Delta E}{V_0} = \tau_3\delta + \frac{C_{33}\delta^2}{2}$$

(3.125)

The obtained elastic constants will change the volume of the crystal but still, the crystal will remain orthorhombic. To ensure the conservation of volume, volume conserving shear distortions D_1, D_2, and D_3 are used to get C_1, C_2, and C_3 respectively.

$$D_4 = \begin{pmatrix} \frac{1}{\sqrt[3]{1-\delta^2}} & 0 & 0 \\ 0 & \frac{1}{\sqrt[3]{1-\delta^2}} & \frac{1}{\sqrt[3]{1-\delta^2}} \\ 0 & \frac{1}{\sqrt[3]{1-\delta^2}} & \frac{1}{\sqrt[3]{1-\delta^2}} \end{pmatrix}$$

(3.126)

$$D_5 = \begin{pmatrix} \frac{1}{\sqrt[3]{1-\delta^2}} & 0 & \frac{1}{\sqrt[3]{1-\delta^2}} \\ 0 & \frac{1}{\sqrt[3]{1-\delta^2}} & 0 \\ \frac{1}{\sqrt[3]{1-\delta^2}} & 0 & \frac{1}{\sqrt[3]{1-\delta^2}} \end{pmatrix}$$

(3.127)

$$D_6 = \begin{pmatrix} \frac{1}{\sqrt[3]{1-\delta^2}} & \frac{1}{\sqrt[3]{1-\delta^2}} & 0 \\ \frac{1}{\sqrt[3]{1-\delta^2}} & \frac{1}{\sqrt[3]{1-\delta^2}} & 0 \\ 0 & 0 & \frac{1}{\sqrt[3]{1-\delta^2}} \end{pmatrix}$$

(3.128)

The ratio of change in energy to volume for the distortions D_1, D_2 and $D_3$are given as:

$$\frac{\Delta E}{V_0} = 2\tau_4\delta + 2C_{44}\delta^2$$

(3.129)

$$\frac{\Delta E}{V_0} = 2\tau_5\delta + 2C_{55}\delta^2$$

(3.130)

$$\frac{\Delta E}{V_0} = 2\tau_6\delta + 2C_{66}\delta^2$$

(3.131)

D_7, D_8 and D_9 are calculated using the volume conserving orthorhombic distortion matrices given as:

$$D_7 = \begin{pmatrix} \frac{1}{\sqrt[3]{1-\delta^2}} & 0 & 0 \\ 0 & \frac{1}{\sqrt[3]{1-\delta^2}} & \frac{1}{\sqrt[3]{1-\delta^2}} \\ 0 & \frac{1}{\sqrt[3]{1-\delta^2}} & \frac{1}{\sqrt[3]{1-\delta^2}} \end{pmatrix}$$

(3.132)

$$D_8 = \begin{pmatrix} \frac{1}{\sqrt[3]{1-\delta^2}} & 0 & \frac{1}{\sqrt[3]{1-\delta^2}} \\ 0 & \frac{1}{\sqrt[3]{1-\delta^2}} & 0 \\ \frac{1}{\sqrt[3]{1-\delta^2}} & 0 & \frac{1}{\sqrt[3]{1-\delta^2}} \end{pmatrix}$$

(3.133)

$$D_9 = \begin{pmatrix} \frac{1}{\sqrt[3]{1-\delta^2}} & \frac{1}{\sqrt[3]{1-\delta^2}} & 0 \\ \frac{1}{\sqrt[3]{1-\delta^2}} & \frac{1}{\sqrt[3]{1-\delta^2}} & 0 \\ 0 & 0 & \frac{1}{\sqrt[3]{1-\delta^2}} \end{pmatrix}$$

(3.134)

The D_7 has an effect of increasing a and b with equal magnitude while c remains constant. The D_8 the distortion as an effect of increasing and decreasing c with an equal amount while b remains constant. The D_9 has an effect of increasing b and decreasing c with the same magnitude while a remains constant. The implication of the said behavior is that the collective effect of D_7, D_8, and D_9 distortions in a strained crystal is similar the that of a crystal that is not strained.

3.3.26 Bulk Modulus of Crystal

Considering a single crystal, the independent elastic constants can be used to calculate the bulk modulus along the crystallographic axes of a given crystal. Taking the strain normal to the stress in a given direction to be the same, then the bulk modulus can be defined by the equation:

$$B = \frac{\Delta}{(1+\sigma+\beta)^2}$$

(3.135)

Where $\Delta = C_{11} + 2C_{12}\sigma + C_{22}\sigma^2 + 2C_{13}\beta^2 + 2C_{23}\sigma\beta$

The orthorhombic crystalline structure has the values for σ and β given has

$$\sigma = \frac{(C_{11}-C_{12})(C_{33}-C_{13})-(C_{23}-C_{13})(C_{11}-C_{13})}{(C_{33}-C_{13})(C_{22}-C_{12})-(C_{13}-C_{23})(C_{12}-C_{23})}$$

(3.136)

$$\beta = \frac{(C_{22}-C_{12})(C_{11}-C_{13})-(C_{11}-C_{12})(C_{11}-C_{12})}{(C_{22}-C_{12})(C_{33}-C_{13})-(C_{12}-C_{23})(C_{13}-C_{23})}$$

(3.137)

The elastic bulk moduli along the a, b, and c axes of the crystal are given by:

$$B_a = a\frac{dP}{da} = \frac{\Lambda}{1+\theta+\vartheta}$$

(3.138)

$$B_b = b\frac{dP}{db} = \frac{B_a}{\theta}$$

(3.139)

$$B_c = c\frac{dP}{dc} = \frac{B_a}{\vartheta} \qquad (3.140)$$

θ and ϑ represents the directional change of b and c in relation to a.

CHAPTER FOUR

RESULTS AND DISCUSSIONS

4.1 Structural phase Stability of $GdBa_2Cu_3O_{7-x}$

The structural optimization was done on the lattice parameters and atomic positions. The parameters that were optimized are the cell dimensions, the kinetic cutoff energy, and the K-points. The optimized parameters confirmed that $GdBa_2Cu_3O_{7-x}$ is a simple orthorhombic crystal in a stable state. To assess the stability of the crystal the Goldschmidt tolerance factor (t_f) was used and is given in equation 4.1 (Article *et al*., 2015);

$$t_f = \frac{\frac{R_{A_1}+R_{A_2}}{2}+R_O}{\sqrt{2}(R_B+R_O)} \qquad (4.1)$$

Where R_{A_1} and R_{A_2} are the radii for the Gd and Ba occupying site A of the crystal structure.

For the orthorhombic crystal, the value for a stable structure is supposed to be less than unity $(t_f < 1)$. The ionic radii that were used for the calculation were; 1.05 Å, 1.42 Å, 0.73 Å, and 1.4 Å, for Gd, Ba, Cu, and O respectively. The tolerance factor was found to be 0.8747 which means the structure was stable. The equilibrium lattice constant was estimated by fitting a curve of volume versus energy to determine the minimum energy with respect to the volume of the crystal using the Birch–Murnaghan equation of state (Christensen *et al*., 2010; Jayalakshmi *et al*., 2005; Mahesh *et al*., 2013). The total ground state energy as a function of volume is presented in Figure 4.1. Figure 4.2 confirms the accuracy of the computation by having the volume at zero pressure same as that in Figure 4.1. The corresponding lattice parameters are presented in Table 4.1. The observed decrease in the cell parameters with pressure can be explained in terms of reduced compression in the crystal structure as a result of repulsion among the atoms. The degree of change of the lattice parameters is not the same in all directions because the interatomic distances differ in different directions.

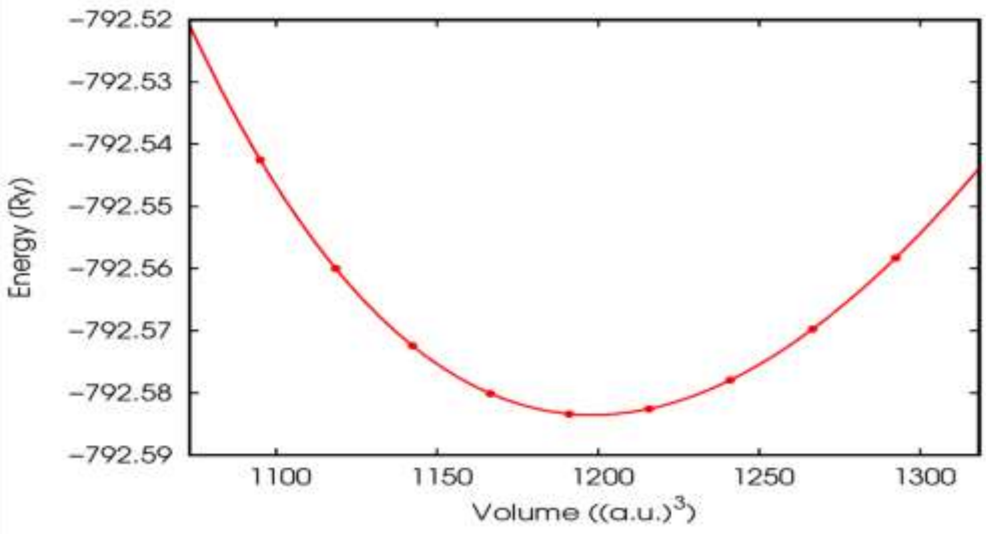

Figure 4.1: A fit of the total ground state energy as a function of volume.

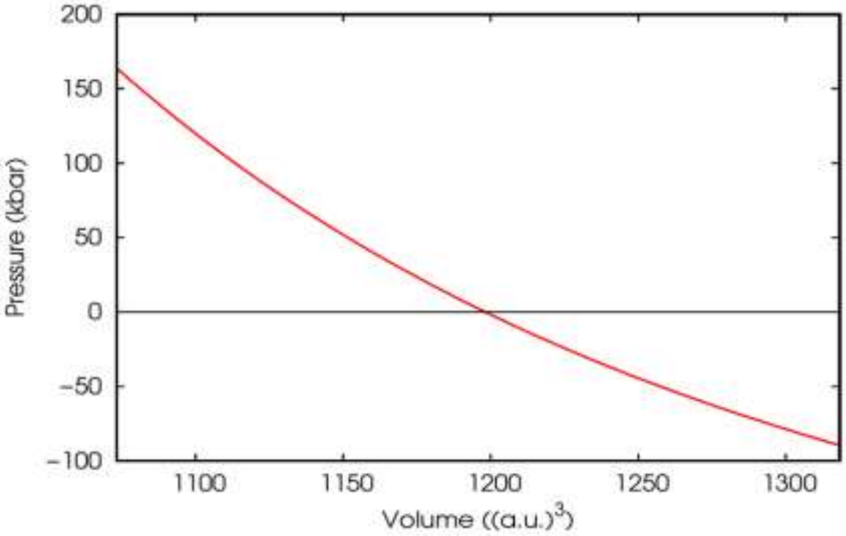

Figure 4.2: A fit of pressure as a function of volume.

The minima of the fit of Figure 4.1 gives the ground state energy corresponding to the input parameters used in the computation. The ground state energy is ~792.56 Ry and the used cell dimensions gave a volume of ~1200(a,u)^3. The result of Figure 4.2 is a confirmatory measure for the accuracy of the curve plotted in Figure 4.1. Zero pressure coincides with the curve at a volume of ~1200(a,u)^3. With the confirmation, the crystal structure is deemed to have been properly optimized.

Table 4.1: The computed lattice parameters under the influence of pressure.

$P(GPa)$	a	b	c
0	7.2611	7.4614	22.7207
5	7.1770	7.2911	22.4276
10	7.0843	7.1360	20.7924
15	7.0620	7.0423	20.4080
20	7.0075	7.0617	19.9982
25	6.9214	7.0023	19.5662
30	6.8933	6.9610	19.2881
35	6.7625	6.7750	20.2198
40	6.7076	6.5137	18.2949

The crystal structure of the $GdBa_2Cu_3O_{7-x}$ (Figure 4.3) represents a unit cell crystal. Along the b axis of the structure, there exists the CuO ion which is a characteristic feature for all layered cuprate superconductors. It is observed that each of the copper iono in the crystal structure is surrounded by the oxygen atom. At the center of the CuO_2 layer there is the Gd ion. The BaO ion separates the CuO_2 layer, and remains attached to the CuO plane. Table 4.2 represents the normalized atomic positions in the unit cell crystal.

Table 4.2: The normalized atomic positions in the crystal cell.

Atom	X	Y	Z	Atomic position
Gd	0.5	0.5	0.5	Center
Ba	0.5	0.5	±0.18	Center
Cu1	0	0	0	Edge
Cu2	0	0	±0.355	Edge
O1	0	0	±0.159	Edge
O2	0.5	0	±0.378	Face
O3	0	0.5	±0.378	Face
O4	0	0.5	0	Edge

The results from the above table represent the ordering of the atoms and how the bond lengths vary in the crystal. The properties of the crystal are determined by the atomic position of each of the atoms which vary as indicated in the table.

From Figure 4.3, Cu1 and O4 combine to form CuO ion while the Cu2, O2, and O3 are loosely held to form the two CuO_2 planes. The O1 exists inside the crystal and combines with Ba to form BaO. Gd remains unattached to any atom in the crystal. The greater contribution of the material to superconductivity is basically as a result of the O1 atom. This is because of its existence in the vacancy created between the CuO_2 planes and the CuO chain.

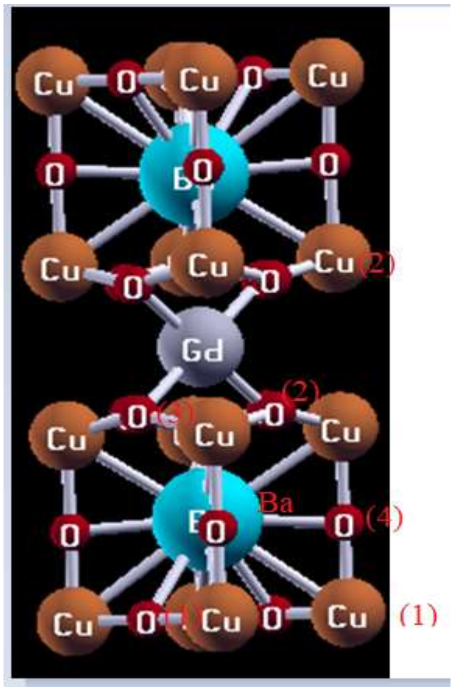

Figure 4.3: The crystal structure of $GdBa_2Cu_3O_{7-x}$ indicates the bonding of the different atoms based on the coordinates of the atoms.

From the crystals above, the ordering of atoms is the same in the upper and the lower layer of the crystal. Upon optimization, the equilibrium lattice parameters were found to be 3.848Å, 3.948Å, and 11.702Å for a, b, and c respectively. At zero pressure this compared well with the experimental results reported (W. Zhang & Osamura, 1991).

The fact that the experimental value at zero pressure did not vary so much from the computational values qualifies the validity of the computational technique used. Lattice parameters were also measured from the output of calculations done at different pressure to assess the degree of hardening brought about by the applied hydrostatic pressure. The summary of the calculated lattice parameter with respect to varying pressure is given in Table

4.1 which were achieved through, relax and variable cell relax calculation within the quantum espresso code at different pressure.

The relationship between $\frac{\mathrm{a}}{\mathrm{a}_0}$, $\frac{\mathrm{b}}{\mathrm{b}_0}$, $\frac{c}{c_0}$, and $\frac{\mathrm{V}}{\mathrm{V}_0}$ in which a_0, b_0, c_0, and V_0 are equilibrium lattice parameters and the volume of a relaxed structure under the influence of hydrostatic pressure was also computed. The plot for the relationship is shown in Figure 4.4. The decreasing variation is in agreement with the previously reported experimental work for other cuprate perovskite (Christy *et al.*, 1994; Comodi *et al.*, 1990; Lin *et al.*, 2012). The side percentage contraction of *b* and *c* is greater than that of side, meaning *b* and *c* are easily compressed and their porosity is relatively high than that of side a because of the anisotropic nature and anisotropic linear compressibility of the HTSC (Fietz & Wuhl, 1990; Sato & Naito, 1997)

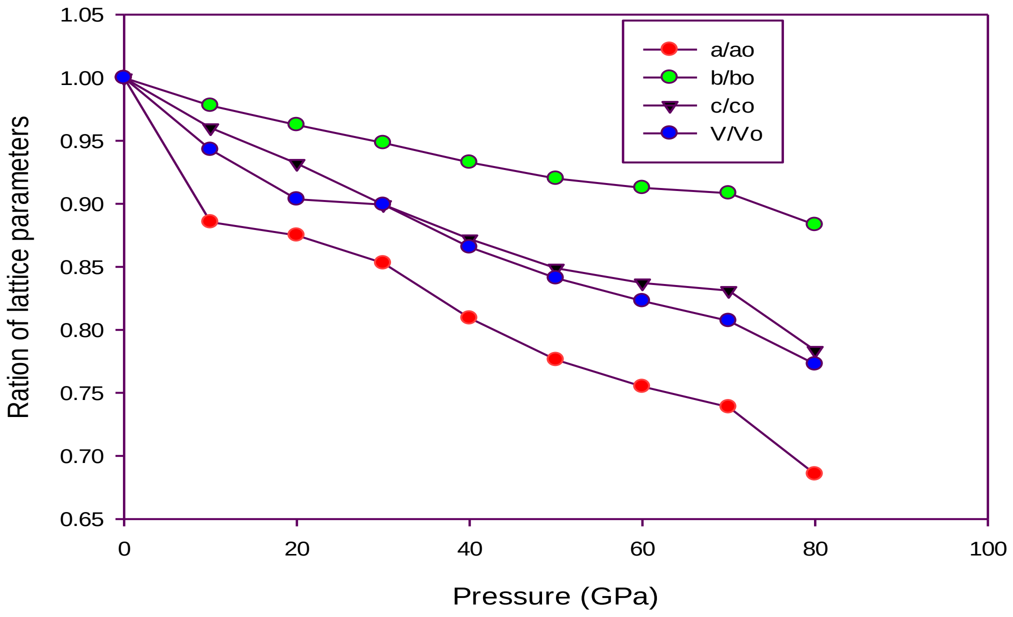

Figure 4.4: Variation of volume and cell parameters with pressure (GPa).

Site b undergoes a small change under the influence of pressure as compared to a and c. The percentage change is near ~30%.

4.2 Structural Phase Transition under Pressure

It was noted that the ground state energy of the tetragonal phase at zero pressure is high than that of the orthorhombic and the reverse happens as the pressure increases. Figure 4.5 and Figure 4.6 respectively, imply that the tetragonal phase cannot withstand high pressure and hence become unstable as the pressure increases. This is in agreement with the work reported by (Noor *et al*., 2017; Pu *et al*., 2020). In their study of polymorphic structural phase changes under different conditions of pressure, a characteristic small value of ground state energy at zero pressure was noted in comparison with the corresponding other phases. And a reverse happens at the transition temperature. The same can be confirmed from Figure 4.8, immediately after phase transition, in which the calculated enthalpy is the same for the two phases, the orthorhombic phase takes a lower value of enthalpy. Meaning the orthorhombic phase is the most stable phase than the tetragonal phase.

The transition pressure is estimated to be at a point in which the minimum energy and volume are the same or nearly the same for the two phases as shown in Figure 4.7. Before and after the phase transition, the minimum energy for the two phases is different as shown in Figures 4.5 and 4.6 respectively. From the DFT calculation in this work, the transition pressure is estimated to be 21.95GPa as shown in Figure 4.8, a point at which the enthalpy for the two phases is the same. The orthorhombic phase gets compressed beyond the said transition pressure, gets distorted, and will not bear its characteristic properties.

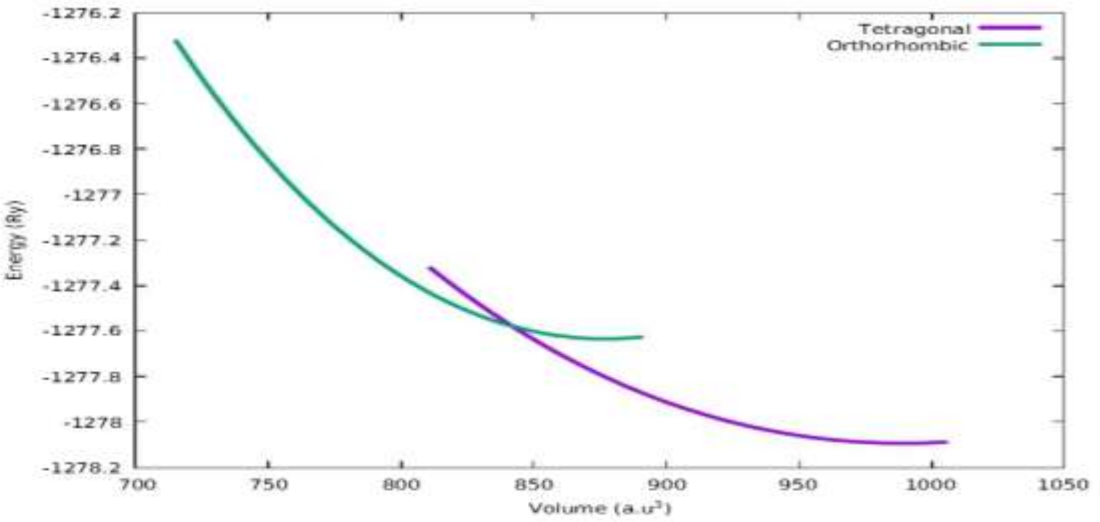

Figure 4.5: A graph of energy versus volume at zero pressure.

As shown in Figure 4.5, the plot indicates different values of minimum energy. The difference in volume at minimum energy is also more pronounced.

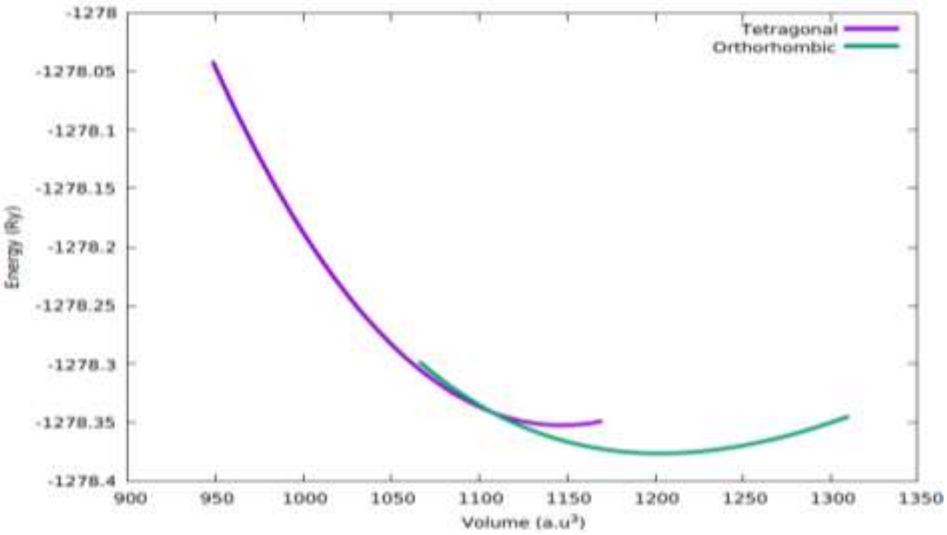

Figure 4.6: A graph of energy versus volume at 10GPa pressure.

It has been shown from Figure 4.6 that there exist different values of minimum energy for the two phases but the difference in volume in smaller compared to that at zero.

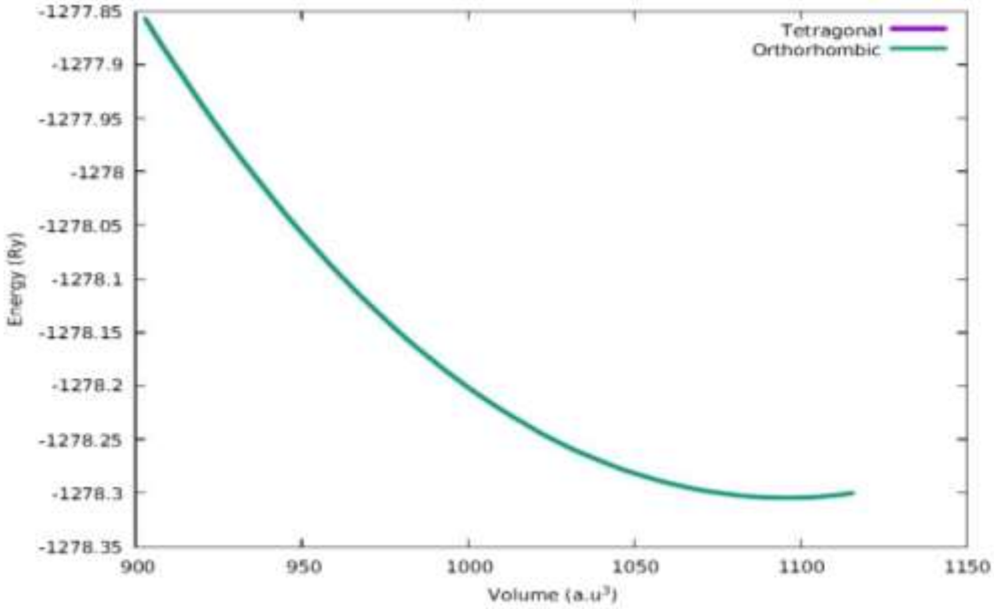

Figure 4.7: A graph of energy versus volume at 20 GPa pressure.

It is indicated In Figure 4.7 that the minimum energy for the two phases is nearly the same. This is the approximate pressure at which the phase transition occurs.

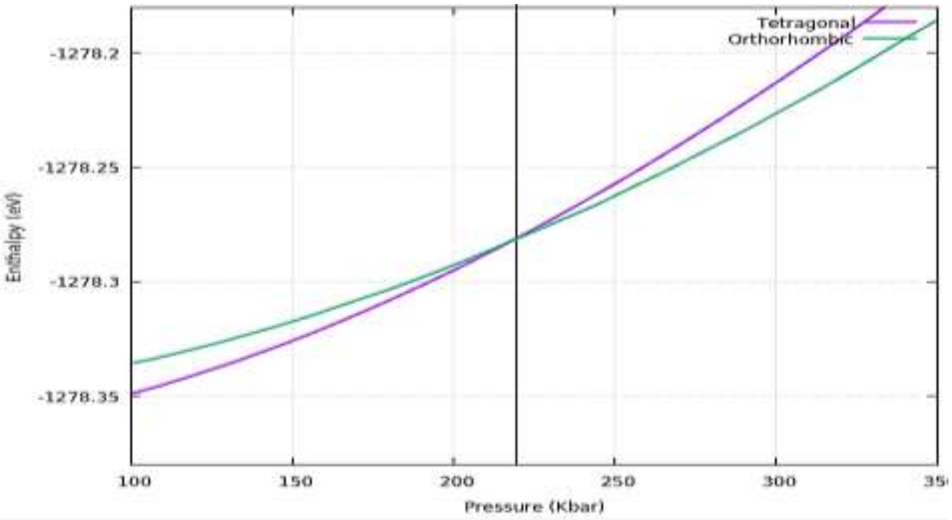

Figure 4.8: A graph of enthalpy as a function of pressure.

For the superconductors and other materials that undergo structural phase transition, at the point of phase transition, the two crystals must have equal free energy (Urry, 2004; Zein *et al*., 2010). The state of superconductivity depends on the balance between the two free energies and the deviation from the two leads to no superconductivity meaning that superconductivity entirely depends on the crystal structure (Bardeen & Stephen, 1964; Klemm & Clem, 1980; Lafarge *et al*., 1993).

4.3 Electronic Structure Properties

In terms of electronic structure analysis of materials, semiconducting properties are considered as the changes that occur during semiconductor to conductor transition. The changes are brought about by the interactions that happen in the occupied states in the band and the conduction states (Schabel & Park, 1998; Siebentritt *et al*., 2010; Xu *et al*., 2010). The definition of the electronic structure depends on the total contribution of the electrons and holes in the structure and also the induced effects such as doping.

4.3.1 Band Structure Calculation

The band structure was calculated at Γ, X, Z, U, Y, S, T, and R high symmetry points. At zero pressure a direct band gap of 0.78eV is formed at around the T symmetry point (Figure 4.9). With increasing pressure, the gap closes and the structure undergoes metallization. This relates well with what has been reported in studies done on superconducting perovskites under different conditions of pressure (Granhed et al., 2020; Noor *et al*., 2017; Pu *et al*., 2020). This is explained in terms of the hardening of the crystal lattice with pressure hence affecting the distance between the holes and the electrons in the structure. As a result, there is a columbic potential change which triggers a different patterns of motion by the particles.

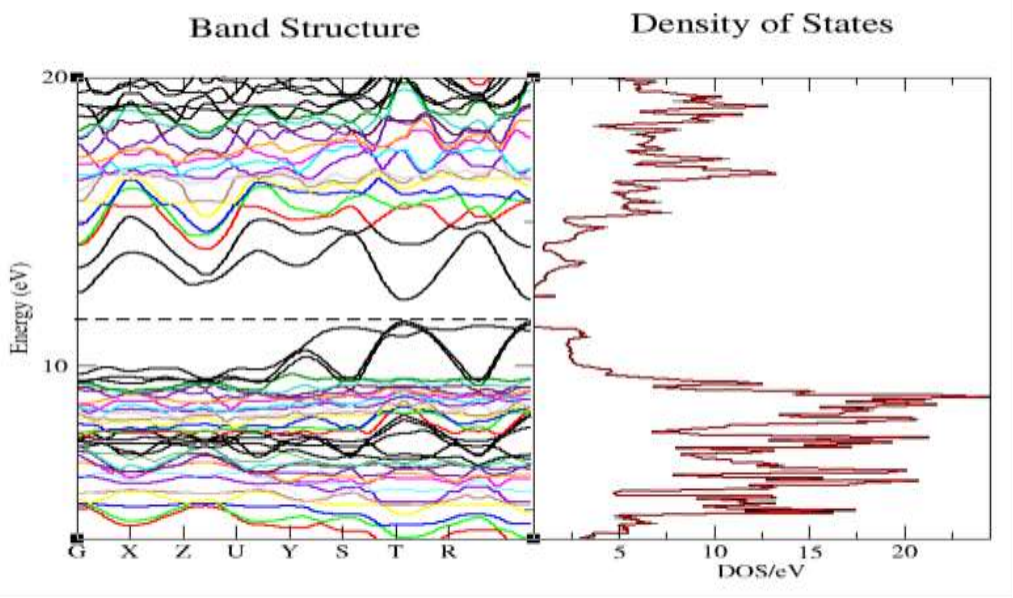

Figure 4.9: Band structure and the partial density of state at zero pressure.

The dotted line in the band structure represents the highest occupied state in the valence band. The bands structure and the density of state compare well. At zero pressure the single valence band which is just below the conduction band is a result of Cu 1d as can be seen in the combined graph of PDOS and DOS structure in Figure 4.13. The two bands appearing below the band gap are dominated by Ba 2P and Gd 5P. At zero pressure the conduction band is empty but dominated by Cu 1d and oxygen O 2P. The Cu 1d and O 2P combine to form the Cu-O chain that appears in the undoped structure of $GdBa_2Cu_3O_{7-x}$.

As the pressure increases there is overlapping between the valence band and the conduction band which can be attributed to the broadening of the band width of the 1s, 2p and 1d atomic orbital as shown in Figure 4.10. This is because of their strong interaction with neighboring atoms which creates wider bands than the energy gap and this avails electrons to the conduction band. There is a considerable value for the density of states at the Fermi level at the metallization pressure. This means that the Fermi energy increases with an increase in pressure. Therefore, it is an indication that pressure can lead to semiconductor to conductor transition. The changes in the band structure and density of state at different pressure in relation to Fermi energy is shown in Figure 4.10.

As observed in Figure 9 at pressure zero, two peaks are formed in the valence and conduction band near the Fermi level. This has an influence on the density of state as it makes it have a high affinity for oxygen vacancy population at the Fermi energy. This information is important in the calculation of the density of state at the Fermi level. The Fermi level increases as the pressure increases as observed in other reported work and in Figure 4.11.

The Fermi energy are 12.432eV, and 19.457eV for zero and 50 GPa applied pressure as shown in Figure 4.11 (a) and (b) respectively. The Fermi level increases with increasing pressure. The Fermi energy dependence on pressure can be expressed by equation 4.2 (Shan et al., 2013):

$$E_g(P) = E_g(0) - \beta P$$

(4.2)

Where β is the pressure coefficient which defines the shift in the position of the valence and conduction band with variation in pressure (Óò *et al*., n.d.).

The shift position of the valence and conduction band results in to change in Fermi energy which can be expressed as a function of temperature by equation 4.3 (N. Lee *et al.*, 1997).

$$E_F(P,T) = \frac{E_g(P)}{2} + \frac{3}{4} K_B T ln \frac{m_h^\star}{m_e^\star}$$

(4.3)

Where E_F is the Fermi energy, E_g the energy gap, K_B is Bolzmann's constant, T is the absolute temperature, $m_h^\star$ mass of the hole, and $m_e^\star$ the mass of an electron.

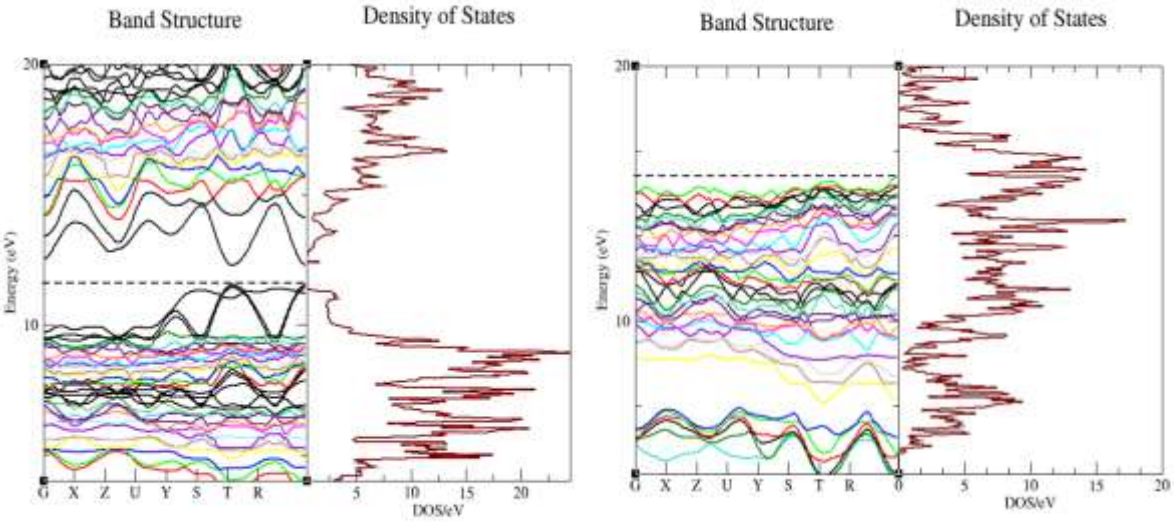

Figure 4.10: Density of state and band structure for GdBa$_2$Cu$_3$O$_7$ for the pressure of 0Gpa and 50GPa.

a **b**

Figure 4.11: Induced pressure dependence of the Fermi energy. From the plots **a** and **b** represents calculations at done at 0GPa and 50GPa respectively.

The relationship between the Fermi energy and increasing pressure is shown in Figure 4.11 Indicate how pressure can lead to a change in the superconductivity transition temperature.

There is a continued increase in Fermi energy with increased pressure provided the structure has not undergone distortion. The direct proportionality of the Fermi energy with pressure and temperature results in increased kinetic energy of the particles at high pressure. This is for unstrained crystals. For a strained crystal, the behavior is different as seen in Figure 4.12 where a strain is applied to the structure. When both the strain and the stress are applied to the structure, a strained Fermi energy is liberated and a plot of the applied pressure against the strained Fermi energy is presented in Figure 4.12.

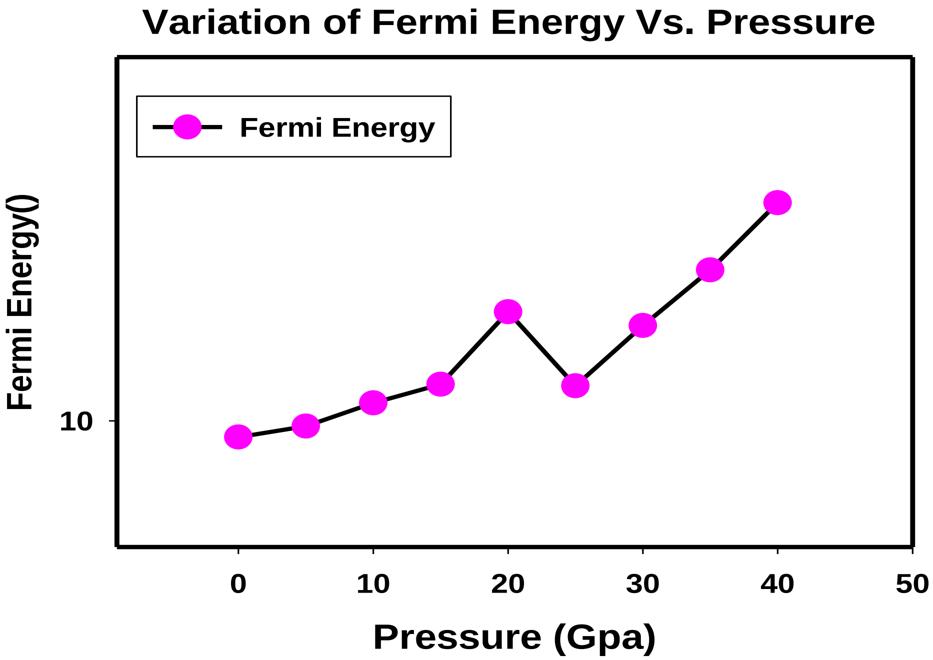

Figure 4.12: Fermi energy as a function of pressure for a strained crystal of $GdBa_2Cu_3O_{7-x}$.

The strain causes instability about the phase transition pressure thus affecting the Fermi energy as observed at ~20GPa. The Fermi energy beyond ~20GPa does not describe a stable crystal structure of the material. The change in energy with pressure can be defined by the expression (Daoud et al., 2012);

$$E_i(P) = E_i(o) + C_iP + C_2P^2 \tag{4.4}$$

4.3.2 Density of State and Partial Density of State

The DOS structure shows a narrow band at -10eV which is dominated by Barium 1s core orbitals, followed with barium 2p core orbital at 5eV. The valence bands near the Fermi energy range (10-20eV) is a result of CuO ion from copper 1d and O 2p orbitals while the conduction band near the Fermi level is dominated by Gd 5p core orbitals which has a greater role in defining superconductivity (Sahu et al., 2011) and as indicated in Figure 4.11 and figure 4.13 respectively.

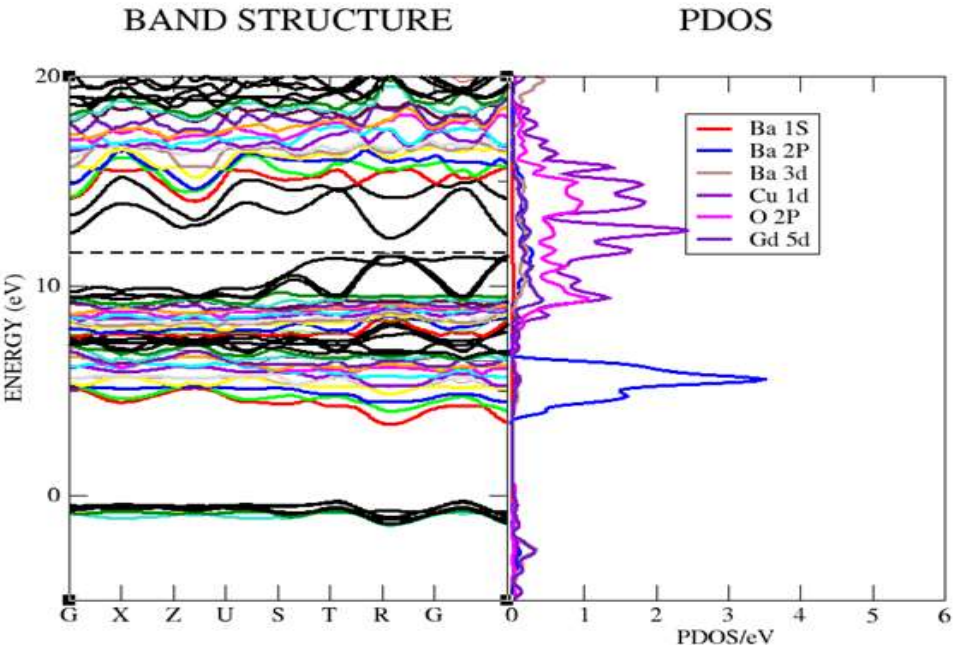

Figure 4.13: The band structure and PDOS at zero pressure.

The partial density of states indicates the elemental and the atomic orbital contribution to the valence and conduction band. The figure indicates the orbitals that are predominant around the Fermi level. The holes that happen to appear in the CuO_2 have a hopping nature which can lead to the destruction of the magnetic properties by the removal of the Cu spin and thus the magnetic bond with other Cu atoms gets broken.

4.4 Elastic Properties

The elastic constant is the basic parameter in the study of how materials respond to stress and from which all other mechanical properties can be calculated. The constant determines the anisotropic and isotropic behavior of a material (Y. Li & Barbič, 2015; Cooper *et al.*, 2015). By application of the non-volume conserving approach, the deformations resulting from the displacement of the primitive cell from their equilibrium position were used to determine the elastic tensor and thus the elastic constant was found (P. Wang *et al.*, 2011);

$$C_{ijkl} = \frac{\partial \sigma_{ij}}{\partial \varepsilon_{kl}} = \frac{1}{V}\frac{\partial^2 E}{\partial \varepsilon_{ij} \partial \varepsilon_{kl}}$$

(4.5)

Where E denotes the Helmholtz free energy, $\partial \sigma_{ij}$ and $\varepsilon_{kl}$are the applied stress and the Eulerian strain tensors respectively.

The orthorhombic crystal for the $GdBa_2Cu_3O_{7-x}$ has nine independent constants: C_{11}, C_{22}, C_{33}, C_{12}, C_{13}, C_{23}, C_{44}, C_{55}, and C_{66} (Long et al., 2013; Mouhat & Coudert, 2014). The constants were used to calculate the elastic modulus, shear modulus, and bulk modulus and are presented as a function of pressure as shown in Figure 4.14.

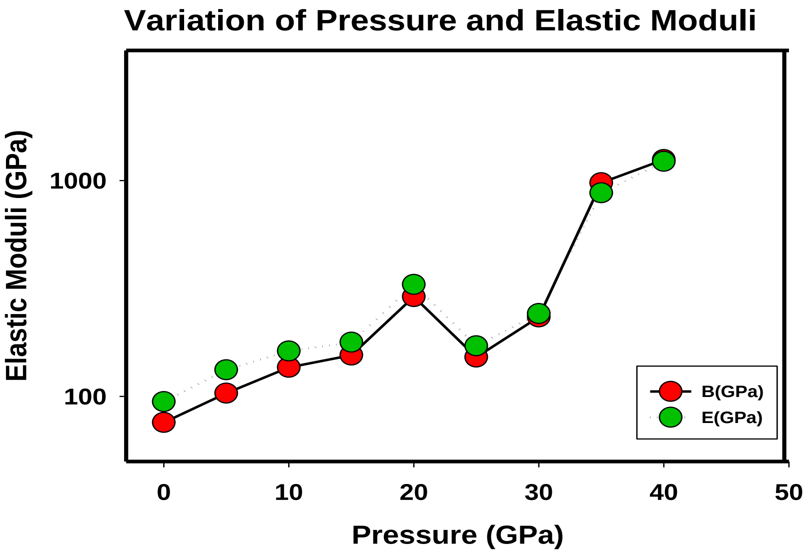

Figure 4.14: Bulk (B) and Young's (E) moduli as a function of pressure.

Young's moduli represents the ratio of volumetric stress and strain whereas bulk moduli represents the ratio of linear stress to strain. The curves in Figure 4.14 imply direct proportionality represented by the equation;

$$3B\left(1-\frac{2}{m}\right)=E. \quad (4.6)$$

The calculated elastic constants C_{ij} shown in Table 4.3 were used to calculate the bulk and shear moduli as a function of pressure shown in Table 4.5. The $C_{ij}(i \neq j)$ determines the strength of a material. The choice of using the $C_{ij}(i \neq j)$ which is calculated using the volume conserving orthorhombic distortion is governed by the fact that the balance in energy per volume matrices cancels out for the three distortions. Because of that reason, $C_{ij}(i \neq j)$ elastic constants are the ones that determine the strength of a material (R. Zhang *et al*., 2015).

Pressure leads to an increase in the elastic constants Table 4.3. The high values of C_{11}, C_{22}, and C_{33} are usually associated with linear compression and the others define the shape of the crystal (Fecht *et al.*, 2008). Since the calculated values of the C_{11}, C_{22}, and C_{33} are higher than the others, it means the crystal can withstand deforming stress along the axial than the other directions which are to withstand along the other non-axial direction. The trend only happens up to ~20GPa.

Table 4.3: Calculated elastic constants C_{ij} $(\boldsymbol{GPa})$ of $GdBa_2Cu_3O_{7-1}$ under the effect of induced pressure up to 25 $(\boldsymbol{GPa})$.

$\boldsymbol{P(GPa)}$	$\boldsymbol{C_{11}}$	$\boldsymbol{C_{22}}$	$\boldsymbol{C_{33}}$	$\boldsymbol{C_{12}}$	$\boldsymbol{C_{13}}$	$\boldsymbol{C_{23}}$	$\boldsymbol{C_{44}}$	$\boldsymbol{C_{55}}$	$\boldsymbol{C_{66}}$
0	125.15	126.73	115.86	80.41	38.22	42.94	39.68	27.84	57.31
5	180.35	207.34	154.64	89.02	51.61	52.67	48.04	34.97	67.39
10	225.16	270.89	217.71	115.12	76.63	217.71	53.19	42.09	76.61
15	256.14	318.62	229.03	132.31	89.83	86.10	57.35	46.87	81.91
20	87.13	312.79	915.02	4.34	2040.02	2158.10	129.25	774.49	288.13
25	246.40	304.85	228.11	130.63	89.04	83.61	54.49	42.96	81.38
30	173.10	607.32	412.77	485.65	388.25	988.85	499.10	19.16	112.05
35	274.24	436.65	324.89	341.67	231.80	451.34	226.12	40.21	105.34
40	397.43	503.93	295.85	196.91	143.65	145.01	71.20	64.07	101.37

For C_{ii} $(i = 1,2,3,4,5,6)$ the elastic constant increases with pressure as opposed to $C_{ij}(i \neq j)$. The strength of bonding along different directions also depends on the magnitude of C_{11}, C_{22}, and C_{33} (L. Sun et al., 2017). The elastic constants C_{11}, C_{22}, and C_{33} are tensile strength along

[100], [010], and [001] directions respectively. It is noted that $C_{11}>C_{22}>C_{33}$ which means the strength of bonding in [100] direction is greater than the others Table 4.3.

The measure of ductility is determined by the difference in magnitude between the bulk modulus and shear modulus (Ravindran et al., 1998; C. Zhang et al., 2020). As indicated in Figure 4.14 and Table 4.5, the difference can be noticed and hence the material is considered brittle but the ductility gets onset with increasing pressure. The computed values of G and B indicate an increase, as the magnitude of pressure increased but the value of B at every pressure was higher. This means that the ratio $\frac{G}{B}$ was less than one (lower) indicating more ductility. The ratio is called Pugh's ratio and is usually used as a criterion for checking brittle and the ductile properties of a Material (Pugh, 2016). The critical value which determines whether a material is brittle or not is 1.75 (Reynaud et al., 2005). From the values in Table 4.3, it can be concluded that pressure increases the ductility of $GdBa_2Cu_3CO_{7-x}$ up to ~5GPa as indicated by the calculated values.

The Young's moduli and bulk moduli are also used to calculate the Poison's ratio which is also a criteria for isotropic material. Inisotropic material should have values ranging from -1 to 0.5 (Mattrup & Ravn, 2019) . The Poisson's ration was calculated by:

$$n=\frac{3G-2B}{2(3G+2B)} \tag{4.7}$$

The calculated values using the equation 4.7 ranged from -0.0616 to 0.3723 which also confirms the anisotropic nature of the material.

The mechanical stability criteria for the orthorhombic phase of $GdBa_2Cu3O_{7-x}$ under zero pressure in the isotropic condition is satisfied by the following condition in equation 4.6 (Long *et al.*,2013; Mouhat & Coudert, 2014).

$$C_{ii} > 0(i = 1,4,5,6) > 0,\ (C_{11} + C_{22} - 2C_{12}) > 0, (C_{11} + C_{33} - 2C_{13}) > 0,$$
$$(C_{22} + C_{33} - 2C_{23}) > 0,,\ (C_{11} + C_{22} + C_{33} + 2C_{12} + 2C_{13} + 2C_{23}) > 0,\ \frac{1}{3}(C_{12} + C_{13} + C_{23}) < B < \frac{1}{3}(C_{11} + C_{22} + C_{33}) \qquad (4.8)$$

The computed values derived from the aforementioned equations demonstrate that when the substance experiences little isotropic distortion, the stability condition is satisfied. The Voigt-Reuses-Hill averages (Man & Huang, 2011; Villalobos-Portillo et al., 2019) were used to convert the anisotropic values of the constants to isotropic and then used to calculate the transverse, longitudinal, and average sound velocities and they were value used to calculate the average sound velocity Table 4.4. The observed increasing trend up to 20 GPa can be attributed to increasing stiffness due to pressure and the decrease after 20 GPa is due to the phase transition from orthorhombic to tetragonal phase.

Table 4.4: The effect of pressure on the longitudinal Bulk velocity $\mathbf{v}-\mathbf{B}(\mathbf{m/s})$, shear velocity (v-G (m/s), and compressional velocity v-E(m/s).

$P(GPa)$	$v-B(m/s)$	$v-E(m/s)$	$v-G(m/s)$
0	4256.82	4256.82	2307.13
5	4256.88	4256.88	4818.10
10	4374.88	4374.88	4256.82
15	3716.58	3716.58	5506.64
20	1852.41	1852.41	24108.5
25	4334.80	4334.80	5434.21
30	6228.24	6228.24	2415.64
35	5157.21	5157.21	2821.65
40	4435.89	4435.89	3686.16

As indicated in the table above, the increased pressure leads to an increase in the wave velocity for this $GdBa_2Cu_3O_{7-x}$.

4.4.1 Elastic Properties at Zero Pressure and High Pressure

The stable crystal structure at zero pressure is shown in Figure 4.3 after full optimization of both the lattice parameters and the atomic position. The values, a, b and c for different amounts of induced-pressure that were applied in the calculation of the elastic constant are shown in the Table 4.3. At zero pressure they agree well with the ones experimental value reported in (Ingosi, 2018). The elastic criteria for stability for an orthorhombic material equation 4.6 are also satisfied for the calculated pressure up to 20GPa. The bulk modulus (B) tells how the volume gets deformed due to changes in bond length while the shear modulus (G) tells how the bond angle will change on application of strain. Under the criteria of deformation, there are factors that determine the degree of deformation. The two factors B and G (Table 4.5) when applied to calculate the bond angles indicate a drastic drop in bond angle with increasing pressure. This is followed by a very small variation as pressure continues to rise and the same trend is observed in Figure 4.15.

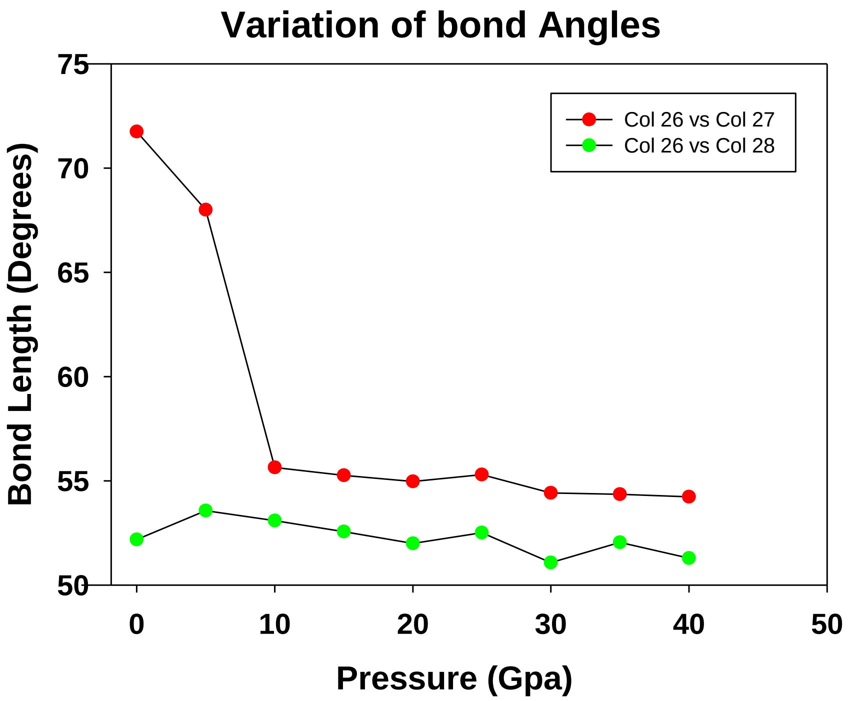

Figure 4.15: Change of bond length as a function of pressure.

It is noted that there is change in large percentage decreased in the -O-Cu-O- bonding up to 10Gpa.

Table 4.5: The calculated bulk modulus (**B**), shear modulus (**G**), Young's modulus (**G**), for $GdBa_2Cu_3O_{7-x}$.

$P(GPa)$	$B(GPa)$	$E(GPa)$	$G(GPa)$
0	75.72	94.46	36.56
5	103.39	132.69	51.76
10	136.21	162.20	63.17
15	155.21	178.04	68.17
20	289.51	330.17	150.64
25	151.86	171.32	652.96
30	233.08	241.56	241.56
35	976.34	876.21	197.32
40	1249.7	1226.43	368.62

The values were calculated from the constant C_{ij} (Chen et al., 2019). Table 4.6 present a tabulation of values of bond angle as a function of pressure. This means that the elastic moduli drops up to around 10GPa and then remains fairly constant for -O-Cu-O- bond. The difference in the bond angles indicates that this material is anisotropic in nature a factor that influences the determination of superconductivity of the material as discussed in chapter three, under the properties of superconductors. The vlues for the bulk modulus (**B**), shear modulus (**E**) and Young's modulus (**G**) for $GdBa_2Cu_3O_{7-x}$ were calculated from the constant Cij (Chen et al., 2019). For all the calculated moduli there is an increase in the magnitude of the calculated values with increasing values of pressure up to 20GPa (optimally doped) then followed inconsnstent values in the over doping regime which represent the unstable tetragonal phase of the structure.

Table 4.6: Variation of bond angles with pressure. The $\boldsymbol{\theta_1}$ and $\boldsymbol{\theta_2}$ represent -O-Cu-O- and -Cu-Ba-Cu- bond angles respectively.

$\boldsymbol{P(GPa)}$	$\boldsymbol{\theta_1}$	$\boldsymbol{\theta_2}$
0	71.75	52.18
5	68.00	53.57
10	55.64	53.09
15	55.26	52.56
20	54.97	52.00
25	55.30	52.51
30	54.42	51.08
35	54.35	52.05
40	54.23	51.29

The change in bond angle can be attributed to changes that occur within the inter atomic spacing of the material that lead to changes in the shear modulus of the material. Because the bond angle of -O-Cu-O- is a weak angle, it undergoes more change in bond length than other angles.

4.4.2 Elastic Anisotropy

Elastic anisotropy factors give the directional dependency of the elastic properties. The directional dependence of the elastic properties find application in so many areas of interest (Nam et al., 2020; Vatandoost et al., 2020). Some of these include; response of external stress of a crystal, the charges flow on a crystal and mapping of the geophysical fields during the exploration. The difference in elastic behavior of the crystal in different directions can be attributed to the nature of bonding and atomic orientation. The anisotropic factors considered for orthorhombic crystal structure are; A(100) crystallographic factor for $< 011 >$ and $<$

$010 >$ shear planes, A(010) cryptographic factor for $< 001 >$ and $< 001 >$ shear planes and A(001) crystallographic factor for $< 110 >$ and $< 100 >$ shear planes. A crystal is considered to be elastic anisotropic if the value of A(100), A(010) and A(001) are less or greater than one. If the value is a unity the crystal is considered to be elastic isotropic. The criteria for anisotropic factors given by the following expressions:

$$A(100) = \frac{4(C_{44})}{C_{11}+C_{33}-2C_{13}}$$

(4.9)

$$A(010) = \frac{4(C_{55})}{C_{22}+C_{33}-2C_{23}}$$

(4.10)

$$A(001) = \frac{4(C_{66})}{C_{11}+C_{22}-2C_{12}}$$

(4.11)

The values of the calculated shear anisotropic factors are presented in Table 4.7 with increasing pressure up to 40 GPa. It is observed that from all planes the material is less anisotropic. The shear anisotropy factors A(100), A(010), and A(001) must be unity for a crystal to be considered isotropic, while any other values smaller or greater than one measures the degree of elastic anisotropy. All the calculated values of various anisotropy factors under pressure up to 40GPa for $GdBa_2Cu_3O_{7-x}$ are plotted in Figure.

Table 4.7: The variation of the shear anisotropic factors with pressure under different planes.

$P(GPa)$	$A(100)$	A(010)	$A(001)$
0	0.964453	0.710612	2.517461
5	0.829098	0.54504	1.285762
10	0.734643	3.165852	1.152854
15	0.750876	0.499347	1.056426
20	0.105340	0.629868	2.945813
25	0.735280	0.469842	1.122521
30	0.472600	0.080030	2.34807
35	0.524200	0.342100	1.342700
40	0.701512	0.502746	0.798912

When the applied pressure increased from 0–40 GPa, A(100) in the range of the factors of 0.9642 to 0.1053 for the pressure range of 0GPa to 20GPa. This means that for this plane pressure highly increases the anisotropy of the material but both A(100) and A(010) had little variation with increasing pressure. A(001) firstly decreased from showing an increase up to the pressure of 20GPa and then decreased from 1.016 to 0.758 after 30 GPa, implying that the anisotropy of the A(001) shear plane between the <110> and <010> directions firstly decreased and then increased with pressure. However, pressure had little influence on the shear anisotropy of the A(100) plane between the <011> and <010> directions, as well as the A(010) plane between the <101> and <001> directions. Crystal elastic anisotropy can also be assessed using the percentage of anisotropy in the compressibility A_B and the shear moduli A_G. These are calculated using the equation (Katz & Meunier, 1987):

$$A_B = \frac{B_V - B}{B_V - B} \qquad (4.12)$$

$$A_G = \frac{G_V - G_R}{G_V - G_R}$$

(4.13)

A_G and A_B take values of zero to one. The value of zero means that the crystal is elastic isotropic while the value of one means the crystal has the highly anisotropic. The values of A_B and $A_G$with varied pressure are presented in Table 4.8. The values of the factors are highest at 5GPa. The inconcistances experienced beyond 20GPa are as a result of the unstable tetragonal phase of the material.

The shear velocity only characterizes solid material while the compression wave can also characterize the fluids. The shear sound velocity is determined by the shear modulus of the material and is not constant in motion. The velocity of the longitudinal is as a result of the magnitude of the materials shear modulus, the change in volume due to compression and the density of the material. The bulk velocity is as a result of the combination of the two velocities and is presented by the formula;

$$cB_v = \left(cv_l^2 - \frac{4}{3}v_s^2\right)^2$$

(4.14)

Table 4.8: Values of percentage of anisotropy in the compressibility A_B and the shear moduli A_G. The highest values for both are recorded at 5GPa.

$P(GPa)$	A_B	A_G
0	0.013744	0.054422
5	0.664961	0.32819
10	0.019874	0.030536
15	0.016735	0.031966
20	0.015210	0.03342
25	0.014053	0.035574
30	0.014053	0.039821
40	0.391520	4.53753

The trend in the Table 4.9 can be explained on the basis of wave scattering theory in which pressure is assumed to reduce the porosity of the crystal thus leading to high sound velocity. High sound velocity in a crystal increases with increase in the elastic moduli (Fan et al., 2019; Liu et al., 2009). This effect on the ceramic perovskite is aided by the interatomic forces that are associated with the high temperature superconductors. In this superconductor the reduction in the volume due to pressure can be attributed to the increase of the copper valence due to the hoping oxygen. The increase of the copper valence leads to decreased ionic radius of the copper ions hence the crystal hardens by reduction of volume which favors the sound velocity.

The anisotropic factor is determined by bonding along a given plane between nearest atoms is strong (Bouhadda et al., 2013). For this case, it means that there is strong bonding of atoms in the <001> shear plane.

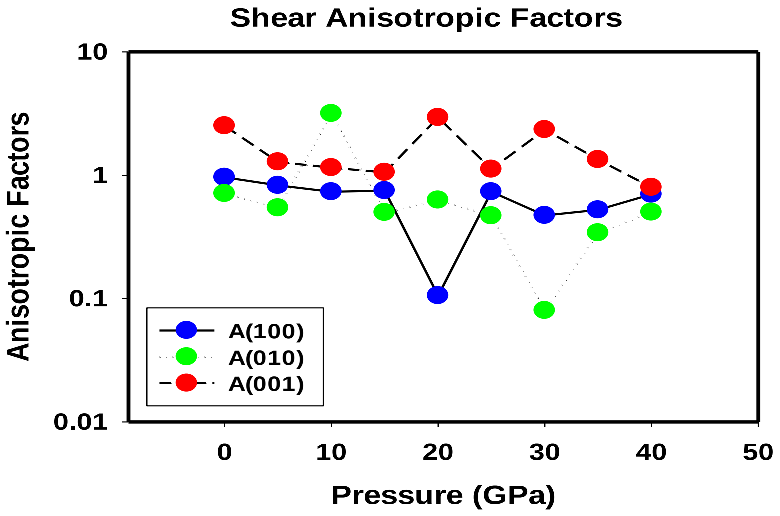

Figure 4.16: The shear anisotropic factor as a function of pressure the $GdBa_2Cu_3O_{7-x}$.

Table 9: A table of shear anisotropic factors with varied pressure up to 40GPa.

$P(GPa)$	$A(100)$	A(010)	$A(001)$
0	0.964453	0.710612	2.517461
5	0.829098	0.545040	1.285762
10	0.734643	3.165852	1.152854
15	0.750876	0.499347	1.056426
20	0.105340	0.629868	2.945813
25	0.735280	0.469842	1.122521
30	0.472600	0.080030	2.348070
35	0.524200	0.342100	1.342700
40	0.701512	0.502746	0.798910

For this superconductor the non-porous regime gives good relationship between the elastic moduli and the hydrostatic pressure (Dodd et al., 2003; Mech et al., 1989). The increased non porosity which hardens the crystal with increased pressure is related by the equation;

$$E = E_0(1 - 1.9P + P^2)$$

(4.15)

In which E represents the elastic moduli and E_0 represents the elastic moduli of the crystal with reduced porosity and P is the fractional change in volume. The the relationship between the elastic modulus at zero pressure (B_0) and that at elevated pressure $B(P)$ is given by the relationship;

$$B(P) = B_0 + \frac{\partial B}{\partial P} P$$

(4.16)

The result obtained at zero pressure is in good agreement with the experimental result reported of 84.6 GPa for bulk modulus at zero pressure (Almond et al., 1989).

The study of the sound velocity and associated attenuation is key in the different application of superconductors. This is attributed by the fact that most superconductors undergo polymorphic structural phase transition as presented in Figures 4.17. For Gd $Ba_2Cu_3O_{7-x}$, changes in the elastic moduli sound velocity is in most cases can be an indicator of phase transition and this affects the superconducting transition temperature. This can be seen in Table 4.8 in which there is an abrupt change in elastic moduli sound velocity near the structural phase transition and in Figure 4.16. The relationship for this transition and the elastic moduli can be presented as.

$$B_n - B_s = \frac{B_n^2}{4\pi} \left(\frac{\partial H_c}{\partial P} \right)^2$$

(4.17)

Where B_n and B_s are the normal bulk moduli the normal and the superconducting phases respectively, H_c is the thermodynamic critical field and P is the pressure. As indicated, the elastic moduli in the superconducting phase which is below ~21.9GPa is lower the non-superconducting tetragonal phase. The equation 4.15 applies for all the moduli of elasticity.

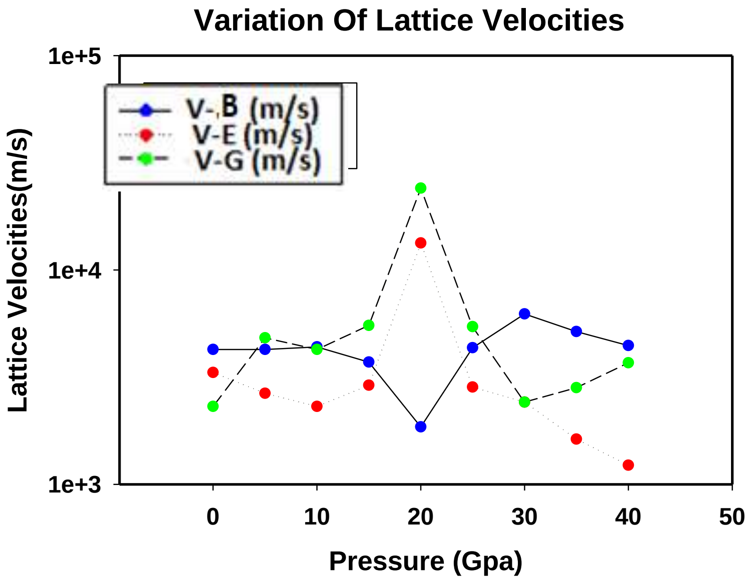

Figure 4.17: Lattice velocities as a function of pressure for the $GdBa_2Cu_3O_{7-x}$.

The lattice velocities in the Figure 4.17 indicate a drastic change at ~20GPa implying polymorphic phase transition for the structure at that induced pressure.

4.4.3 Cauchy Pressure

The Cauchy pressure gives a better description of the interatomic bonding that defines the characteristic of a material resulting from the nature of bonding at atomic level. For an orthorhombic structure $C_{12} - C_{66} > 0$, $C_{13} - C_{55} > 0$ and $C_{23} - C_{44} > 0$ implies the atomic bonding is metallic in nature while $C_{12} - C_{66} < 0$, $C_{13} - C_{55} < 0$ and $C_{23} - C_{44} < 0$ are majorly associated with the directional properties. For the large absolute values, the crystal is assumed to have strong metallic bonding and directional properties. The calculated values of the Cauchy pressure show that the maximum values of absolute Cauchy pressure are observed at a pressure of 20GPa Figure 4.18. This indicates the strongest bonding is of the metallic kind. The increasing values of the Cauchy pressure with pressure means increased metallization with increased pressure. The inconsistencies in the values of the Cauchy pressure after the maximum values indicates instability if the bonding and this can be attributed to the phase transition phenomenon which occurs slightly above ~20GPa.

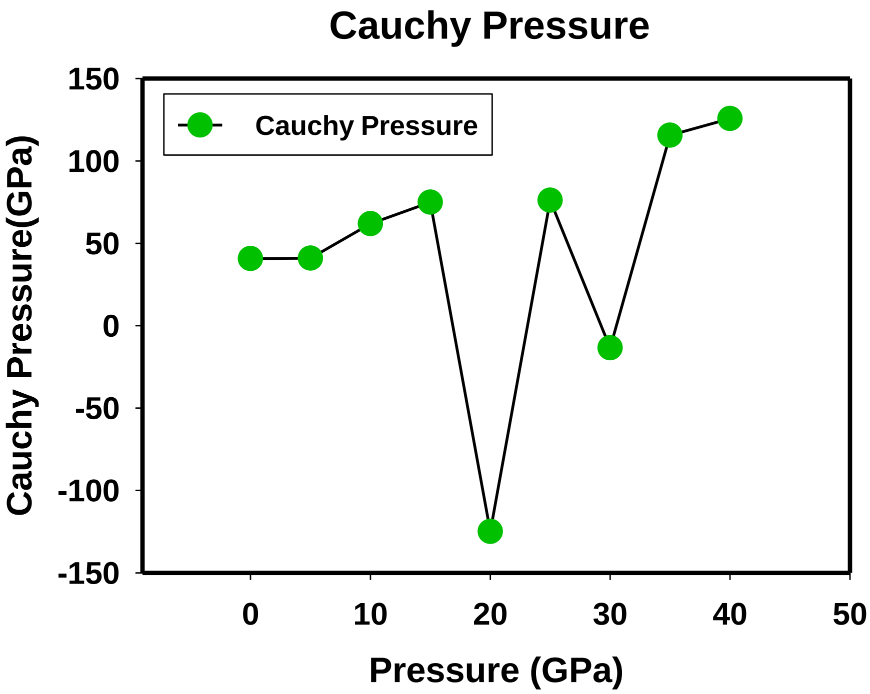

Figure 4.18: Cauchy pressure as a function of pressure..

The positive Cauchy pressure signifies ductility of a structure while the negative value signifies the brittleness of the structure. Since at low pressure the material has a positive value, then it means the criteria can not be relied on for the assessment of the ability of the material to resist fracture as explained in chapter two.

4.4.4 Hardness of a Material

The strength of a material can be considered in terms of hardness and the yield strength. Hardness is an intrinsic behavior that tells how a material will resist deformation from the applied force. Yield strength tells the ability of a material to resist plastic deformation. The hardness of the crystal in the study was calculated using the Vickers hardness model which is expressed as;

$$H_v = 2(k^2G)^{0.585} - 3$$

(4.18)

Where $k = \frac{G}{B}$, G is a shear modulus and H_v vicker hardness of the material. The yield strength is expressed as $\sigma_y = \frac{H_v}{3}$. Both the values of the Vicker hardness and the Yield strength increases up the value of 15GPa and then decrease drastically Figure (4.19). This means that ability of this material to resist deformation at low pressure and elevated pressure is low as compared to the pressure of 15GPa. Maximum hardness is experienced at the pressure of 15GPa. Materials which have high yield strength in most cases are likely to be brittle and from Figure 4.19 it can be confirmed at the optimal pressure for the two properties are high for the $GdBa_2Cu_3O_{7-1}$ perovskite material. This means that in straining the material to the optimum level of yield strength, the material deforms in a brittle manner. When compared with other ceramic materials it is observed that the values reported in this study are high and hence the ability of this material to resist dislocation on the application of stress is confirmed.

The hardness of a crystal relates to how bonds hold the atoms and the degree of hardness when pressure is applied depends on the ability of the material to resist disorientation of the atoms from their bonded positions. The $GdBa_2Cu_3O_{7-x}$ which is a ceramic material is characterized by covalent bonds which form the intrinsic perspective of the crystal structure and are directional. The tendency of the bonds to be directionally rigid prevents dislocation from having a smooth slide because it will involve a lot of distortions. The observed hardness at that relatively higher pressure of 15GPa can thus be associated with the inability to move the dislocations in the crystal lattice.

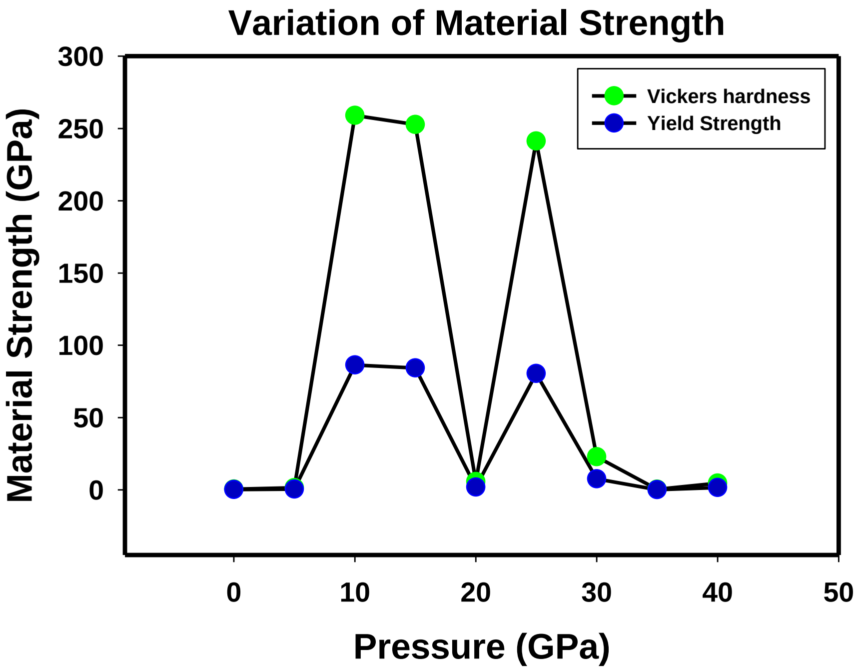

Figure 4.19: Material strength as a function of pressure for the $GdBa_2Cu_3O_{7-x}$.

The low value of the yield strength implies that the material can undergo plastic deformation with small applied stress which confirms the ductile nature of the material. On the other hand the high value of Vickers hardness confirm that if a thin piece of the material is subjected to stress, it can withstand to high magnitude of pressure. At phase transition the values take minimum value.

4.4.5 Pugh's Criterion

The criterion is used to assess whether the material is ductile or brittle. According to the criterion, a material is considered brittle if Pugh's ratio is less than 1.75 and ductile if Pugh's ratio is greater than 1.75. The calculated values indicate that at low pressure the material portrays a relatively high level of ductility as inferred from the values in Figure 4.20. This can be explained in terms of reduction of the stress arising from low pressure since at low pressure the stress is usually low.

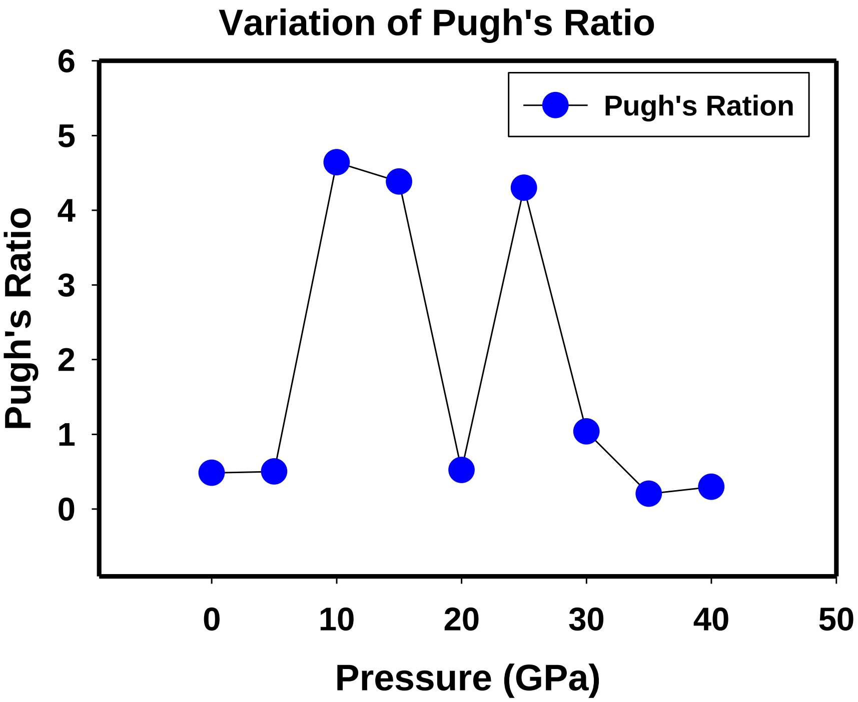

Figure 4.20: Pugh's ratio as a function of pressure for the $GdBa_2Cu_3O_{7-x}$.

The Figure 4.20 indicates that the ratio which is a coefficient of the bulk and shear modulus illustrates the pressure dependence of the material to plastic deformation. Ductile behavior is observed in the material at low pressure ~5GPa. With increased pressure the material become brittle with the Pugh's ratio greater than 1.75.

4.4.6 Energy Factor K

The energy factor K can be used to estimate the plasticity of a crystalline material in relation to dislocation under stress. The dislocation in a crystalline material can occur in two ways: edge dislocation and screw dislocation. In the edge dislocation an extra half plane of atoms is shifted at the middle of the crystal and as a result it disorients the nearby planes of atoms. Screw dislocation is usually produced by tearing the crystal along a plane that is parallel to the slip direction. Plastic deformation on the crystalline structure is aided by the degree of crystal dislocations. These dislocations which appear in a crystalline structure as distortions interfere with the atomic arrangement and introduce stress in the system. The calculated result indicates an increase of the factor up to ~90 at 15GPa for K-screw and ~60 at 20GPa for K-edge Figure 4.21. This is true as the literature value relates the two by the expression $\mathrm{E}_{\mathrm{screw}} = 0.66\mathrm{E}_{\mathrm{edge}}$. The energy of dislocation is as a result of the elastic component of the strained bonds within an elastic material. This elastic component of energy depends on the crystal size.

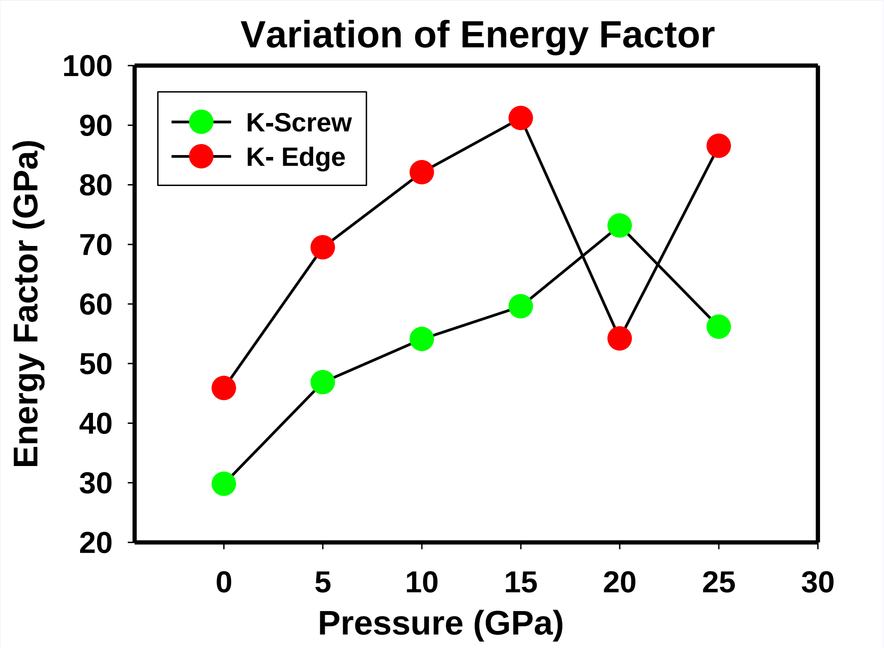

Figure 4.21: Energy factor as a function of pressure for $GdBa_2Cu_3O_{7-x}$.

4.4.7 Debye Temperature

Debye temperature is a thermodynamic quantity in material science that is associated with the phonon vibrational modes in a crystal, elastic constant and specific heat. For isotropic elastic medium it is given by (Ledbetter et al., 1987):

$$\Theta_D = \frac{h}{k}\left[\frac{3n}{4\pi}\frac{N_A\rho}{M}\right]^{\frac{-1}{3}} v_m$$

(4.19)

Where v_m, n is the charge density, v_m is the average sound velocity, h is the Plank's constant, N_A is the Avogadro's number, k is the Boltzmann's constant, ρ is the density and M is the molecular weight of the solid material. The calculated values of the Debye temperature at different pressure are shown (Table 4.10). The calculated Debye values are used to calculate the superconducting transition temperature using equation 4.17. The average sound velocity is expressed as:

$$v_m = \frac{1}{3}\left[\frac{2}{v_t^3} + \frac{1}{v_l^3}\right]^{\frac{-1}{3}}$$

(4.20)

Where v_l and v_t are the longitudinal and transverse sound velocities and are calculated from the Bulk modulus B and the shear modulus G (Luan et al., 2018).

The Debye temperature increased from 409.00K to 850K as pressure increased from 0GPa to 20GPa. This increase is because of the phase transition to non- superconducting tetragonal phase of the material. The high value of the Debye temperature means that phonon coupling constant is strong. From Table 4.10, it is also noted that Fermi energy increases with increase in Debye energy. The electron density at the Fermi level is given by:

$$n_e = N_e e^{\frac{E_F - E_g}{k}}$$

(4.21)

The equation implies that increase of the electron density mean an increase in the Fermi energy and that leads to an increase of the Debye temperature. The equation 4.20 above is related to the definition of Debye temperature in equation 4.16.

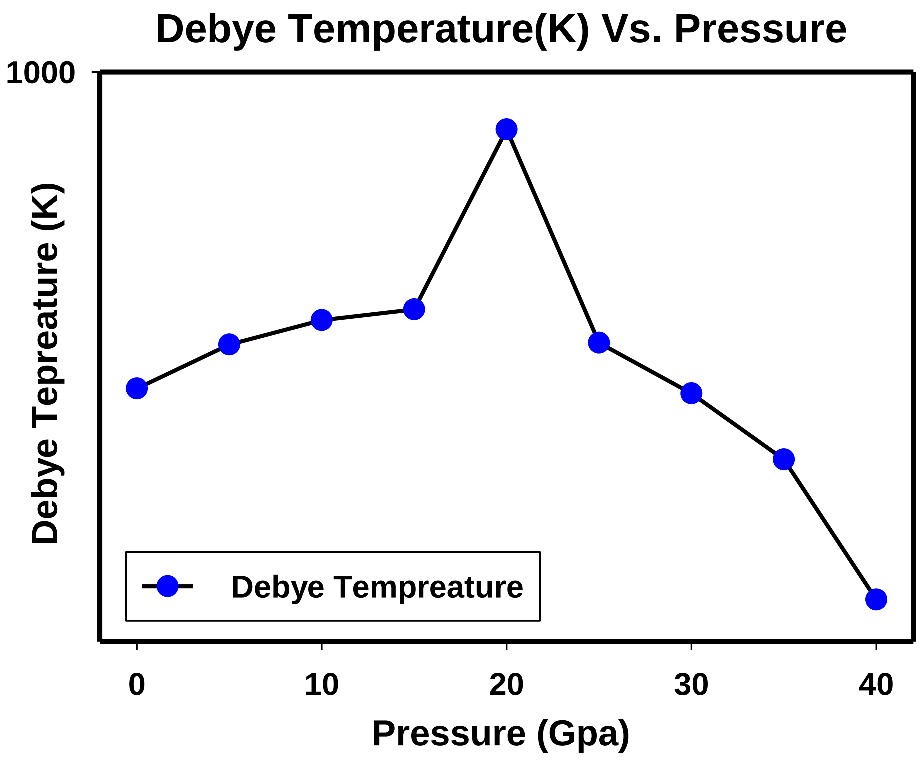

Figure 4:22: Debye temperature as a function pressure. The maximum Debye temperature is achieved at ~20GPa.

4.4.8 Superconductivity Transition Temperature Under Pressure

Cuprate superconductors undergo doping on the condition that holes must be populated in the CuO_2 layers as suggested by the BCS theory and the Mc Millan's equation. like other cuprates $GdBa_2Cu_3O_{7-x}$, the hole concentration can be varied by reducing the oxygen concentraton represented by x in the formular or by inducing pressure on the crystal structure. The effect of external pressure to the crystal is that it varies the concentration of charges near the Fermi level of the crystal lattice which leads to modification of the electronic structure of the crystal. In this cuprates superconductivity is brought about by two factors namely; doping effect and polar ionic. The combination of the two effects enhences the population of the hoping oxygen between the upper and lower layer of the crystal and thus results to increased superconductivity and hence the superconductivity transition temperature T_C. The Table 4.10 represents the superconductivity transtion temperature resulting from pressure induced doping. It is observerved that the underdoping legime leads to increase in superconductivity transtion temperature while the overdoping legime leads to decrease in the superconductivity transtion temperature. As explained by the BCS theory, the tanstion from normal state to the state of superconderctivity is attributed to an interaction between the charge carrier, electrons and holes. For the cuprate high temperature superconductor it is the holes that contribute to the superconductivity. The pairing of the charge carriers leads to the smooth flow that results in the superconducting ground state. The temperature dependence conductivity is brought about by the crystal lattice vibration modes under normal state. Above the superconductivity transition temperature enhanced electron-phonon interaction leads to high electrical resistivity but strong pairing occurs at or below the superconductivity transition temperature.

The holes then happen to appear in the CuO_2 have the hopping nature which can lead to destruction of the magnetic properties by the removal of the Cu spin and thus the magnetic bond with other Cu atoms get broken. Upon doping the superconductivity state emerge for the destroyed antiferromagnetic state which favor superconductivity. The study adopted the electron phonon coupling constant of $\lambda = 3.9$ (Philip B Allen, 2000).

Table 4.10: The table represents values for the calculated Fermi energy (E_F), Debye Temperature (Θ_D), Average sound velocity (V_m) and the superconductivity transition temperature (T_C) for $GdBa_2Cu_3O_{7-x}$.

$P(GPa)$	E_F	$\Theta_D(K)$	$v_m(M/s$	$T_c(K)$
0	9.55	409.00	2551.76	67.92
5	9.85	463.11	2939.09	77.08
10	10.52	495.99	3129.50	82.20
15	11.09	511.42	3213.91	84.86
20	13.62	850.39	6375.56	141.16
25	11.04	465.44	3496.60	83.59
30	13.10	403.35	3154.52	77.47
35	15.33	334.54	2451.43	60.32
40	18.54	225.10	1579.71	54.33

The values for the Table 4.10 were calculated from the moduli in table 4.2. Under doping starts at $\mathbf{T_C}$=67.92K.

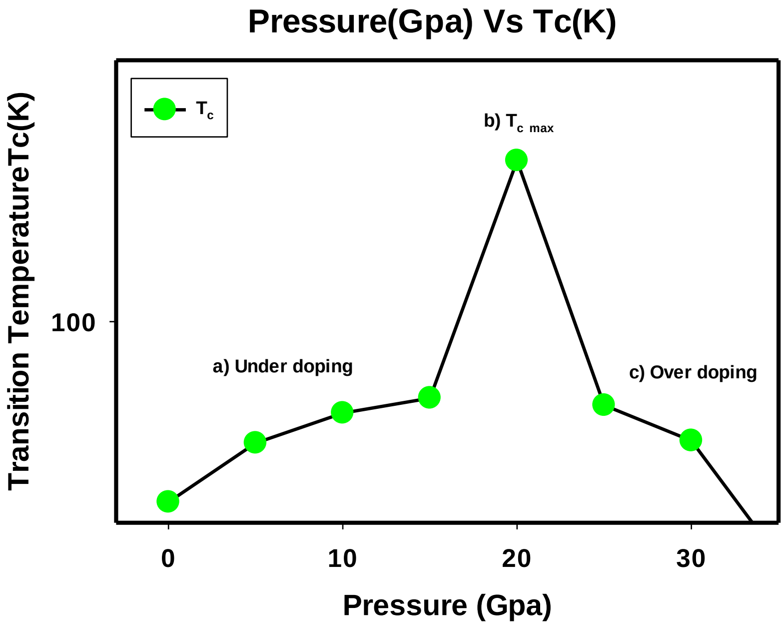

Figure 4.23: The graph represents plot of TC against pressure.

The plot in Figure 4.23 indicates how hole doping for the $GdBa_2Cu_3O_{7-x}$ varies with pressure. It is shown that T_C indicates a gradual rise at $n > n_{min}$ in the under doping regime and achieves a maximum at $n = n_{op}$ which represents the T_C (max) for the crystal under the influence of pressure. At T_C (max) the material is optimally doped. At $n > n_{max}$ the T_C decreases and this described by over doping regime.

The relationship between the hole population as a result of induced pressure and the normal to superconducting state for all the cuprates superconductors including $GdBa_2Cu_3O_{7-x}$ are described by the inverted parabola equation 4.21 (Wejgaard, 1969):

3.4 $$\boldsymbol{T_C = T_C(\mathrm{max})\left[1 - B\left(n_{op} - n\right)^2\right]} \qquad \textbf{(4.22)}$$

Where n_{op} is the crystal's hole concentration in which the T_C attains its maximum value $T_C(\mathrm{max})$ (Figure 4.23). The constant $B = \left(n_{op} - n_{min}\right)^{-2}$, where n_{min} is the minimum hole concentration which marks the onset of superconductivity. Equation 4.22 can be modified to include condtions of superconderctivity transition temperature under pressure as (Wejgaard, 1969);

$$T_C(P) = T_C(\mathrm{max})(P)\left[1 - B\left(n_{op} - n(P)\right)^2\right]$$

(4.23)

Where $T_C(P)$, $T_C(\mathrm{max})(P)$ and $n(P)$ are calculated at a given pressure (P). The model works on the assumption that n_{op} and B do not depend on pressure. Assuming $T_{C(op)}(P)$ to be pressure dependent T_C when the crystal has maximum hole concentration then equation 4.22 can be written as:

$$T_C(P) = \frac{T_{C(op)}(P)\left[1-B\left(n_{op}-n(P)\right)^2\right]}{\left[1-B\left(n_{op}-n_{op}(P)\right)^2\right]}$$

(4.24)

Equation 4.23 is a representation of the superconductivity transition tempetrature when the induced pressure is within the underdoping regime. With increasing pressure n(P) shift towards n_{op} leading to optimal doping with the T_C taking a mximum value. In this work the induced pressure that resulted to maximum T_C was approximated to be at 20GPa (Table 10). The increase of T_C (Table 4.10) resulting from induced pressure up maximaun T_C can be explained in terms of the population of charge carriers in the CuO_2 Planes of $GdBa_2Cu_3O_{7-}$ which is a common characteristic for all cuprate superconductors (Ambrosch-Draxl et al., 2004). Therefore it means that the oxygen located at the center of the cuprate moves to CuO_2 under the influence of the induced pressure and the superconductivity transition temperature is associated with the minimum buckling angle of CuO_2. The over doping limit indicated in Table 4.10 is a result of population of charge carriers near the Fermi level and the over doping limit is marked by maximum Fermi energy. The the computed values of T_C show that the material's superconductivity properties vary with pressure but good high temperature superconducvity is achieved at a pressure of approximately 20GPa. The good superconductivity behavior is also supported by the computed high values for the Debye temperature (Cocisnunications, 1980). When a material potrays better T_C , it implies that the material is stable (Barns & Laudise, 1987; Klose & Hertel, 1970) and this is illustrated in the stability criterion (equation 4.7) from the elastic constant. Above 25GPa tha material shifts to unstable superconducting phase (tetragonal phase) and that can explain the inconsistence observed of T_C observed above that value.

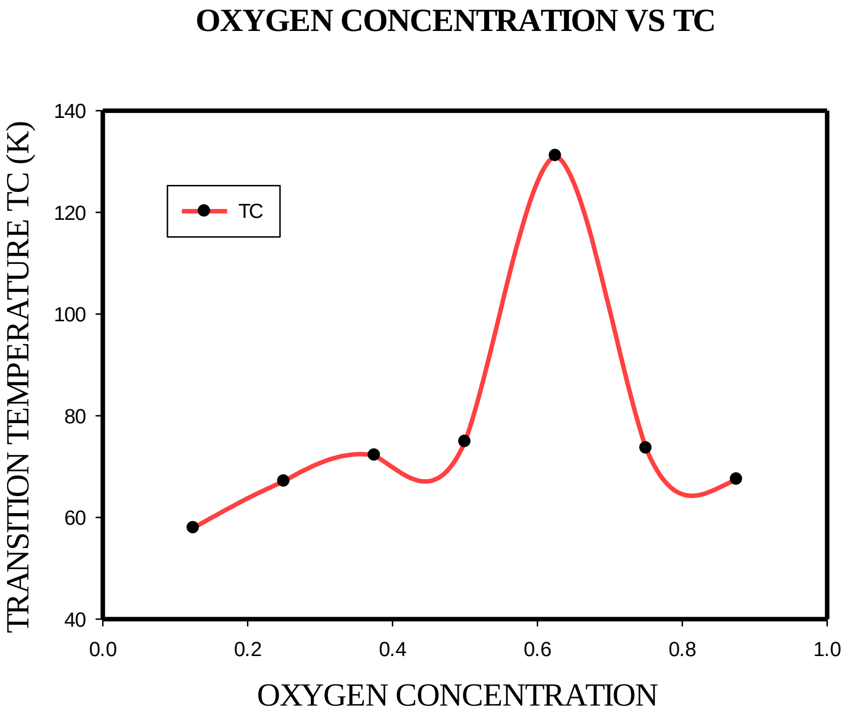

Figure 4. 24: A graph of hole concentration for the $GdBa_2Cu_3O_{7-x}$ as a function of T_C by varying the value of x by means of super cell.

The Figure 4.24 indicates a rise in T_C which starts at $n > n_{min}$ in the reagion when the material is under doped and a peak is achieved at $n = n_{op}$ which represents the T_C (max) for the material under optimal value x. At T_C (max) the material is optimally doped. Beyond $n > n_{op}$ the T_C drops to minimum and the T_C is described by over doping regime. The behavior of this kind of doping is similar to the of the hole doping under pressure Figure (4.23). The T_C (max) is approximately at $x = 0.65$. the hole doping by variation of x can be explained in terms of hole pairing as the value increases to optimum level. Further increase results to unpairing thus reducing the superconductivity transition temperature.

CHAPTER FIVE

CONCLUSION AND RECOMMENDATIONS

In this chapter we present the summary of the study of this work along with the recommendations for future work to be done. The structural, electronic structure, elastic properties and superconductivity for the layered $GdBa_2Cu_3O_{7-x}$ perovskite material have been studied based on their potential application in many field.

5.1 Conclusion

So far the cuprate superconductors remain to be the ones that exhibit high temperature superconductivity as compared to other superconducting materials. The ability to undertake them through chemical substitution and other forms of doping (hole and electron) makes them even more better for application. The uniqueness of these superconductors lies on the presence of the CuO_2 plane which takes responsibility in giving the material the superconductivity behavior. The influence of the CuO_2 plane is based on the interaction of the 4s-3d orbitals which is as a result of their pairing of localized ions in the copper ion. For maximum hybridization to be realized in the s-d orbitals the conduction band has to be hybridized with the oxygen 2p orbitals. By considering the electronic configuration of elements, the three levels namely; 3d, 4s, 2p are close to each other. Furthermore by considering the 4s orbital for the cuprates it so much correlates to the superconductivity transition temperature. This is strongly related to the partial density of state PDOS results report in this work.

In order to understand the structural stability of the material, structural optimization was carried out with respect to the all lattice parameters and the atomic positions using the plane wave self-consistence field calculations (PWSCF). As indicated in chapter IV, the lattice parameters and the atonic position show that the $GdBa_2Cu_3O_{7-x}$ has a orthorhombic symmetry with space group Pmmm. The stability was verified using the Goldschmidt tolerance factor (f_t) the indicated values in chapter IV show that the material is stable at ground state. Even though the calculated value nears unity indicating stability, by application of pressure the orthorhombic symmetry loses stability and undergoes a polymorphic phase transition to the tetragonal phases at the indicated transition pressure.

In order to study the ground state properties of the material, the molecular volume was varied and the calculated energies plotted with the Birch–Murnaghan equation of state The obtained equilibrium lattice parameters, the bulk modulus (B_o) and pressure derivative of bulk modulus (B') are computed from the calculated ground state energies. The calculated lattice parameters for the material are in good agreement with the experimental results.

The phase transition pressure and metallization with increase in pressure is illustrated. The material undergoes polymorphic phase transition under the influence of pressure to change from orthorhombic to tetragonal phases.

The plotted band structure from the bands calculation indicates the material has a direct band gap at the T high symmetry point of the brillouin sampling. The calculated band gap in good agreement with the available experimental data but slightly underestimated. The underestimation can be attributed to the use of the local density approximation (LDA) and the generalized gradient approximation (GGA) functional pseudopotentials which are known to underestimate the computed band gap. For better understanding of the electronic band structure of the material, further, the total density of states (DOS) was also computed. The partial density of state (PDO) calculation for this material indicates that the conduction band is dominated by the Gd 5p while the valence band near the Fermi level is dominated by the CuO from the Cu 1d and O 2p.

The elastic constant properties of the $GdBa_2Cu_3O_{7-x}$ for the orthorhombic phase were studied by the use of density functional theory (DFT) computational method. A whole set of elastic constants for the material was solved from the quadratic relation between the crystal strain and energy. The local density approximation (LDA) and the generalized gradient approximation (GGA) exchange gave exchange correlation functional gave a close results to the experimental results. By application of the Voigt-Reuss-Hill approximation, the elastic moduli of the material such as the Young, bulk and shear modulus were calculated based on the obtained elastic constant of the material. In comparison with the experimental result the computational methods work better especially when the application is on a single crystal structure at high pressure.

The elastic anisotropy which is a factor associated which superconductivity is illustrated by the anisotropic factors for the orthorhombic crystal material. The anisotropic factors were found to vary with pressure with the highest factors recorded at the pressure of zero. The variation of the factor away from one with increased pressure indicated that anisotropy increased with increase in pressure. From such result it can be inferred that the superconductivity increased with pressure which conforms to the theory. This is also supported with the results of the shear anisotropic factors in different planes which indicate a drop on the factors for the pressure range of 1GPa to 20Gpa. The material hardness test show that the material is relatively ductile at lower pressure and tends to brittleness with increased pressure.

Superconductivity transition temperature was successfully measured by pressure doping. The use of the Mc Millan's formula that requires the application of the Debye temperature calculated from the elastic constants was used to calculate the under doped, over doped and optimally doped superconductivity transition temperature. The material was optimally doped at around 20GPa. The obtained results confirm the ability of pressure to induce doping and hence enhance superconductivity transition temperature up to optimum doping level. The optimal superconductivity transition temperature is found to be above the normal transition temperature.

5.2 Recommendation

More emphasis in this work has been given to the superconducting properties of the $GdBa_2Cu_3O_{7-x}$ perovskite material for application. We are recommending the study of other properties of interest such as the magnetic and optical properties in the influence of the superconderctivity transition temperature. This should include $MBa_2Cu_3O_{7-x}$ (M=other rare earth metal) where the various rare earth metal are likely to give varied properties. We also recommend an intense study of the unstable tetragonal phase which is a polymorph $GdBa_2Cu_3O_{7-1}$ of this material with the intention of finding possible ways that will improve its properties for application under different conditions. The is very important because it as been seen by changing the structure of a material under different condition it can result to new and improved properties which are essential for both industrial and other applications.

Experimental studies on the suggested areas should also be considered as a way of supplementing the results obtained from the computational studies.

REFERENCES

Abrahamsen, A. B., Magnusson, N., Jensen, B. B., & Runde, M. (2012). Large superconducting wind Turbine generators. *Energy Procedia*, *24*(January), 60–67. https://doi.org/10.1016/j.egypro.2012.06.087

Abrikosov, A. A. (1957). *2/(Tc-T),*. *2*, 199–208.

Afifi, H. A., Hager, I. Z., Aal, N. S. A., & Abd El-Aziz, A. M. (2019). Study of the effect of Ni additive in YBa2Cu3O7-δ superconducting composite employing ultrasonic measurement. *Measurement: Journal of the International Measurement Confederation*, *135*, 928–934. https://doi.org/10.1016/j.measurement.2018.12.006

Akhmatskaya, E. V, & Nobes, R. H. (1999). Phase Stability of Inorganic Crystals : A Pseudopotential Plane-Wave Study. *International Journal of Quantum Chemistry*, *77*(2000), 895–910. http://onlinelibrary.wiley.com/doi/10.1002/(SICI)1097-461X(2000)77:5%3C895::AID-QUA10%3E3.0.CO;2-C/abstract

Albaalbaky, A., Kvashnin, Y., Patte, R., Frésard, R., & Ledue, D. (2018). Effects of Ga doping on magnetic and ferroelectric properties of multiferroic delafossite CuCrO2: Ab initio and Monte Carlo approaches. *Physical Review B*, *98*(17), 174403. https://doi.org/10.1103/PhysRevB.98.174403

Alecu, G. (2004). Crystal Structures of Some High-Temperature Superconductors. *Romanian Reports in Physiscs*, *56*(3), 404–412.

Alknes, P., Hagner, M., Bjoerstad, R., Scheuerlein, C., Bordini, B., Sugano, M., Hudspeth, J., & Ballarino, A. (2016). Mechanical Properties and Strain-Induced Filament Degradation of Ex Situ and in Situ MgB2 Wires. *IEEE Transactions on Applied Superconductivity*, *26*(3), 3–7. https://doi.org/10.1109/TASC.2015.2509166

Allen, P. B., & Dynes, R. C. (1975). Superconductivity and phonon softening: II. Lead alloys. *Physical Review B*, *11*(5), 1895–1905. https://doi.org/10.1103/PhysRevB.11.1895

Allen, Philip B. (2000). *I . THEORETICAL INTRODUCTION*. 478–483.

Allender, D., & Bardeen, J. (1973). Model for an exciton mechanism of superconductivity. *Physical Review B*, *7*(3), 1020–1029. https://doi.org/10.1103/PhysRevB.7.1020

Almond, D. P., Qingxian Wang, Freestone, J., Lambson, E. F., Chapman, B., & Saunders, G. A. (1989). An ultrasonic study of superconducting and non-superconducting GdBa 2Cu3O7-x. *Journal of Physics: Condensed Matter*, *1*(38), 6853–6864. https://doi.org/10.1088/0953-8984/1/38/010

Ambrosch-Draxl, C., Sherman, E. Y., Auer, H., & Thonhauser, T. (2004). Pressure-induced hole doping of the Hg-based cuprate superconductors. *Physical Review Letters*, *92*(18), 3–6. https://doi.org/10.1103/PhysRevLett.92.187004

Amin, M. N., Kim, J. S., Lee, Y., & Kim, J. K. (2009). Simulation of the thermal stress in mass concrete using a thermal stress measuring device. *Cement and Concrete Research*, *39*(3), 154–164. https://doi.org/10.1016/j.cemconres.2008.12.008

Ando, Y., Segawa, K., Komiya, S., & Lavrov, A. N. (2002). Electrical Resistivity Anisotropy from Self-Organized One Dimensionality in High-Temperature Superconductors. *Physical Review Letters*, *88*(13), 4. https://doi.org/10.1103/PhysRevLett.88.137005

Antipov, E. V., Abakumov, A. M., & Putilin, S. N. (2002). Chemistry and structure of Hg-based superconducting Cu mixed oxides. *Superconductor Science and Technology*, *15*(7). https://doi.org/10.1088/0953-2048/15/7/201

Antonova, L., Troitskii, A., Mikhailova, G., Demikhov, T., Kuzmichev, S., Skuratov, V., & Semina, V. (2019). Changes in Critical Parameters of GdBa2Cu3O7−x HTS-2G Due to Swift-Ion Irradiation. *Physica Status Solidi (B) Basic Research*, *256*(5), 2–5. https://doi.org/10.1002/pssb.201800255

Article, E., Kieslich, G., Sun, S., & Cheetham, A. K. (2015). Chemical Science An extended Tolerance Factor approach for organic – inorganic perovskites †. *Chemical Science*, *6*, 3430–3433. https://doi.org/10.1039/C5SC00961H

Arute, F., Arya, K., Babbush, R., Bacon, D., Bardin, J. C., Barends, R., Biswas, R., Boixo, S., Brandao, F. G. S. L., Buell, D. A., Burkett, B., Chen, Y., Chen, Z., Chiaro, B., Collins, R., Courtney, W., Dunsworth, A., Farhi, E., Foxen, B., … Martinis, J. M. (2019). Quantum supremacy using a programmable superconducting processor. *Nature*, *574*(7779), 505–510. https://doi.org/10.1038/s41586-019-1666-5

Assirey, E. A. R. (2019). Perovskite synthesis, properties and their related biochemical and industrial application. *Saudi Pharmaceutical Journal*, *27*(6), 817–829. https://doi.org/10.1016/j.jsps.2019.05.003

Atul, D. verma. (2018). d M us pt. *On Certain Distance and Degree Based Topological Indices of Zeolite LTA Frameworks, December 2016*, 11–14.

Babaev, E., & Speight, M. (2005). Semi-Meissner state and neither type-I nor type-II superconductivity in multicomponent superconductors. *Physical Review B - Condensed Matter and Materials Physics*, *72*(18), 1–4. https://doi.org/10.1103/PhysRevB.72.180502

Baiutti, F., Logvenov, G., Gregori, G., Cristiani, G., Wang, Y., Sigle, W., Van Aken, P. A., & Maier, J. (2015). High-temperature superconductivity in space-charge regions of lanthanum cuprate induced by two-dimensional doping. *Nature Communications*, *6*, 1–8. https://doi.org/10.1038/ncomms9586

Bardeen, J., & Stephen, M. (1964). Free-energy difference between normal and superconducting states. *Physical Review*, *136*(6A), 1963–1965. https://doi.org/10.1103/PhysRev.136.A1485

Barham, R. J., & Doetschman, D. C. (1992). Single crystal electron paramagnetic resonance study of Y2BaCu05, a common impurity in the high temperature superconductor, YBa2Cu307. *Journal of Materials Research*, *7*(3), 565–571. https://doi.org/10.1557/JMR.1992.0565

Barišić, N., Wu, D., Dressel, M., Li, L. J., Cao, G. H., & Xu, Z. A. (2010). Electrodynamics of electron-doped iron pnictide superconductors: Normal-state properties. *Physical Review B - Condensed Matter and Materials Physics*, *82*(5), 1–12. https://doi.org/10.1103/PhysRevB.82.054518

Barnes, P. N., Sumption, M. D., & Rhoads, G. L. (2005). Review of high power density superconducting generators: Present state and prospects for incorporating YBCO windings. *Cryogenics*, *45*(10–11), 670–686. https://doi.org/10.1016/j.cryogenics.2005.09.001

Barns, R. L., & Laudise, R. A. (1987). Stability of superconducting YBa2Cu3O7 in the presence of water. *Applied Physics Letters*, *51*(17), 1373–1375. https://doi.org/10.1063/1.98683

Been, E., Lee, W. S., Hwang, H. Y., Cui, Y., Zaanen, J., Devereaux, T., Moritz, B., & Jia, C. (2021). Electronic Structure Trends across the Rare-Earth Series in Superconducting

Infinite-Layer Nickelates. *Physical Review X*, *11*(1), 11050. https://doi.org/10.1103/PhysRevX.11.011050

Benmakhlouf, A., Errandonea, D., Bouchenafa, M., Maabed, S., Bouhemadou, A., & Bentabet, A. (2017). New pressure-induced polymorphic transitions of anhydrous magnesium sulfate. *Dalton Transactions*, *46*(15), 5058–5068. https://doi.org/10.1039/C7DT00539C

Beno, M. A., Soderholm, L., Capone, D. W., Hinks, D. G., Jorgensen, J. D., Grace, J. D., Schuller, I. K., Segre, C. U., & Zhang, K. (1987). Structure of the single-phase high-temperature superconductor YBa 2Cu3O7-δ. *Applied Physics Letters*, *51*(1), 57–59. https://doi.org/10.1063/1.98886

Bobrov, V. S. (1993). Deformation, structure and properties of ceramics and crystals of high-Tc superconductors. *Materials Science and Engineering A*, *164*(1–2), 146–152. https://doi.org/10.1016/0921-5093(93)90652-U

Bolse, W. (1994). Ion-beam induced atomic transport through bi-layer interfaces of low- and medium-Z metals and their nitrides. *Materials Science and Engineering R*, *12*(2), 7–8. https://doi.org/10.1016/0927-796X(94)90001-9

Bondarenko, S. I., Koverya, V. P., Krevsun, A. V., & Link, S. I. (2017). High-temperature superconductors of the family (RE)Ba2Cu3O7-δ and their application (Review Article). *Low Temperature Physics*, *43*(10), 1125–1151. https://doi.org/10.1063/1.5008405

Bouhadda, Y., Bououdina, M., Fenineche, N., & Boudouma, Y. (2013). Elastic properties of perovskite-type hydride NaMgH3 for hydrogen storage. *International Journal of Hydrogen Energy*, *38*(3), 1484–1489. https://doi.org/10.1016/j.ijhydene.2012.11.047

Bray, J. W. (2009). Superconductors in applications; Some practical aspects. *IEEE Transactions on Applied Superconductivity*, *19*(3), 2533–2539. https://doi.org/10.1109/TASC.2009.2019287

Brittles, G. D., Mousavi, T., Grovenor, C. R. M., Aksoy, C., & Speller, S. C. (2015). Persistent current joints between technological superconductors. *Superconductor Science and Technology*, *28*(9), 93001. https://doi.org/10.1088/0953-2048/28/9/093001

Burtch, N. C., Heinen, J., Bennett, T. D., Dubbeldam, D., & Allendorf, M. D. (2018). Mechanical Properties in Metal–Organic Frameworks: Emerging Opportunities and Challenges for Device Functionality and Technological Applications. *Advanced Materials*, *30*(37), 1–18. https://doi.org/10.1002/adma.201704124

Cai, P., Ruan, W., Peng, Y., Ye, C., Li, X., Hao, Z., Zhou, X., Lee, D. H., & Wang, Y. (2016). Visualizing the evolution from the Mott insulator to a charge-ordered insulator in lightly doped cuprates. *Nature Physics*, *12*(11), 1047–1051. https://doi.org/10.1038/nphys3840

Cankurtaran, M., Al-Kheffaji, A., Saunders, G. A., Almond, D. P., & Freestone, J. (1990). The effect of hydrostatic pressure on the elastic behaviour of orthorhombic and tetragonal GdBa2Cu3O7-x. *Superconductor Science and Technology*, *3*(2), 76–80. https://doi.org/10.1088/0953-2048/3/2/005

Cao, Y., Wang, Q., Waugh, J. A., Reber, T. J., Li, H., Zhou, X., Parham, S., Park, S. R., Plumb, N. C., Rotenberg, E., Bostwick, A., Denlinger, J. D., Qi, T., Hermele, M. A., Cao, G., & Dessau, D. S. (2016). Hallmarks of the Mott-metal crossover in the hole-doped pseudospin-1/2 Mott insulator Sr2IrO4. *Nature Communications*, *7*, 1–7. https://doi.org/10.1038/ncomms11367

Cava RJ. (1990). Structural Chemistry and The Local Charge Picture of Copper Oxide Superconductors. *Science*, *247*(4943), 656–662.

Cayado, P., Erbe, M., Kauffmann-Weiss, S., Bühler, C., Jung, A., Hänisch, J., & Holzapfel, B. (2017). Large critical current densities and pinning forces in CSD-grown superconducting GdBa2Cu3O7-x-BaHfO3 nanocomposite films. *Superconductor Science and Technology*, *30*(9). https://doi.org/10.1088/1361-6668/aa7e47

Cbers, A., Gourdon, C., Jeudy, V., & Okada, T. (2005). Normal-state bubbles and lamellae in type-I superconductors. *Physical Review B - Condensed Matter and Materials Physics*, *72*(1), 1–16. https://doi.org/10.1103/PhysRevB.72.014513

Chan, C., Zhang, X., Zhang, Y., Tse, K., Deng, B., Zhang, J., & Zhu, J. (2017). Stepping Stone Mechanism: Carrier-Free Long-Range Magnetism Mediated by Magnetized Cation States in Quintuple Layer. *Chinese Physics Letters*, *35*(1). https://doi.org/10.1088/0256-307X/35/1/017502

Chan, W. K., Flanagan, G., & Schwartz, J. (2013). Spatial and temporal resolution requirements for quench detection in (RE)Ba2Cu3Ox magnets using Rayleigh-scattering-based fiber optic distributed sensing. *Superconductor Science and Technology*, *26*(10). https://doi.org/10.1088/0953-2048/26/10/105015

Chen, C., Liu, L., Wen, Y., Jiang, Y., & Chen, L. (2019). Elastic properties of orthorhombic YBa2Cu3O7 under pressure. *Crystals*, *9*(10), 1–12. https://doi.org/10.3390/cryst9100497

Chiew, S. P., Zhao, M. S., & Lee, C. K. (2014). Mechanical properties of heat-treated high strength steel under fire/post-fire conditions. *Journal of Constructional Steel Research*, *98*, 12–19. https://doi.org/10.1016/j.jcsr.2014.02.003

Christensen, N. E., Svane, A., Laskowski, R., Palanivel, B., Modak, P., Chantis, A. N., Van Schilfgaarde, M., & Kotani, T. (2010). Electronic properties of 3R -CuAlO2 under pressure: Three theoretical approaches. *Physical Review B - Condensed Matter and Materials Physics*, *81*(4), 1–9. https://doi.org/10.1103/PhysRevB.81.045203

Christy, A. G., Angel, R. J., Haines, J., & Clark, S. M. (1994). Crystal structural variation and phase transition in caesium trichlorocuprate at high pressure. *Journal of Physics: Condensed Matter*, *6*(17), 3125–3136. https://doi.org/10.1088/0953-8984/6/17/005

Chung, I., Song, J. H., Im, J., Androulakis, J., Malliakas, C. D., Li, H., Freeman, A. J., Kenney, J. T., & Kanatzidis, M. G. (2012). CsSnI 3: Semiconductor or metal? High electrical conductivity and strong near-infrared photoluminescence from a single material. High hole mobility and phase-transitions. *Journal of the American Chemical Society*, *134*(20), 8579–8587. https://doi.org/10.1021/ja301539s

Cocisnunications, S. S. (1980). *N(ef) <j2>. 33*.

Cococcioni, M., Dal Corso, A., & de Gironcoli, S. (2003). Structural, electronic, and magnetic properties of Fe2SiO4 fayalite: Comparison of LDA and GGA results. *Physical Review B - Condensed Matter and Materials Physics*, *67*(9), 941061–941067. https://doi.org/10.1103/PhysRevB.67.094106

Comodi, P., Mellini, M., & Zanazzi, P. F. (1990). Scapolites: variation of structure with pressure and possible role in the storage of fluids. *European Journal of Mineralogy*, *2*(2), 195–202. https://doi.org/10.1127/ejm/2/2/0195

Congreve, J. V. J., Shi, Y., Huang, K. Y., Dennis, A. R., Durrell, J. H., & Cardwell, D. A. (2019). Improving Mechanical Strength of YBCO Bulk Superconductors by Addition of

Ag. *IEEE Transactions on Applied Superconductivity*, *29*(5), 1–5. https://doi.org/10.1109/TASC.2019.2907474

Cooper, A. J., Harris, J. H., Garrett, S. J., özkan, M., & Thomas, P. J. (2015). The effect of anisotropic and isotropic roughness on the convective stability of the rotating disk boundary layer. *Physics of Fluids, 27*(1), 1–17. https://doi.org/10.1063/1.4906091

Daoud, S., Loucif, K., & Bioud, N. (2012). *Effect of hydrostatic pressure on the structural , elastic and electronic properties of (B3) boron phosphide*. *79*(1), 95–106. https://doi.org/10.1007/s12043-012-0283-8

Delft, D. Van. (2012). History and significance of the discovery of superconductivity by Kamerlingh Onnes in 1911. *Physica C: Superconductivity and Its Applications*, *479*, 30–35. https://doi.org/10.1016/j.physc.2012.02.046

Delft, D. van, & Kes, P. (2010). Experimenting in liquid helium. *Phys. Today*, *63*(9), 38–42. http://snf.ieeecsc.org/sites/ieeecsc.org/files/RN16e.pdf

Dellea, G., Minola, M., Galdi, A., Di Castro, D., Aruta, C., Brookes, N. B., Jia, C. J., Mazzoli, C., Moretti Sala, M., Moritz, B., Orgiani, P., Schlom, D. G., Tebano, A., Balestrino, G., Braicovich, L., Devereaux, T. P., Maritato, L., & Ghiringhelli, G. (2017). Spin and charge excitations in artificial hole- and electron-doped infinite layer cuprate superconductors. *Physical Review B*, *96*(11), 1–8. https://doi.org/10.1103/PhysRevB.96.115117

Dewar, M. J. S. (1987). A New Mechanism For Superconductivity. *Angewandte Chemie International Edition in English*, *26*(12), 1273–1275. https://doi.org/10.1002/anie.198712731

Ding, Z., Zhou, S., & Zhao, Y. (2004). Hardness and fracture toughness of brittle materials: A density functional theory study. *Physical Review B - Condensed Matter and Materials Physics*, *70*(18), 1–6. https://doi.org/10.1103/PhysRevB.70.184117

Dissertations, D. (2015). *ScholarWorks @ UMass Amherst Conjugated Polymers in Thermoelectric Composites and Small Molecules for High Light Absorptivity*. *November*.

Doan, C., Le, H., & Lower, S. (2020). Gibbs (Free) Energy Gibbs Energy in Reactions. *LibreTexts- CHEMISTRY*, *2*(4), 1–7. https://chem.libretexts.org/Bookshelves/Physical_and_Theoretical_Chemistry_Textbook_Maps/Supplemental_Modules_(Physical_and_Theoretical_Chemistry)/Thermodynamics/Energies_and_Potentials/Free_Energy/Gibbs_(Free)_Energy

Dodd, S. P., Cankurtaran, M., & James, B. (2003). Ultrasonic determination of the elastic and nonlinear acoustic properties of transition-metal carbide ceramics: TiC and TaC. *Journal of Materials Science*, *38*(6), 1107–1115. https://doi.org/10.1023/A:1022845109930

Drozdov, A. P., Eremets, M. I., Troyan, I. A., Ksenofontov, V., & Shylin, S. I. (2015). Conventional superconductivity at 203 kelvin at high pressures in the sulfur hydride system. *Nature*, *525*(7567), 73–76. https://doi.org/10.1038/nature14964

Drozdov, A. P., Kong, P. P., Minkov, V. S., Besedin, S. P., Kuzovnikov, M. A., Mozaffari, S., Balicas, L., Balakirev, F. F., Graf, D. E., Prakapenka, V. B., Greenberg, E., Knyazev, D. A., Tkacz, M., & Eremets, M. I. (2019). Superconductivity at 250 K in lanthanum hydride under high pressures. *Nature*, *569*(7757), 528–531. https://doi.org/10.1038/s41586-019-1201-8

Durrell, J. H., Ainslie, M. D., Zhou, D., Vanderbemden, P., Bradshaw, T., Speller, S., Filipenko, M., & Cardwell, D. A. (2018). Bulk superconductors: A roadmap to applications. *Superconductor Science and Technology*, *31*(10). https://doi.org/10.1088/1361-6668/aad7ce

Dutta, A., & Sinha, T. P. (2011). Structural and dielectric properties of A(Fe1/2Ta 1/2)O3 [A = Ba, Sr, Ca]. *Materials Research Bulletin*, *46*(4), 518–524. https://doi.org/10.1016/j.materresbull.2011.01.003

Emin, D. (2017). Dynamic d-symmetry Bose condensate of a planar-large-bipolaron liquid in cuprate superconductors. *Philosophical Magazine*, *97*(31), 2931–2945. https://doi.org/10.1080/14786435.2017.1354137

Engineering, M., Division, C. S., Laboratov, L. B., & Road, O. C. (1991). *One- and*. *168*.

Ernzerhof, M., & Scuseria, G. E. (1999). Assessment of the Perdew-Burke-Ernzerhof exchange-correlation functional. *Journal of Chemical Physics*, *110*(11), 5029–5036. https://doi.org/10.1063/1.478401

Examination of Patent Applications That Include Claims Containing Alternative Language. (2007). In *Biotechnology Law Report* (Vol. 26, Issue 5, pp. 523–536). https://doi.org/10.1089/blr.2007.9919

Fan, D., Fu, S., Yang, J., Tkachev, S. N., Prakapenka, V. B., & Lin, J. F. (2019). Elasticity of single-crystal periclase at high pressure and temperature: The effect of iron on the elasticity and seismic parameters of ferropericlase in the lower mantle. *American Mineralogist*, *104*(2), 262–275. https://doi.org/10.2138/am-2019-6656

Fay, D. L. (1967). *Angewandte Chemie International Edition, 6(11), 951–952.*, *39*(10), 7363–7366.

Fecht, H. J., Wunderlich, R., Battezzati, L., Etay, J., Ricci, E., Seetharaman, S., & Egry, I. (2008). Thermophysical properties of materials. In *Europhysics News* (Vol. 39, Issue 5, pp. 19–21). https://doi.org/10.1051/epn:2008501

Fietz, W. H., & Wuhl, H. (1990). *H.A. LUDWIG, W.H. FIETZ, M.R. DIETRICH and H. WUHL*. *167*(0 17), 335–338.

Fontcuberta, J., Martínez, B., Seffar, A., Piñol, S., García-Muñoz, J. L., & Obradors, X. (1996). Colossal magnetoresistance of ferromagnetic manganites: Structural tuning and mechanisms. *Physical Review Letters*, *76*(7), 1122–1125. https://doi.org/10.1103/PhysRevLett.76.1122

Freysoldt, C., Grabowski, B., Hickel, T., Neugebauer, J., Kresse, G., Janotti, A., & Van De Walle, C. G. (2014). First-principles calculations for point defects in solids. *Reviews of Modern Physics*, *86*(1), 253–305. https://doi.org/10.1103/RevModPhys.86.253

Fröhlich, H. (1950). Theory of the superconducting state. I. The ground state at the absolute zero of temperature. *Physical Review*, *79*(5), 845–856. https://doi.org/10.1103/PhysRev.79.845

Fukuhara, M., Yoshida, H., Inoue, A., & Fujima, N. (2010). Superconductivity and Coulomb oscillation in Ni-Nb-Zr-H glassy alloys with nanoclusters. *Intermetallics*, *18*(10), 1864–1866. https://doi.org/10.1016/j.intermet.2010.01.002

Furness, J. W., Zhang, Y., Lane, C., Buda, I. G., Barbiellini, B., Markiewicz, R. S., Bansil, A., & Sun, J. (2018). An accurate first-principles treatment of doping-dependent electronic structure of high-temperature cuprate superconductors. *Communications Physics*, *1*(1), 1–6. https://doi.org/10.1038/s42005-018-0009-4

Galasso, F. S. (1969). *Properties and Perovskite-Type*. *5*, 1–207.

Gazquez, J., Guzman, R., Mishra, R., Bartolomé, E., Salafranca, J., Magén, C., Varela, M., Coll, M., Palau, A., Valvidares, S. M., Gargiani, P., Pellegrin, E., Herrero-Martin, J., Pennycook, S. J., Pantelides, S. T., Puig, T., & Obradors, X. (2016). Emerging diluted ferromagnetism in high-Tc superconductors driven by point defect clusters. *Advanced Science*, *3*(6), 1–8. https://doi.org/10.1002/advs.201500295

Ghouch, N. El, Al-Oweini, R., & Awad, R. (2020). Effects of Adding Transition Metal-Substituted Polyoxotungstates on the Frequency and Temperature-Dependent Dielectric Properties of (Bi1.8Pb0.4)Sr2Ca2Cu3O10+δ Superconducting Phase. *Journal of Low Temperature Physics*, *200*(1–2), 62–75. https://doi.org/10.1007/s10909-020-02462-x

Gillet, Y., Kontur, S., Giantomassi, M., Draxl, C., & Gonze, X. (2017). Ab Initio Approach to Second-order Resonant Raman Scattering Including Exciton-Phonon Interaction. *Scientific Reports*, *7*(1), 1–10. https://doi.org/10.1038/s41598-017-07682-y

Goldacker, W., Grilli, F., Pardo, E., Kario, A., Schlachter, S. I., & Vojenčiak, M. (2014). Roebel cables from REBCO coated conductors: A one-century-old concept for the superconductivity of the future. *Superconductor Science and Technology*, *27*(9). https://doi.org/10.1088/0953-2048/27/9/093001

Golovach, V. N., Khaetskii, A., & Loss, D. (2004). Phonon-induced decay of the electron spin in quantum dots. *Physical Review Letters*, *93*(1), 1–4. https://doi.org/10.1103/PhysRevLett.93.016601

Goryainov, S. V., Kolesnik, E. N., & Boldyreva, E. V. (2005). A reversible pressure-induced phase transition in β-glycine at 0.76 GPa. *Physica B: Condensed Matter*, *357*(3–4), 340–

347. https://doi.org/10.1016/j.physb.2004.11.089

Granhed, E. J., Wahnström, G., & Hyldgaard, P. (2020). BaZrO3 stability under pressure: The role of nonlocal exchange and correlation. *Physical Review B*, *101*(22), 224105. https://doi.org/10.1103/PhysRevB.101.224105

Greene, R. L., Mandal, P. R., Poniatowski, N. R., & Sarkar, T. (2020). The Strange Metal State of the Electron-Doped Cuprates. *Annual Review of Condensed Matter Physics*, *11*, 213–229. https://doi.org/10.1146/annurev-conmatphys-031119-050558

Haberkorn, N., Kim, J., Suárez, S., Lee, J. H., & Moon, S. H. (2015). Influence of random point defects introduced by proton irradiation on the flux creep rates and magnetic field dependence of the critical current density J c of co-evaporated GdBa2Cu3O7-δ coated conductors. *Superconductor Science and Technology*, *28*(12), 125007. https://doi.org/10.1088/0953-2048/28/12/125007

Hafner, J., & Wolverton, C. (2006). Toward computational materials design: The impact of density functional theory on materials research. *MRS Bulletin*, *31*(9), 659–665. https://doi.org/10.1557/mrs2006.174

Hague, J. P., Kornilovitch, P. E., Samson, J. H., & Alexandrov, A. S. (2007). Superlight small bipolarons in the presence of a strong coulomb repulsion. *Physical Review Letters*, *98*(3), 1–4. https://doi.org/10.1103/PhysRevLett.98.037002

Hao, L. Y., Ji, M., Yuan, J., An, D. Y., Li, M. Y., Zhou, X. J., Huang, Y., Sun, H. C., Zhu, Q., Rudau, F., Wieland, R., Kinev, N., Li, J., Xu, W. W., Jin, B. B., Chen, J., Hatano, T., Koshelets, V. P., Koelle, D., … Wu, P. H. (2015). Compact superconducting terahertz source operating in liquid nitrogen. *Physical Review Applied*, *3*(2), 1–7.

https://doi.org/10.1103/PhysRevApplied.3.024006

Hashimoto, M., Yoshida, T., Yagi, H., Takizawa, M., Fujimori, A., Kubota, M., Ono, K., Tanaka, K., Lu, D. H., Shen, Z. X., Ono, S., & Ando, Y. (2008). Doping evolution of the electronic structure in the single-layer cuprate Bi2 Sr2-x Lax Cu O6+δ: Comparison with other single-layer cuprates. *Physical Review B - Condensed Matter and Materials Physics*, *77*(9), 1–9. https://doi.org/10.1103/PhysRevB.77.094516

Haussühl, E., Reichmann, H. J., Schreuer, J., Friedrich, A., Hirschle, C., Bayarjargal, L., Winkler, B., Alencar, I., Wiehl, L., & Ganschow, S. (2020). Elastic properties of single crystal Bi12SiO20 as a function of pressure and temperature and acoustic attenuation effects in Bi12 MO20 (M = Si, Ge and Ti). *Materials Research Express*, *7*(2). https://doi.org/10.1088/2053-1591/ab6ad6

Hirsch, J. E. (2017). Momentum of superconducting electrons and the explanation of the Meissner effect. *Physical Review B*, *95*(1), 1–15. https://doi.org/10.1103/PhysRevB.95.014503

Hirsch, J. E., & Marsiglio, F. (2019). Hole superconductivity in infinite-layer nickelates. *Physica C: Superconductivity and Its Applications*, *566*(September), 1353534. https://doi.org/10.1016/j.physc.2019.1353534

Hohenwarter, A. (2015). Incremental high pressure torsion as a novel severe plastic deformation process: Processing features and application to copper. *Materials Science and Engineering A*, *626*, 80–85. https://doi.org/10.1016/j.msea.2014.12.041

Holt, A. R., Hunt, J., & Moiseiwitsch, B. L. (1971). Application of a simplified second Born approximation to the scattering of electrons and protons by helium atoms. *Journal of*

Physics B: Atomic and Molecular Physics, *4*(10), 1318–1331. https://doi.org/10.1088/0022-3700/4/10/017

Homes, C. C., Dordevic, S. V., Strongin, M., Bonn, D. A., Liang, R., Hardy, W. H., Komiya, S., Ando, Y., Yu, G., Kaneko, N., Zhao, X., Greven, M., Basov, D. N., & Timusk, T. (2004). A universal scaling relation in high-temperature superconductors. *Nature*, *430*(6999), 539–541. https://doi.org/10.1038/nature02673

Hull, J. R. (2003). Applications of high-temperature superconductors in power technology. *Reports on Progress in Physics*, *66*(11), 1865–1886. https://doi.org/10.1088/0034-4885/66/11/R01

Hull, J. R., & Murakami, M. (2004). Applications of bulk high-temperature superconductors. *Proceedings of the IEEE*, *92*(10), 1705–1717. https://doi.org/10.1109/JPROC.2004.833796

Hwang, H. Y., Cheong, S. W., Radaelli, P. G., Marezio, M., & Batlogg, B. (1995). Lattice effects on the magnetoresistance in doped LaMnO3. *Physical Review Letters*, *75*(5), 914–917. https://doi.org/10.1103/PhysRevLett.75.914

Ikehara, T., & Tsuchiya, T. (2009). Effects of anisotropic elasticity on stress concentration in micro mechanical structures fabricated on (001) single-crystal silicon films. *Journal of Applied Physics*, *105*(9). https://doi.org/10.1063/1.3124368

Inaguma, Y., Aimi, A., Mori, D., Katsumata, T., Ohtake, M., Nakayama, M., & Yonemura, M. (2018). High-Pressure Synthesis, Crystal Structure, Chemical Bonding, and Ferroelectricity of LiNbO 3 -Type LiSbO 3. *Inorganic Chemistry*, *57*(24), 15462–15473. https://doi.org/10.1021/acs.inorgchem.8b02767

Ingosi, A. (2018). Thermodynamic Properties Of YBCO-123 Superconducting Materials With S-Wave And P-Wave Singlet Admixture. *Journal of Multidisciplinary Engineering Science and Technology*, *5*(10), 8790–8793.

Jayalakshmi, V., Murugan, R., & Palanivel, B. (2005). Electronic and structural properties of CuMO 2 (M = Al, Ga, In). *Journal of Alloys and Compounds*, *388*(1), 19–22. https://doi.org/10.1016/j.jallcom.2004.07.009

Jensen, B. B., Mijatovic, N., & Abrahamsen, A. B. (2012). Development of superconducting wind turbine generators. *European Wind Energy Conference and Exhibition 2012, EWEC 2012*, *1*, 169–178.

Jia, S., Qu, R., Li, J., Fang, H., & Li, D. (2016). A Novel Vernier Reluctance Fully Superconducting Direct Drive Synchronous Generator with Concentrated Windings for Wind Power Application. *IEEE Transactions on Applied Superconductivity*, *26*(7). https://doi.org/10.1109/TASC.2016.2576472

Jin, H. J., Kim, G., Jo, W., Shin, H. Y., Yoon, S., Kim, K., & Kim, M. (2015). Spatial investigation on structural properties of GdBa2Cu3O7 - X coated conductors grown on IBAD-MgO based stainless-steel substrates. *IEEE Transactions on Applied Superconductivity, 25*(3). https://doi.org/10.1109/TASC.2014.2385481

Kanel, G. I., Razorenov, S. V., & Fortov, V. E. (2004). Shock-wave compression and tension of solids at elevated temperatures: Superheated crystal states, pre-melting, and anomalous growth of the yield strength. *Journal of Physics Condensed Matter*, *16*(14). https://doi.org/10.1088/0953-8984/16/14/010

Karaca, H. E., Karaman, I., Basaran, B., Ren, Y., Chumlyakov, Y. I., & Maier, H. J. (2009).

Magnetic field-induced phase transformation in NiMnColn magnetic shape-memory alloys-a new actuation mechanism with large work output. *Advanced Functional Materials*, *19*(7), 983–998. https://doi.org/10.1002/adfm.200801322

Kargar, M., Alikhanzadeh-Arani, S., & Salavati-Niasari, M. (2015). Synthesis of Ultrafine High-TC Superconducting GdBa2Cu3O7-x Powder. *IEEE Transactions on Applied Superconductivity*, *25*(4). https://doi.org/10.1109/TASC.2015.2439235

Karlsruhe, F., & Berichte, W. (2006). *Stresses in Oxidized Claddings and Mechanical Stability of Oxide Scales*.

Katz, J. L., & Meunier, A. (1987). The elastic anisotropy of bone. *Journal of Biomechanics*, *20*(11–12), 1063–1070. https://doi.org/10.1016/0021-9290(87)90024-8

Keaton, J. R. (2018). *Bulk Modulus*. 96–96. https://doi.org/10.1007/978-3-319-73568-9_38

Kim, J., Kim, Y., Yoon, S., Shin, K., Lee, J., Jung, J. S., Lee, J. T., Kim, J. G., Kim, D., Yoo, J., Lee, H., Moon, S. H., & Hahn, S. (2020). Design, construction, and operation of an 18 T 70 mm no-insulation (RE)Ba2Cu3O7- x magnet for an axion haloscope experiment. *Review of Scientific Instruments*, *91*(2). https://doi.org/10.1063/1.5124432

Klemm, R. A., & Clem, J. R. (1980). Lower critical field of an anisotropic type-II superconductor. *Physical Review B*, *21*(5), 1868–1875. https://doi.org/10.1103/PhysRevB.21.1868

Klose, W., & Hertel, P. (1970). Transition temperature of superconductors. *Zeitschrift Für Physik A Hadrons and Nuclei*, *239*(4), 331–336. https://doi.org/10.1007/BF01398243

Kröger, F. A., & Nachtrieb, N. H. (1964). The Chemistry of Imperfect Crystals . *Physics Today*, *17*(10), 66–69.

https://doi.org/10.1063/1.3051186

Kumar, A., Chaudhary, S., Meher Abhinav, E., & Mahato, R. N. (2019). Impact of crystal stacking sequence on electrical transport and dielectric properties of the nanocrystalline BaCo0.9Mn0.1O3-δ. *Journal of Alloys and Compounds*, *786*(February), 356–367. https://doi.org/10.1016/j.jallcom.2019.01.319

Kushima, A., & Yildiz, B. (2010). Oxygen ion diffusivity in strained yttria stabilized zirconia: Where is the fastest strain? *Journal of Materials Chemistry*, *20*(23), 4809–4819. https://doi.org/10.1039/c000259c

Lafarge, P., Joyez, P., Esteve, D., Urbina, C., & Devoret, M. H. (1993). Measurement of the even-odd free-energy difference of an isolated superconductor. *Physical Review Letters*, *70*(7), 994–997. https://doi.org/10.1103/PhysRevLett.70.994

Larson, P., Lambrecht, W. R. L., Chantis, A., & Van Schilfgaarde, M. (2007). Electronic structure of rare-earth nitrides using the LSDA+U approach: Importance of allowing 4f orbitals to break the cubic crystal symmetry. *Physical Review B - Condensed Matter and Materials Physics*, *75*(4), 1–14. https://doi.org/10.1103/PhysRevB.75.045114

Le, D., Stolbov, S., & Rahman, T. S. (2009). Reactivity of the Cu2O(1 0 0) surface: Insights from first principles calculations. *Surface Science*, *603*(10–12), 1637–1645. https://doi.org/10.1016/j.susc.2008.12.039

Ledbetter, H. M., Kim, S. A., Lei, M., & Austin, M. W. (1987). Elastic Constants and Debye Temperature of Polycrystalline y1 ba2 cu3 o7 _x. *Journal of Materials Research*, *2*(6), 786–789. https://doi.org/10.1557/JMR.1987.0786

Ledbetter, H. M., Weston, W. F., & Naimon, E. R. (1975). Low-temperature elastic properties of four austenitic stainless steels. *Journal of Applied Physics*, *46*(9), 3855–3860. https://doi.org/10.1063/1.322182

Lee, N., Lee, K., Lee, C., Kim, J., Park, H. Y., Kwak, D., Lee, H., Lim, H., Lee, N., Lee, K., Lee, C., Kim, J., & Parka, H. Y. (1997). *Determination of conduction band tail and Fermi energy of heavily Sidoped GaAs by roomtemperature photoluminescence Determination of conduction band tail and Fermi energy of heavily Si-doped GaAs by room-temperature photoluminescence*. *3367*(1995), 1–5. https://doi.org/10.1063/1.359963

Lee, Y. (1991). *Application of Superconducting Magnetic Energy Storage Unit to Improve Ti ’*-.

Leonard, K. J., Aytug, T., Gapud, A. A., List, F. A., Greenwood, N. T., Zhang, Y., Perez-Bergquist, A. G., & Weber, W. J. (2014). Irradiation response of next generation high temperature superconductors for fusion energy applications. *Fusion Science and Technology*, *66*(1), 57–62. https://doi.org/10.13182/FST13-735

Li, C., Zhao, J., Hu, Q., Liu, Z., Yu, Z., & Yan, H. (2016). Crystal structure and transporting properties of Bi2S3under high pressure: Experimental and theoretical studies. *Journal of Alloys and Compounds*, *688*, 329–335. https://doi.org/10.1016/j.jallcom.2016.06.276

Li, Y., & Barbič, J. (2015). Stable Anisotropic Materials. *IEEE Transactions on Visualization and Computer Graphics*, *21*(10), 1129–1137. https://doi.org/10.1109/TVCG.2015.2448105

Lin, C., Zhang, Y., Liu, J., Li, X., Li, Y., Tang, L., & Xiong, L. (2012). Pressure-induced structural change in orthorhombic perovskite GdMnO 3. *Journal of Physics Condensed*

Matter, *24*(11). https://doi.org/10.1088/0953-8984/24/11/115402

Liu, L., Du, J., Zhao, J., Liu, H., Gao, H., & Chen, Y. (2009). Elastic properties of hydrous forsterites under high pressure: First-principle calculations. *Physics of the Earth and Planetary Interiors*, *176*(1–2), 89–97. https://doi.org/10.1016/j.pepi.2009.04.004

Liuermore, L., Matter, C., Diuision, L., & Box, P. O. (1990). *of YBazCu30,*. *41*(13).

Long, J., Yang, L., & Wei, X. (2013). Lattice, elastic properties and Debye temperatures of ATiO3 (A = Ba, Ca, Pb, Sr) from first-principles. *Journal of Alloys and Compounds*, *549*, 336–340. https://doi.org/10.1016/j.jallcom.2012.08.120

Lozovik, Y., & Yudson, V. (1976). A new mechanism for superconductivity: pairing between spatially separated electrons and holes. *Sov. Phys. JETP*, *44*(2), 389–397. http://www.jetp.ac.ru/cgi-bin/dn/e_044_02_0389.pdf

Luan, X., Qin, H., Liu, F., Dai, Z., Yi, Y., & Li, Q. (2018). The mechanical properties and elastic anisotropies of cubic Ni3Al from first principles calculations. *Crystals*, *8*(8). https://doi.org/10.3390/cryst8080307

Lugovskoi, A. V., Katsnelson, M. I., & Rudenko, A. N. (2019). Electron-phonon properties, structural stability, and superconductivity of doped antimonene. *Physical Review B*, *99*(6), 1–13. https://doi.org/10.1103/PhysRevB.99.064513

Ma, X. G., Liang, P., Miao, L., Bie, S. W., Zhang, C. K., Xu, L., & Jiang, J. J. (2009). Pressure-induced phase transition and elastic properties of TiO2 polymorphs. *Physica Status Solidi (B) Basic Research*, *246*(9), 2132–2139. https://doi.org/10.1002/pssb.200945111

MacHon, D., Pischedda, V., Le Floch, S., & San-Miguel, A. (2018). Perspective: High pressure transformations in nanomaterials and opportunities in material design. *Journal of Applied Physics*, *124*(16). https://doi.org/10.1063/1.5045563

Madsen, G. K. H., & Singh, D. J. (2006). BoltzTraP. A code for calculating band-structure dependent quantities. *Computer Physics Communications*, *175*(1), 67–71. https://doi.org/10.1016/j.cpc.2006.03.007

Mahesh, R., Murugan, R., & Palanivel, B. (2013). Electronic structure, magnetic ordering and phase stability of LiFeX (X = P, As and Sb) under pressure. *Modern Physics Letters B*, *27*(32), 1–14. https://doi.org/10.1142/S0217984913502369

Man, C. S., & Huang, M. (2011). A simple explicit formula for the Voigt-Reuss-Hill average of elastic polycrystals with arbitrary crystal and texture symmetries. *Journal of Elasticity*, *105*(1–2), 29–48. https://doi.org/10.1007/s10659-011-9312-y

Manuscript, A. (1972). Dalton transactions. *Journal of the Chemical Society, Dalton Transactions*, 1772.

Manuscript, A. (2020). *revolutionize the field of spintronics and us pt*.

Mao, H. K., Chen, X. J., Ding, Y., Li, B., & Wang, L. (2018). Solids, liquids, and gases under high pressure. *Reviews of Modern Physics*, *90*(1), 15007. https://doi.org/10.1103/RevModPhys.90.015007

Markiewicz, R. S. (1994). Van Hove exciton-cageons and high-Tc superconductivity XA. Role of spin-orbit coupling in generating a diabolical point. *Physica C: Superconductivity and Its Applications*, *228*(3–4), 227–253. https://doi.org/10.1016/0921-4534(94)90413-8

Marlow, R., Kuriyakose, S., Mesaros, N., Han, H. H., Tomlinson, R., Faust, S. N., Snape, M.

D., Pollard, A. J., & Finn, A. (2018). A phase III, open-label, randomised multicentre study to evaluate the immunogenicity and safety of a booster dose of two different reduced antigen diphtheria-tetanus-acellular pertussis-polio vaccines, when co-administered with measles-mumps-rubella vacci. *Vaccine*, *36*(17), 2300–2306. https://doi.org/10.1016/j.vaccine.2018.03.021

Mattrup, M., & Ravn, S. (2019). *Search for High Poisson ' s Ratio Oxide Glasses*.

Mayssara A. Abo Hassanin Supervised, A. (2014). In *Paper Knowledge . Toward a Media History of Documents*.

Mazin, I. I., Johannes, M. D., Boeri, L., Koepernik, K., & Singh, D. J. (2008). Problems with reconciling density functional theory calculations with experiment in ferropnictides. *Physical Review B - Condensed Matter and Materials Physics*, *78*(8), 1–7. https://doi.org/10.1103/PhysRevB.78.085104

McClean, J. R., Kimchi-Schwartz, M. E., Carter, J., & De Jong, W. A. (2017). Hybrid quantum-classical hierarchy for mitigation of decoherence and determination of excited states. *Physical Review A*, *95*(4), 1–10. https://doi.org/10.1103/PhysRevA.95.042308

Mccoy, S. (2020). *Rare Earth Cuprate Analysis for High Tc Superconducting Devices - ProQuest*. *June*. https://search.proquest.com/docview/2438706682?pq-origsite=gscholar&fromopenview=true

Mech, R., Britain, G., Press, P., Zobackt, S. M. D., Aime, T., Sept, E. J., Mech, R., & Hydraulic, I. (1989). *Jl*. *26*(6), 499–506.

Mehta, A., DiCarlo, J., & Navrotsky, A. (1992). Nature of hole states in cuprate superconductors. *Journal of Solid State Chemistry*, *101*(1), 173–185.

https://doi.org/10.1016/0022-4596(92)90213-F

Meng, W., Wang, X., Xiao, Z., Wang, J., Mitzi, D. B., & Yan, Y. (2017). Parity-Forbidden Transitions and Their Impact on the Optical Absorption Properties of Lead-Free Metal Halide Perovskites and Double Perovskites. *Journal of Physical Chemistry Letters*, *8*(13), 2999–3007. https://doi.org/10.1021/acs.jpclett.7b01042

Mitra, A., Mahapatra, A. S., Mallick, A., Shaw, A., Bhakta, N., & Chakrabarti, P. K. (2018). Improved magneto-electric properties of LaFeO3 in La0.8Gd0.2Fe0.97Nb0.03O3. *Ceramics International*, *44*(4), 4442–4449. https://doi.org/10.1016/j.ceramint.2017.12.045

Mnefgui, S., Dhahri, A., Dhahri, J., & Hlil, E. K. (2013). Effects of transition-metal V-doping on the structural, magnetic and transport properties in La0.67Sr0.33MnO3 manganite oxide. *Journal of Superconductivity and Novel Magnetism*, *26*(2), 251–260. https://doi.org/10.1007/s10948-012-1756-1

Mohammed, A. M., Mohtar, S. S., Aziz, F., Aziz, M., Ul-Hamid, A., Wan Salleh, W. N., Yusof, N., Jaafar, J., & Ismail, A. F. (2021). Ultrafast degradation of Congo Red dye using a facile one-pot solvothermal synthesis of cuprous oxide/titanium dioxide and cuprous oxide/zinc oxide p-n heterojunction photocatalyst. *Materials Science in Semiconductor Processing*, *122*(May 2020), 105481. https://doi.org/10.1016/j.mssp.2020.105481

Mohan, D. G., & Gopi, S. (2020). Induction assisted friction stir welding: a review. *Australian Journal of Mechanical Engineering*, *18*(1), 119–123. https://doi.org/10.1080/14484846.2018.1432089

Molinari, E., Bungaro, C., Gulia, M., Lugli, P., & Rucker, H. (1992). Electron-phonon interactions in two-dimensional systems: A microscopic approach. *Semiconductor Science and Technology*, *7*(3 B). https://doi.org/10.1088/0268-1242/7/3B/016

Monthoux, P., Balatsky, A. V., & Pines, D. (1992). Weak-coupling theory of high-temperature superconductivity in the antiferromagnetically correlated copper oxides. *Physical Review B*, *46*(22), 14803–14817. https://doi.org/10.1103/PhysRevB.46.14803

Mouhat, F., & Coudert, F. X. (2014). Necessary and sufficient elastic stability conditions in various crystal systems. *Physical Review B - Condensed Matter and Materials Physics*, *90*(22), 4–7. https://doi.org/10.1103/PhysRevB.90.224104

Mumtaz, M., Ali, L., Mubasher, Saleh, A., Slimani, Y., Qasim, I., Hassan, M., & Ahmad, Z. (2020). AC-conduction mechanism via dielectric measurements of (Cr)x/(CuTl)-1223 nanoparticles-superconductor composites. *Cryogenics*, *105*(January 2019), 103021. https://doi.org/10.1016/j.cryogenics.2019.103021

Nabi, M., Bhat, T. M., & Gupta, D. C. (2019). Effect of pressure on electronic, magnetic, thermodynamic, and thermoelectric properties of tantalum-based double perovskites Ba2MTaO6 (M = Mn, Cr). *International Journal of Energy Research*, *43*(9), 4229–4242. https://doi.org/10.1002/er.4547

Nakamura, A., Shimojima, T., Sonobe, T., Yoshida, S., Ishizaka, K., Malaeb, W., Shin, S., Iimura, S., Matsuishi, S., & Hosono, H. (2017). Multiple-pseudogap phases in the hydrogen-doped LaFeAsO system. *Physical Review B*, *95*(6), 1–7. https://doi.org/10.1103/PhysRevB.95.064501

Nam, T. H., Petríková, I., & Marvalová, B. (2020). Experimental characterization and viscoelastic modeling of isotropic and anisotropic magnetorheological elastomers. *Polymer Testing*, *81*(November 2019). https://doi.org/10.1016/j.polymertesting.2019.106272

Navrotsky, A. (1998). Energetics and Crystal Chemical Systematic among Ilmenite, Lithium Niobate, and Perovskite Structures. *Chemistry of Materials*, *10*(10), 2787–2793. https://doi.org/10.1021/cm9801901

Nithya, C., & Thiyagaraj, G. (2020). Morphology oriented CuS nanostructures: Superior K-ion storage using surface enhanced pseudocapacitive effects. *Sustainable Energy and Fuels*, *4*(7), 3574–3587. https://doi.org/10.1039/d0se00469c

Noor, N. A., Alay-e-Abbas, S. M., Hassan, M., Mahmood, I., Alahmed, Z. A., & Reshak, A. H. (2017). The under-pressure behaviour of mechanical, electronic and optical properties of calcium titanate and its ground state thermoelectric response. *Philosophical Magazine*, *97*(22), 1884–1901. https://doi.org/10.1080/14786435.2017.1320440

Núñez-Regueiro, M., Freitas, D. C., Brusetti, R., & Marcus, J. (2013). Effect of pressure on the superconductivity of Rb0.19WO 3. *Solid State Communications*, *159*, 26–28. https://doi.org/10.1016/j.ssc.2013.01.012

Ogunjimi, V., Gautam, B., Sebastian, M. A., Haugan, T., & Wu, J. (2020). The effect of APC/YBCO interface on the angular range of effective pinning by one-dimensional artificial pinning centers in YBa2Cu3O7-xnanocomposite films. *IOP Conference Series: Materials Science and Engineering*, *756*(1). https://doi.org/10.1088/1757-899X/756/1/012025

Óò, Å. Ø. Ð. Ð. Þ. Ø., Øóö, Ó. Ù. Æ. Ë. Ñ. Ó. Ò. Ù., Èö, Ù. Ò. Ö. À., Ò, Ä. Ù., Óò, À. Ç. Â.

Ò. Ò. Í., Äá, Æ., & Ââæ, Í. Ê. Ò. . *Metallization of Cu3N Semiconductor under High Pressure*. *426*.

Otto, F., Yang, Y., Bei, H., & George, E. P. (2013). Relative effects of enthalpy and entropy on the phase stability of equiatomic high-entropy alloys. *Acta Materialia*, *61*(7), 2628–2638. https://doi.org/10.1016/j.actamat.2013.01.042

Otto, H. H. (2016). A Different Approach to High-Tc Superconductivity: Indication of Filamentary-Chaotic Conductance and Possible Routes to Room Temperature Superconductivity. *World Journal of Condensed Matter Physics*, *06*(03), 244–260. https://doi.org/10.4236/wjcmp.2016.63023

Ozturk, O., Arebat, R. A. M., Nefrow, A. R. A., Bulut, F., Guducu, G., Asikuzun, E., & Celik, S. (2019). Investigation of structural, superconducting and mechanical properties of Co/Cu substituted YBCO-358 ceramic composites. *Journal of Materials Science: Materials in Electronics*, *0*(0), 0. https://doi.org/10.1007/s10854-019-01053-1

P. Monthoux, A. V. Balatsky, D. P. (1992). Correlated Copper Oxides. *Physical Review B*, *46*(22), 14803.

Panin, V. E., Panin, A. V., Elsukova, T. F., & Popkova, Y. F. (2015). Fundamental role of crystal structure curvature in plasticity and strength of solids. *Physical Mesomechanics*, *18*(2), 89–99. https://doi.org/10.1134/S1029959915020010

Park, N. G. (2015). Perovskite solar cells: An emerging photovoltaic technology. *Materials Today*, *18*(2), 65–72. https://doi.org/10.1016/j.mattod.2014.07.007

Pavlidis, T., Ganten, M., Lehner, B., Düx, M., & Loew, M. (2003). Tenoplastik der langen bizepssehne bei großem defekt der rotatorenmanschette. *Zeitschrift Fur Orthopadie Und*

Ihre Grenzgebiete, *141*(2), 177–181. https://doi.org/10.1055/s-2003-38660

Pęczkowski, P., Kowalik, M., Jaegermann, Z., Szterner, P., Zachariasz, P., & Woch, W. M. (2019). Synthesis and physicochemical properties of Er 0.5 Dy 0.5 Ba 2 Cu 3 O 6.83 cuprate high-temperature superconductor. *Acta Physica Polonica A*, *135*(1), 28–35. https://doi.org/10.12693/APhysPolA.135.28

Peng, X., Yong, H., & Zhou, Y. (2020). Finite element modeling of single-lap joint between GdBa2Cu3O7-x-coated conductors using cohesive elements. *Physica C: Superconductivity and Its Applications*, *570*(January), 1353600. https://doi.org/10.1016/j.physc.2020.1353600

Pereiro, J., Petrovic, A., Panagopoulos, C., & Božović, I. (2011). *Interface superconductivity: History, development and prospects*. *631*. http://arxiv.org/abs/1111.4194

Peverati, R., & Truhlar, D. G. (2012). Exchange-correlation functional with good accuracy for both structural and energetic properties while depending only on the density and its gradient. *Journal of Chemical Theory and Computation*, *8*(7), 2310–2319. https://doi.org/10.1021/ct3002656

Physical properties of tissue: a ... - Google Books. (n.d.). http://books.google.com/books/about/Physical_properties_of_tissue.html?id=Gl1qAAAAMAAJ

Piskunov, S., Heifets, E., Eglitis, R. I., & Borstel, G. (2004). Bulk properties and electronic structure of SrTiO3, BaTiO 3, PbTiO3 perovskites: An ab initio HF/DFT study. *Computational Materials Science*, *29*(2), 165–178. https://doi.org/10.1016/j.commatsci.2003.08.036

Poole, C., Baig, T., Deissler, R. J., Doll, D., Tomsic, M., & Martens, M. (2016). Numerical study on the quench propagation in a 1.5 T MgB2 MRI magnet design with varied wire compositions. *Superconductor Science and Technology*, *29*(4), 0. https://doi.org/10.1088/0953-2048/29/4/044003

Priya, S., Ando, A., & Sakabe, Y. (2003). Nonlead perovskite materials: Ba(Li1/4Nb3/4)O3 and Ba(cu1/3Nb2/3)O3. *Journal of Applied Physics*, *94*(2), 1171–1177. https://doi.org/10.1063/1.1585121

Progress, O. (2016). *a 2 / B*. *3*(7).

Pu, C., Ma, B., Wang, H., Tang, X., & Zhou, D. (2020). Exploring the real ground-state structures of W3Si silicides from first-principles calculations. *Computational Materials Science*, *180*(April), 109719. https://doi.org/10.1016/j.commatsci.2020.109719

Pugh, S. F. (2016). *XCII . Relations between the elastic moduli and the plastic properties of polycrystalline pure metals*. *5982*(December). https://doi.org/10.1080/14786440808520496

Qd, T., & Qd, T. (2003). *600 700 800 900 1000 Wavelength (nm)*. *12*(16), 1–2. papers3://publication/uuid/B70921F0-0FD8-447C-B739-0179D945BD1A

Qu, R., Liu, Y., & Wang, J. (2013). Review of superconducting generator topologies for direct-drive wind turbines. *IEEE Transactions on Applied Superconductivity*, *23*(3). https://doi.org/10.1109/TASC.2013.2241387

Radebaugh, R. (2012). Cryocoolers for aircraft superconducting generators and motors. *AIP Conference Proceedings*, *1434*(57), 171–182. https://doi.org/10.1063/1.4706918

Rahim, A. H. M. A., & Mohammad, A. M. (1994). Improvement of synchronous generator damping through superconducting magnetic energy storage systems. *IEEE Transactions on Energy Conversion*, *9*(4), 736–742. https://doi.org/10.1109/60.368333

Rajalakshmi, K., Gunasekaran, S., & Kumaresan, S. (2015). Density functional theory, comparative vibrational spectroscopic studies, highest occupied molecular orbital and lowest unoccupied molecular orbital analysis of Linezolid. *Indian Journal of Physics*, *89*(6), 525–538. https://doi.org/10.1007/s12648-014-0618-z

Ramli, A., Halim, S. A., Chen, S. K., & Kechik, M. M. A. (2016). The effect of Gd2O3 nanoparticles addition on microstructural and electrical properties of YBCO superconductor. *ARPN Journal of Engineering and Applied Sciences*, *11*(23), 13708–13715.

Ravindran, P., Fast, L., Korzhavyi, P. A., Johansson, B., Wills, J., & Eriksson, O. (1998). Density functional theory for calculation of elastic properties of orthorhombic crystals: Application to TiSi2. *Journal of Applied Physics*, *84*(9), 4891–4904. https://doi.org/10.1063/1.368733

Razia, S., Murikoli, S. P., Surendran, V., & Upendran, S. (2009). Doping dependent metal to insulator transition in the (Bi, Pb)-2212 system: The evolution of structural and electronic properties with europium substitution. *Chinese Physics B*, *18*(9), 4000–4006. https://doi.org/10.1088/1674-1056/18/9/064

Reynaud, C., Thévenot, F., Chartier, T., & Besson, J. L. (2005). Mechanical properties and mechanical behaviour of SiC dense-porous laminates. *Journal of the European Ceramic Society*, *25*(5), 589–597. https://doi.org/10.1016/j.jeurceramsoc.2004.02.009

Rieck, C. T., Fay, D., & Tewordt, L. (1990). Energy gap, Tc, and density of states in high-temperature superconductors for retarded s- and d-wave interactions. *Physical Review B*, *41*(10), 7289–7292. https://doi.org/10.1103/PhysRevB.41.7289

Rieck, C. T., Little, W. A., Ruvalds, J., & Virosztek, A. (1995). Infrared and microwave spectra of an energy gap in high-temperature superconductors. *Physical Review B, 51*(6), 3772–3782. https://doi.org/10.1103/PhysRevB.51.3772

Rivero, P., García-Suárez, V. M., Pereñiguez, D., Utt, K., Yang, Y., Bellaiche, L., Park, K., Ferrer, J., & Barraza-Lopez, S. (2015). Systematic pseudopotentials from reference eigenvalue sets for DFT calculations. *Computational Materials Science*, *98*, 372–389. https://doi.org/10.1016/j.commatsci.2014.11.026

Rizi, vahid salimian. (2019). Ce Pte Us Pt. *Materials Research Express*, 0–12.

Robinson, J., Xi, K., Kumar, R. V., Ferrari, A. C., Au, H., Titirici, M.-M., Parra Puerto, A., Kucernak, A., Fitch, S. D. S., & Garcia-Araez, N. (2020). High Power Density Superconducting Machines – Development Status and Technology Roadmap. *J. Phys. Energy*, *2*, 0–31.

Rosenstein, B., & Li, D. (2010). Ginzburg-Landau theory of type II superconductors in magnetic field. *Reviews of Modern Physics*, *82*(1), 109–168. https://doi.org/10.1103/RevModPhys.82.109

Ru, Y., Yong, H., & Zhou, Y. (2018). Fracture analysis of bulk superconductors under electromagnetic force. *Engineering Fracture Mechanics*, *199*, 257–273. https://doi.org/10.1016/j.engfracmech.2018.05.024

Ruhman, J., & Lee, P. A. (2016). Superconductivity at very low density: The case of strontium titanate. *Physical Review B*, *94*(22).

https://doi.org/10.1103/PhysRevB.94.224515

Sahu, A. K., Singh, A., Jha, P. K., Sanyal, S. P., & Technology, I. (2011). *Phase Transitions : A Multinational Pressure-induced structural phase transition and electronic properties of RESb (RE = Ho , Er and Tm) compounds : ab initio calculations*. *October 2014*, 37–41. https://doi.org/10.1080/01411594.2010.545939

Sakai, S., Motome, Y., & Imada, M. (2010). Doped high- Tc cuprate superconductors elucidated in the light of zeros and poles of the electronic Green's function. *Physical Review B - Condensed Matter and Materials Physics*, *82*(13), 1–16. https://doi.org/10.1103/PhysRevB.82.134505

Sanz, S., Arlaban, T., Manzanas, R., Tropeano, M., Funke, R., Ková, P., Yang, Y., Neumann, H., & Mondesert, B. (2014). Superconducting light generator for large offshore wind turbines. *Journal of Physics: Conference Series*, *507*(PART 3). https://doi.org/10.1088/1742-6596/507/3/032040

Sarkar, J., & Bhattacharyya, S. (2012). Application of graphene and graphene-based materials in clean energy-related devices Minghui. *Archives of Thermodynamics*, *33*(4), 23–40. https://doi.org/10.1002/er

Sato, H., & Naito, M. (1997). Increase in the superconducting transition temperature by anisotropic strain effect in (001) La1.85Sr0.15CuO4 thin films on LaSrAlO4 substrates. *Physica C: Superconductivity and Its Applications*, *274*(3–4), 221–226. https://doi.org/10.1016/S0921-4534(96)00675-2

Schabel, M. C., & Park, C. (1998). Angle-resolved photoemission on untwinned. I. Electronic structure and dispersion relations of surface and bulk bands. *Physical Review B -*

Condensed Matter and Materials Physics, *57*(10), 6090–6106. https://doi.org/10.1103/PhysRevB.57.6090

Schrieffer, J. R. (2018). Theory of super conductivity. *Theory of Superconductivity*, 1–332. https://doi.org/10.1201/9780429495700

Senatore, C., Alessandrini, M., Lucarelli, A., Parizh, M., Lvovsky, Y., Sumption, M., & Parkinson, B. (n.d.). *conductors compositions Design considerations and experimental results for MRI systems using HTS magnets*.

Senatore, C., Barth, C., Bonura, M., Kulich, M., & Mondonico, G. (2016). Field and temperature scaling of the critical current density in commercial REBCO coated conductors. *Superconductor Science and Technology*, *29*(1), 14002. https://doi.org/10.1088/0953-2048/29/1/014002

Shan, W., Walukiewicz, W., Iii, J. W. A., Yu, K. M., Wu, J., Haller, E. E., Shan, W., Walukiewicz, W., Iii, J. W. A., Yu, K. M., & Wu, J. (2013). *Pressure dependence of the fundamental band-gap energy of CdSe Pressure dependence of the fundamental band-gap energy of CdSe*. *67*(2004), 2002–2005. https://doi.org/10.1063/1.1638879

Shapiro, I., & Shapiro, B. Y. (2019). Intermediate state in a type-I superconducting sphere: Pinning and size effect. *Superconductor Science and Technology*, *32*(8). https://doi.org/10.1088/1361-6668/ab1f56

Shen, G., & Mao, H. K. (2017). High-pressure studies with x-rays using diamond anvil cells. *Reports on Progress in Physics*, *80*(1), 16101. https://doi.org/10.1088/1361-6633/80/1/016101

Shimojima, T., Malaeb, W., Nakamura, A., Kondo, T., Kihou, K., Lee, C. H., Iyo, A., Eisaki, H., Ishida, S., Nakajima, M., Uchida, S. I., Ohgushi, K., Ishizaka, K., & Shin, S. (2017). Antiferroic electronic structure in the nonmagnetic superconducting state of the iron-based superconductors. *Science Advances*, *3*(8), 1–7. https://doi.org/10.1126/sciadv.1700466

Shin, H. S., & Bautista, Z. (2019). Establishing a test procedure for evaluating the electromechanical properties of practical REBCO coated conductor tapes by the uniaxial tension test at 77 K. *Superconductor Science and Technology*, *32*(6), 64004. https://doi.org/10.1088/1361-6668/ab0309

Shin, H. S., & Bautista, Z. M. (2018). Evaluation of Irreversible Strain/Stress Limits for Ic Degradation in Practical REBCO CC Tapes Under Uniaxial Tension. *IEEE Transactions on Applied Superconductivity*, *28*(4). https://doi.org/10.1109/TASC.2017.2788078

Shirane, G., Danner, H., & Pepinsky, R. (1957). Neutron diffraction study of orthorhombic BaTio3. *Physical Review*, *105*(3), 856–860. https://doi.org/10.1103/PhysRev.105.856

Siebentritt, S., Igalson, M., Persson, C., & Lany, S. (2010). The electronic structure of chalcopyrites - Bands, point defects and grain boundaries. *Progress in Photovoltaics: Research and Applications*, *18*(6), 390–410. https://doi.org/10.1002/pip.936

Silvarajoo, S., Osman, U. M., Kamarudin, K. H., Razali, M. H., Yusoff, H. M., Bhat, I. U. H., Rozaini, M. Z. H., & Juahir, Y. (2020). Dataset of theoretical Molecular Electrostatic Potential (MEP), Highest Occupied Molecular Orbital-Lowest Unoccupied Molecular Orbital (HOMO-LUMO) band gap and experimental cole-cole plot of 4-(ortho-, meta- and para-fluorophenyl)thiosemicarbazide isomers. *Data in Brief*, *32*, 0–8. https://doi.org/10.1016/j.dib.2020.106299

Singh, L., Rai, U. S., Mandal, K. D., & Singh, N. B. (2014). Progress in the growth of CaCu3Ti4O12 and related functional dielectric perovskites. *Progress in Crystal Growth and Characterization of Materials*, *60*(2), 15–62. https://doi.org/10.1016/j.pcrysgrow.2014.04.001

Single-Slit Diffraction – University Physics Volume 3. (n.d.). https://opentextbc.ca/universityphysicsv3openstax/chapter/single-slit-diffraction/

Slater, J. C., & Johnson, K. H. (1972). Self-consistent-field Xα cluster method for polyatomic molecules and solids. *Physical Review B*, *5*(3), 844–853. https://doi.org/10.1103/PhysRevB.5.844

Stampfl, C., Mannstadt, W., Asahi, R., & Freeman, A. J. (2001). Electronic structure and physical properties of early transition metal mononitrides: Density-functional theory LDA, GGA, and screened-exchange LDA FLAPW calculations. *Physical Review B - Condensed Matter and Materials Physics*, *63*(15), 1–11. https://doi.org/10.1103/PhysRevB.63.155106

Stolyarova, S. V., Simanovskis, A. A., & Petrov, A. E. (1992). The effect of neutron irradiation on mechanical properties of GdBa2Cu3O7_x ceramics. *Ferroelectrics*, *131*(1), 363–367. https://doi.org/10.1080/00150199208223440

Stoyanova-Ivanova, A. K., Terzieva, S. D., Ivanova, G. D., Mladenov, M. A., Kovacheva, D. G., Raicheff, R. G., Georgieva, S. I., Blagoev, B. S., Zlaeski, A. J., & Mikli, V. (2015). The use of high-temperature superconducting cuprate as a dopant to the negative electrode in Ni-Zn batteries. *Bulgarian Chemical Communications*, *47*(September), 41–48.

Sugano-Segura, A. T. R., Tavares, L. B., Rizzi, J. G. F., Rosa, D. S., Salvadori, M. C., & dos Santos, D. J. (2017). Mechanical and thermal properties of electron beam-irradiated polypropylene reinforced with Kraft lignin. *Radiation Physics and Chemistry*, *139*, 5–10. https://doi.org/10.1016/j.radphyschem.2017.05.016

Sun, J., Remsing, R. C., Zhang, Y., Sun, Z., Ruzsinszky, A., Peng, H., Yang, Z., Paul, A., Waghmare, U., Wu, X., Klein, M. L., & Perdew, J. P. (2016). Accurate first-principles structures and energies of diversely bonded systems from an efficient density functional. *Nature Chemistry*, *8*(9), 831–836. https://doi.org/10.1038/nchem.2535

Sun, L., Gao, Y., Yoshida, K., Yano, T., & Wang, W. (2017). Prediction on structural, mechanical and thermal properties of Al4SiC4, Al4C3 and 4H-SiC under high pressure by first-principles calculation. *Modern Physics Letters B*, *31*(9), 1–15. https://doi.org/10.1142/S0217984917500804

Sun, X., Li, Z., Wang, X., & Li, C. (2019). Technology development of electric vehicles: A review. *Energies*, *13*(1), 1–29. https://doi.org/10.3390/en13010090

Sung, H. H., Chou, S. Y., Syu, K. J., & Lee, W. H. (2008). The antipressure effect of Cu on Tc in superconducting La(Ni1-xCux)C2 (0≤x≤0.25). *Journal of Physics Condensed Matter*, *20*(16). https://doi.org/10.1088/0953-8984/20/16/165207

Sureshkumar, R., & Beris, A. N. (1995). Effect of artificial stress diffusivity on the stability of numerical calculations and the flow dynamics of time-dependent viscoelastic flows. *Journal of Non-Newtonian Fluid Mechanics*, *60*(1), 53–80. https://doi.org/10.1016/0377-0257(95)01377-8

The Electromagnetic Equations of the Supraconductor. (1934). *85*(1933).

Takada, Y. (1978). Plasmon Mechanism of Superconductivity in Two- and Three-Dimensional Electron Systems. In *Journal of the Physical Society of Japan* (Vol. 45, Issue 3, pp. 786–794). https://doi.org/10.1143/JPSJ.45.786

Tallon, J. L. (2005). Oxygen in high-Tc cuprate superconductors. In *Frontiers in Superconducting Materials* (Issue February). https://doi.org/10.1007/3-540-27294-1_7

Tran, D. H., Putri, W. B. K., Kang, B., Lee, N. H., Kang, W. N., & Seong, W. K. (2013). Reducing thickness dependence of critical current density in GdBa 2Cu3O7δ thin films by addition of nanostructured defects. *Journal of Applied Physics*, *113*(17), 2011–2014. https://doi.org/10.1063/1.4798233

Troitskii, A. V., Antonova, L. K., Demikhov, T. E., Skuratov, V. A., Semina, V. K., & Mikhailova, G. N. (2020). The effect of Xe ion irradiation (40, 80 MeV) on HTS-2G GdBa2Cu3O7−x. *Physica C: Superconductivity and Its Applications*, *572*(February), 1353631. https://doi.org/10.1016/j.physc.2020.1353631

Urry, D. W. (2004). The change in Gibbs free energy for hydrophobic association: Derivation and evaluation by means of inverse temperature transitions. *Chemical Physics Letters*, *399*(1–3), 177–183. https://doi.org/10.1016/j.cplett.2004.09.137

Van Harlingen, D. J. (1995). Phase-sensitive tests of the symmetry of the pairing state in the high-temperature superconductors-Evidence for dx2-y2 symmetry. *Reviews of Modern Physics*, *67*(2), 515–535. https://doi.org/10.1103/RevModPhys.67.515

Varignon, J., Grisolia, M. N., Íñiguez, J., Barthélémy, A., & Bibes, M. (2017). Complete phase diagram of rare-earth nickelates from first-principles. *Npj Quantum Materials*, *2*(1), 1–8. https://doi.org/10.1038/s41535-017-0024-9

Vatandoost, H., Hemmatian, M., Sedaghati, R., & Rakheja, S. (2020). Dynamic characterization of isotropic and anisotropic magnetorheological elastomers in the oscillatory squeeze mode superimposed on large static pre-strain. *Composites Part B: Engineering*, *182*, 107648. https://doi.org/10.1016/j.compositesb.2019.107648

Vélez, S., García-Santiago, A., Hernandez, J. M., & Tejada, J. (2009). Rotating magnetic field experiments in a pure superconducting Pb sphere. *Physical Review B - Condensed Matter and Materials Physics*, *80*(14), 1–7. https://doi.org/10.1103/PhysRevB.80.144502

Vickery, R. C., & Klann, A. (1957). Crystallographic and magnetochemical studies on ABO3 group compounds of lanthanon and manganese oxides. *The Journal of Chemical Physics*, *27*(5), 1161–1163. https://doi.org/10.1063/1.1743949

Villalobos-Portillo, E. E., Fuentes-Montero, L., Montero-Cabrera, M. E., Burciaga-Valencia, D. C., & Fuentes-Cobas, L. E. (2019). Polycrystal piezoelectricity: Revisiting the Voigt-Reuss-Hill approximation. *Materials Research Express*, *6*(11). https://doi.org/10.1088/2053-1591/ab46f2

Vinet, L., & Zhedanov, A. (2011). A “missing” family of classical orthogonal polynomials. *Journal of Physics A: Mathematical and Theoretical*, *44*(8), 951–952. https://doi.org/10.1088/1751-8113/44/8/085201

Vittayakorn, N., Rujijanagul, G., Tunkasiri, T., Tan, X., & Cann, D. P. (2003). Perovskite phase formation and ferroelectric properties of the lead nickel niobate-lead zinc niobate-lead zirconate titanate ternary system. *Journal of Materials Research*, *18*(12), 2882–2889. https://doi.org/10.1557/JMR.2003.0402

Wang, J., Mu, X., Wang, L., & Sun, M. (2019). Properties and applications of new superlattice: twisted bilayer graphene. *Materials Today Physics*, *9*. https://doi.org/10.1016/j.mtphys.2019.100099

Wang, P., Piao, C. G., Meng, R. Y., Cheng, Y., & Ji, G. F. (2011). Elastic and electronic properties of YNi2B2C under pressure from first principles. *Physica B: Condensed Matter*, *407*(2), 227–231. https://doi.org/10.1016/j.physb.2011.10.035

Wang, Y., & Chubukov, A. (2014). Charge-density-wave order with momentum (2Q,0) and (0,2Q) within the spin-fermion model: Continuous and discrete symmetry breaking, preemptive composite order, and relation to pseudogap in hole-doped cuprates. *Physical Review B - Condensed Matter and Materials Physics*, *90*(3), 1–52. https://doi.org/10.1103/PhysRevB.90.035149

Wang, Y., & Chubukov, A. (2015). Superconducting and charge-density-wave orders in the spin-fermion model: A comparative analysis. *Physical Review B - Condensed Matter and Materials Physics*, *91*(19), 1–8. https://doi.org/10.1103/PhysRevB.91.195113

Wei, Q., Zhao, C., Zhang, M., Yan, H., & Wei, B. (2019). High-pressure phases and pressure-induced phase transition of MoN6 and ReN6. *Physics Letters, Section A: General, Atomic and Solid State Physics*, *383*(20), 2429–2435. https://doi.org/10.1016/j.physleta.2019.04.061

Wejgaard, W. (1969). Effect of pressure on the superconducting transition temperature of iridium. *Physics Letters A*, *29*(7), 396–397. https://doi.org/10.1016/0375-9601(69)90324-7

Wen, C. H. P., Xu, H. C., Chen, C., Huang, Z. C., Lou, X., Pu, Y. J., Song, Q., Xie, B. P., Abdel-Hafiez, M., Chareev, D. A., Vasiliev, A. N., Peng, R., & Feng, D. L. (2016).

Anomalous correlation effects and unique phase diagram of electron-doped FeSe revealed by photoemission spectroscopy. *Nature Communications*, *7*, 1–7. https://doi.org/10.1038/ncomms10840

Witting, I. T., Chasapis, T. C., Ricci, F., Peters, M., Heinz, N. A., Hautier, G., & Snyder, G. J. (2019). The Thermoelectric Properties of Bismuth Telluride. *Advanced Electronic Materials*, *5*(6). https://doi.org/10.1002/aelm.201800904

Woolley, R. G., & Sutcliffe, B. T. (1977). Molecular structure and the born-Oppenheimer approximation. *Chemical Physics Letters*, *45*(2), 393–398. https://doi.org/10.1016/0009-2614(77)80298-4

Xie, W. (2014). *Charge transport in single crystal organic semiconductors(3)*. http://gradworks.umi.com/36/03/3603278.html

Xinxin Zhang. (2016). *Developing High Performance and Stable Hetero-Structured Cathodes and Fundamental Understanding of Oxygen Reduction and Reaction Behavior*. 134.

Xu, M., Gao, Y., Wang, Y., & Wöll, C. (2010). Monitoring electronic structure changes of TiO2(110) via sign reversal of adsorbate vibrational bands. *Physical Chemistry Chemical Physics*, *12*(15), 3649–3652. https://doi.org/10.1039/b926602j

Yin, X., Tang, C. S., Zeng, S., Asmara, T. C., Yang, P., Naradipa, M. A., Trevisanutto, P. E., Shirakawa, T., Kim, B. H., Yunoki, S., Breese, M. B. H., Venkatesan, T., Wee, A. T. S., Ariando, A., & Rusydi, A. (2019). Quantum Correlated Plasmons and Their Tunability in Undoped and Doped Mott-Insulator Cuprates. *ACS Photonics*, *6*(12), 3281–3289. https://doi.org/10.1021/acsphotonics.9b01294

Yoon, S., Kim, J., Lee, H., Hahn, S., & Moon, S. H. (2016). 26 T 35 mm all-GdBa2Cu3O7-x multi-width no-insulation superconducting magnet. *Superconductor Science and Technology*, *29*(4), 0. https://doi.org/10.1088/0953-2048/29/4/04LT04

Yu, H. S., He, X., & Truhlar, D. G. (2016). MN15-L: A New Local Exchange-Correlation Functional for Kohn-Sham Density Functional Theory with Broad Accuracy for Atoms, Molecules, and Solids. *Journal of Chemical Theory and Computation*, *12*(3), 1280–1293. https://doi.org/10.1021/acs.jctc.5b01082

Yuan, H. Q., Singleton, J., Balakirev, F. F., & Baily, S. A. (n.d.). *Nearly Isotropic superconductivity in (Ba , K) Fe 2 As 2*. 1–15.

Zein, A., Hantke, M., & Warnecke, G. (2010). Modeling phase transition for compressible two-phase flows applied to metastable liquids. *Journal of Computational Physics*, *229*(8), 2964–2998. https://doi.org/10.1016/j.jcp.2009.12.026

Zhang, C., Li, L., Yuan, Z., Xu, X., Song, Z., & Zhang, Y. R. (2020). Mechanical properties of siderite and hematite from DFT calculation. *Minerals Engineering*, *146*(October 2019), 106107. https://doi.org/10.1016/j.mineng.2019.106107

Zhang, N. (2020). Authors : Ac ce d M us pt. *2D Materials*. https://iopscience.iop.org/article/10.1088/2053-1583/abe778

Zhang, R., Gao, P., Wang, X., & Zhou, Y. (2015). First-principles study on elastic and superconducting properties of Nb3Sn and Nb3Al under hydrostatic pressure. *AIP Advances*, *5*(10). https://doi.org/10.1063/1.4935099

Zhang, W., & Osamura, K. (1991). Stability and crystal structure of LnBa6Cu3Ox phase (Ln=lanthanide). *Physica C: Superconductivity and Its Applications*, *174*(1–3), 126–134. https://doi.org/10.1016/0921-4534(91)90428-2

Zhao, H., Xu, X., Li, C., Tian, R., Zhang, R., Huang, R., Lyu, Y., Li, D., Hu, X., Pan, L., & Wang, Y. (2017). Cobalt-doping in Cu2SnS3: Enhanced thermoelectric performance by synergy of phase transition and band structure modification. *Journal of Materials Chemistry A*, *5*(44), 23267–23275. https://doi.org/10.1039/c7ta07140j

Zhou, J. P., Jones, C. E., Mcdevitt, J. T., Gim, Y., Goodenough, B., & Kwon, C. (2002). *Ieee Transactions on Applied Superconductivity, VOL. 9, NO. 2, June 1999.pdf*. *9*(2), 2002–2005.

Zhou, W. L., Wang, C. A., Fung, K. K., Li, H. C., & Li, L. (1994). Transmission electron microscopy study of fine a-axis-oriented grains as flux-pinning centers in YBa2Cu3O7-x/ZrO2(Y) thin film. *Physica C: Superconductivity and Its Applications*, *235–240*(PART 1), 599–600. https://doi.org/10.1016/0921-4534(94)91523-7

Zhu, J., Zhang, J. L., Kong, P. P., Zhang, S. J., Yu, X. H., Zhu, J. L., Liu, Q. Q., Li, X., Yu, R. C., Ahuja, R., Yang, W. G., Shen, G. Y., Mao, H. K., Weng, H. M., Dai, X., Fang, Z., Zhao, Y. S., & Jin, C. Q. (2013). Superconductivity in topological insulator Sb 2 Te 3 induced by pressure. *Scientific Reports*, *3*, 6–11. https://doi.org/10.1038/srep02016

Zhu, T., & Gao, S. P. (2014). The stability, electronic structure, and optical property of tio 2 polymorphs. *Journal of Physical Chemistry C*, *118*(21), 11385–11396. https://doi.org/10.1021/jp412462m

Литовцы. (2018). Authors : Ac ce d M us pt. *2D Materials*, 0–23. https://iopscience.iop.org/article/10.1088/2053-1583/abe778

APPENDICES

APPENDIX I: 1.1 The Quantum Espresso Code

This is an open source full *ab intio* package for implementing electronic structure and energy calculations. The package uses the plane wave self-consistent field (PWSCF) code with pseudo potential within the framework of the density functional theory (DFT). Using the code for the first principal calculations, it is necessary to ensure convergence of the energy cutoff which ensure proper wave function expansion and also proper choice of the k-points which gives a measure of how best the grid as given approximation to the continuous integral

APPENDIX II

1.1 Steps in Band Structure Calculation

When using the plane wave self-consistence and the pseudo potential method you involve four main steps namely; relax, scf, nscf (in which a denser grid of k-points is required), the calculation of the bands and post processing in using the bands.x calculation. In this work the plotting of the bands was done using the grace plotting software. The steps are as follows:

1.2 Relax Calculation

This is the first step and is meant to allow the atoms take their desired position. The input file for the relax should be:

```
&control
pseudo_dir  = './
 calculation = 'relax', ‘
  prefix = 'Gab',
  restart_mode='from_scratch',
  tstress =.true.,
  tprnfor =.true.,
/
  &system
  ibrav=  8,
     celldm(1)=    7.26188,
     celldm(2)=    1.0274852581,
     celldm(3)=    3.0451687357,
      nat =  98,
       ntyp = 4,
       ecutwfc = 60.0,
       ecutrho = 480.0,
/
      &electrons
       mixing_beta = 0.2
      conv_thr =1.0d-2
 /
```

```
(20)      &ions
(21)      ion_dynamics='damp',
 /
(22)      &cell
(23)      press=0.0
 /
(24)      ATOMIC_SPECIES
```

APPENDIX I CONT…………

```
 Gd  157.25     Gd.pbe-spdn-rrkjus_psl.1.0.0.UPF
 Ba  137.327    Ba.pbe-nsp-van.UPF
  Cu  63.546    Cu.pbe-d-rrkjus.UPF
  O   15.9994   O.pbe-van_bm.UPF

(25)      ATOMIC_POSITIONS (crystal)
 Ba       0.500000000   0.500000000   0.180760126
 Ba       0.500000000   0.500000000   0.819239874
 Gd       0.500000000   0.500000000   0.500000000
 Cu       0.000000000   0.000000000   0.656717737
 Cu       0.000000000   0.000000000   0.343282263
 Cu       0.000000000   0.000000000   0.000000000
 O       0.000000000   0.000000000   0.834403347
 O       0.000000000   0.000000000   0.165596653
 O       0.000000000   0.500000000   0.619777593
 O       0.000000000   0.500000000   0.380222407
 O       0.500000000   0.000000000   0.621973247
 O       0.500000000   0.000000000   0.378026753
 O       0.000000000   0.500000000   0.000000000


(26)      K_POINTS automatic
          6 6 2 1 1 1
```

The lines number are explained as follows;

(1) &control: Indicates the control block where general information that will guide the computational process without special parameters related to the material are located

(2) pseudo_dir = './ : Directs the code to where the Pseudo potentials are kept and in this case they are kept within the directory containing the script to guide the calculation.

(3) Calculation = 'relax', ': Directs the the plane wave self-consistent (PWSCF) the calculation to be performed.

(4) Prefix = 'Gab', : Indicates the filename prefix that will be used for temporary files from which any information needed for other calculation will be fetched.
(5) Restart_mode='from_scratch',: indicates that the code will be generating a new structure
(6) tstress =.true.,: Is a flag for calculation of stresses. If false, the code will not compute the stresses.
(7) tprnfor = .true.: Is a flag for calculation of forces. If false, the code will not compute the forces.
(8) /: Indicates the end of the block
(9) &system
(10) ibrav= 8,
(11) celldm(1)= 7.26188,
(12) celldm(2)= 1.0274852581,
(13) celldm(3)= 3.0451687357,
(14) nat = 98,
(15) ntyp = 4,
(16) ecutwfc = 60.0,
(17) ecutrho = 480.0,
/

Line 9-17: is the block ibrave for the crystal system. The ibrav= 8,
Is a simple orthorhombic structure. The ibrav is important in the calculation because it defines the symmetry of the structure which then can reduce the number of calculation to be done to achieve the ground state conditions and thus reduce the computation time. The celldm defines the dimensions of the structure and for this calculation the values were given in atomic units, or bohrs. For the orthorhombic structure, $a \neq b \neq c$. Nat-represents the total number of atoms in the structure and for the $GdBa_2Cu_3O_{7-x}$, it has 13 atoms. Ntyp – represents the number of the types of atoms and the structure has 4 atom types. Ecutwfc – is the Kinetic energy cutoff value for the pseudo-potentials.

/

(18) &electrons

(19) mixing beta = 0.2

(20) conv_thr =1.0d-2

Line 18-19 is the electron block. conv_thr =1.0d-2- refers to the minimum energy difference between different cycles that should be achieved before convergence.

```
 /
    (21)          &ions
    (22)          ion dynamics='damp',
   /
```

Line 21-22 represents the ion dynamic block. Depending on the type of calculation different possibilities and different default values can apply. Ion dynamics='damp',- is specifically used for structural relaxation calculations in which the optimization is considered to be constrained.

```
        (23)      &cell
        (24)      press=0.0
   /
```

Line 23-24, defines the dynamics for the cell and different possibilities are allowed depending on the type of calculation the is being undertaken. Press- means the target pressure for the calculation in KBars. Press=0.0 means that the calculation will run at zero pressure. Other values can apply if the calculation is to be run at higher pressure.

```
    (25)          ATOMIC_SPECIES
Gd 157.25         Gd.pbe-spdn-rrkjus_psl.1.0.0.UPF
Ba 137.327        Ba.pbe-nsp-van.UPF
 Cu 63.546        Cu.pbe-d-rrkjus.UPF
 O   15.9994      O.pbe-van_bm.UPF
```

Line 25 declares the atomic species in the structure. The masses and the pseudo potentials used are also included in the block

```
      (26)        ATOMIC_POSITIONS (crystal)
   Ba     0.500000000   0.500000000   0.180760126
   Ba     0.500000000   0.500000000   0.819239874
   Gd     0.500000000   0.500000000   0.500000000
   Cu     0.000000000   0.000000000   0.656717737
   Cu     0.000000000   0.000000000   0.343282263
   Cu     0.000000000   0.000000000   0.000000000
   O      0.000000000   0.000000000   0.834403347
   O      0.000000000   0.000000000   0.165596653
   O      0.000000000   0.500000000   0.619777593
   O      0.000000000   0.500000000   0.380222407
   O      0.500000000   0.000000000   0.621973247
   O      0.500000000   0.000000000   0.378026753
   O      0.000000000   0.500000000   0.000000000
      (27)        K_POINTS automatic
          6 6 2 1 1 1
```

Line 27 represents the k-point selection. The word ‘automatic’ directs the plane wave self-consistent field to generate automatically generate the k-point grid. The k-points are represented in the form of nkx nky nkz offx offy offz where nk, is the actual number of intervals in a given direction and off, is the offset of the grid.

1.3 Scf Calculation

The scf calculation is carried out under less grid of the k-points. The input file that was used for this calculation is:

```
&control
   pseudo_dir  = './ ‘,
   calculation = 'scf',
   prefix = 'Gab',
   restart_mode='from_scratch',
   tstress =.true.,
   tprnfor =.true.,
   outdir ='./tmp/'
 /
 &system
    ibrav=  8,
    celldm(1)=   6.534937498,
    celldm(2)=   0.929272686,
    celldm(3)=   2.601014353,
   nat =  13,
   ntyp = 4,
   ecutwfc = 60.0,
   ecutrho = 480.0,
     &electrons
       mixing_beta = 0.2
       conv_thr =1.0d-8
      /

    ATOMIC_SPECIES
      Gd  157.25          Gd.pbe-spdn-rrkjus_psl.1.0.0.UPF
      Ba  137.327         Ba.pbe-nsp-van.UPF
      Cu  63.546          Cu.pbe-d-rrkjus.UPF
      O   15.9994         O.pbe-van_bm.UPF

     ATOMIC_POSITIONS (crystal)
     Ba      0.500000000   0.500000000   0.180760126
     Ba      0.500000000   0.500000000   0.819239874
     Gd      0.500000000   0.500000000   0.500000000
     Cu      0.000000000   0.000000000   0.656717737
     Cu      0.000000000   0.000000000   0.343282263
     Cu      0.000000000   0.000000000   0.000000000
```

```
O       0.000000000   0.000000000   0.834403347
O       0.000000000   0.000000000   0.165596653
O       0.000000000   0.500000000   0.619777593
O       0.000000000   0.500000000   0.380222407
O       0.500000000   0.000000000   0.621973247
O       0.500000000   0.000000000   0.378026753
O       0.000000000   0.500000000   0.000000000

K_POINTS automatic
 6 6 2  1 1 1
```

1.4. Nscf Calculation

The input file for nscf calculation is the same as that of scf with three changes: calculation = ‘nscf’, restart mode = ‘restart’ and the increased number of the k-points. For this work all the nscf calculations used the grid of 9 9 9 1 1 1.

1.5. Calculation of Bands

This is performed using the calculation = ‘bands’. The k-point for this calculation are picked in a reciprocal space and this are picked from all the available k-pints. The structure for this work was:

```
&control
   pseudo_dir  = '/mnt/lustre/users/jagora/GdBaCuO_dos',
   calculation = 'nscf',
   prefix = 'Gab',
    restart_mode='from_scratch',
      tstress =.true.,
        tprnfor =.true.,
        outdir ='./tmp/'
     /
     &system
```

```
   ibrav=  8,
   celldm(1)=   6.415189605,
   celldm(2)=   0.911586423,
   celldm(3)=   2.6636334554,
  nat =  13,
  ntyp = 4,
  ecutwfc = 60.0,
  ecutrho = 480.0,
  nbnd=50,
 /
 &electrons
  mixing_beta = 0.2
  conv_thr =1.0d-8
 /
ATOMIC_SPECIES
 Gd  157.25    Gd.pbe-spdn-rrkjus_psl.1.0.0.UPF
 Ba  137.327   Ba.pbe-nsp-van.UPF
 Cu  63.546    Cu.pbe-d-rrkjus.UPF
 O   15.9994   O.pbe-van_bm.UPF

  ATOMIC_POSITIONS (crystal)
  Ba      0.500000000   0.500000000   0.180760126
  Ba      0.500000000   0.500000000   0.819239874
  Gd      0.500000000   0.500000000   0.500000000
  Cu      0.000000000   0.000000000   0.656717737
  Cu      0.000000000   0.000000000   0.343282263
  Cu      0.000000000   0.000000000   0.000000000
  O       0.000000000   0.000000000   0.834403347
  O       0.000000000   0.000000000   0.165596653
  O       0.000000000   0.500000000   0.619777593
  O       0.000000000   0.500000000   0.380222407
```

APPENDIX III

2.1 Bulk Modulus Calculation

The calculation offers means to calculate the equations of state and for this work we applied the murnaghan equation of state. In the calculation the energy of the system is calculate in different volumes of the unit cell. This is achieved by running several SCF calculations at different values of lattice parameters which represent different volumes and the corresponding energies noted. A typical file of the calculation is shown below;

```
# equation of state: murnaghan.      chisq = 0.1081D-08
# V0 = 1203.15 a.u.^3,  k0 = 1153 kbar,  dk0 =  5.03  d2k0 =  0.000  emin =-
1278.37671
# V0 =  178.29  Ang^3,  k0 = 115.3 GPa

##########################################################################
#####
# Vol.        E_calc           E_fit    E_diff     Pressure      Enthalpy
# a.u.^3          Ry             Ry         Ry          GPa            Ry
##########################################################################
#####
 1088.40  -1278.32399  -1278.32396   -0.00003     15.03   -1277.21180
 1111.68  -1278.34462  -1278.34466    0.00004     11.20   -1277.49831
 1135.30  -1278.35980  -1278.35983    0.00003      7.78   -1277.75972
 1159.24  -1278.36997  -1278.36994   -0.00003      4.72   -1277.99837
 1183.52  -1278.37546  -1278.37542   -0.00004      1.98   -1278.21628
 1208.14  -1278.37665  -1278.37663   -0.00002     -0.47   -1278.41540
 1233.09  -1278.37389  -1278.37393    0.00004     -2.67   -1278.59745
 1258.39  -1278.36759  -1278.36762    0.00004     -4.63   -1278.76407
 1284.03  -1278.35800  -1278.35797   -0.00003     -6.40   -1278.91669
```

The table shows the equilibrium volume, Bulk modulus and its derivatives at minimum energy. The data is used to plot the plot for the equation of state.

APPENDIX IV

2.1 Total energy, Volume and Pressure

The total energy as a function of reduced volume is related to pressure by the Murnaghan's equation of state. The calculated values of the volume and energy are used to plot energy verses volume curves which are important is assessing the pressure at which phase transition occurs. The file data obtained for the calculation ran at zero pressure is shown below;

```
# omega (a.u.)**3      energy (Ry)      pressure (kbar)
1066.6332473806   -1278.2987753981     190.9137380068
1071.4947005080   -1278.3049269276     181.4138436912
1076.3561536353   -1278.3107687657     172.1701702246
1081.2176067627   -1278.3163092464     163.1746962895
1086.0790598900   -1278.3215564435     154.4196861519
1090.9405130174   -1278.3265181798     145.8976782780
1095.8019661447   -1278.3312020356     137.6014744513
1100.6634192721   -1278.3356153579     129.5241293687
1105.5248723994   -1278.3397652679     121.6589406908
1110.3863255268   -1278.3436586694     113.9994395246
1115.2477786541   -1278.3473022560     106.5393813191
1120.1092317815   -1278.3507025187      99.2727371535
1124.9706849088   -1278.3538657525      92.1936853994
1129.8321380362   -1278.3567980634      85.2966037397
1134.6935911635   -1278.3595053748      78.5760615273
1139.5550442909   -1278.3619934338      72.0268124682
1144.4164974182   -1278.3642678169      65.6437876128
1149.2779505456   -1278.3663339360      59.4220886427
1154.1394036729   -1278.3681970439      53.3569814382
1159.0008568003   -1278.3698622394      47.4438899142
1163.8623099276   -1278.3713344728      41.6783901117
1168.7237630550   -1278.3726185506      36.0562045345
1173.5852161823   -1278.3737191402      30.5731967179
1178.4466693097   -1278.3746407746      25.2253660214
1183.3081224370   -1278.3753878568      20.0088426334
1188.1695755644   -1278.3759646639      14.9198827795
1193.0310286917   -1278.3763753515       9.9548641245
1197.8924818191   -1278.3766239572       5.1102813605
1202.7539349464   -1278.3767144048       0.3827419718
```

1207.6153880738	-1278.3766505076	-4.2310378298
1212.4768412011	-1278.3764359725	-8.7342370090
1217.3382943285	-1278.3760744026	-13.1299334543
1222.1997474558	-1278.3755693011	-17.4211075783
1227.0612005832	-1278.3749240743	-21.6106457758
1231.9226537105	-1278.3741420346	-25.7013437456
1236.7841068379	-1278.3732264033	-29.6959096835
1241.6455599652	-1278.3721803139	-33.5969673498
1246.5070130926	-1278.3710068143	-37.4070590186
1251.3684662199	-1278.3697088698	-41.1286483127
1256.2299193473	-1278.3682893656	-44.7641229298
1261.0913724746	-1278.3667511089	-48.3157972635
1265.9528256020	-1278.3650968321	-51.7859149248
1270.8142787293	-1278.3633291941	-55.1766511669
1275.6757318567	-1278.3614507834	-58.4901152194
1280.5371849840	-1278.3594641195	-61.7283525324
1285.3986381114	-1278.3573716557	-64.8933469381
1290.2600912387	-1278.3551757804	-67.9870227300
1295.1215443661	-1278.3528788195	-71.0112466647
1299.9829974935	-1278.3504830382	-73.9678298902
1304.8444506208	-1278.3479906427	-76.8585298010
1309.7059037482	-1278.3454037819	-79.6850987200

APPENDIX V

4.1 Super Cell (Crystal)

A solid crystal is usually defined by a unit cell. A super cell has infinite number of unit cells but still can describe the same crystal. Super cells are usually used to determine the properties that cannot be described by a unit cell such has varying the concentration of atoms in a structure. To create a super cell using the quantum espresso package, software called phonopy is used. The phonopy software uses the Pwscf file. The output will show the number of atoms and the 'CELL_PARAMETERS' and atom positions for super cell. A typical example for the output file for the super cell generated in this work is shown below;

```
!    ibrav = 0, nat = 104, ntyp = 4
CELL_PARAMETERS bohr
 14.4677433052524282    0.0000000000000000    0.0000000000000000
  0.0000000000000000   14.7889967485508755    0.0000000000000000
   0.0000000000000000    0.0000000000000000   82.5583554754268789
ATOMIC_SPECIES
 Ba 137.32700   Ba.pbe-nsp-van.UPF
 Gd 157.25000   Gd.pbe-spdn-rrkjus_psl.1.0.0.UPF
 Cu   63.54600   Cu.pbe-d-rrkjus.UPF
  O   15.99940   O.pbe-van_bm.UPF
                                   ATOMIC_POSITIONS crystal
      Site n.    Atom
       1          Ba tau (1) = (   0.2502350   0.2571128   0.2759381  )
       2          Ba tau (2) = (   0.7500000   0.2568713   0.2752225  )
       3          Ba tau (3) = (   0.2500000   0.7706139   0.2752225  )
       4          Ba tau (4) = (   0.7500000   0.7706139   0.2752225  )
       5          Ba tau (5) = (   0.2500000   0.2568713   1.7978069  )
       6          Ba tau (6) = (   0.7500000   0.2568713   1.7978069  )
       7          Ba tau (7) = (   0.2500000   0.7706139   1.7978069  )
       8          Ba tau (8) = (   0.7500000   0.7706139   1.7978069  )
       9          Ba tau (9) = (   0.2500000   0.2568713   1.2473618  )
      10          Ba tau (10) = (   0.7500000   0.2568713   1.2473618  )
      11          Ba tau (11) = (   0.2500000   0.7706139   1.2473618  )
      12          Ba tau (12) = (   0.7500000   0.7706139   1.2473618  )
```

```
13          Ba tau (13) = (   0.2500000   0.2568713   2.7699462  )
14          Ba tau (14) = (   0.7500000   0.2568713   2.7699462  )
15          Ba tau (15) = (   0.2500000   0.7706139   2.7699462  )
16          Ba tau (16) = (   0.7500000   0.7706139   2.7699462  )
17          Gd tau (17) = (   0.2500000   0.2568713   0.7612922  )
18          Gd tau (18) = (   0.7500000   0.2568713   0.7612922  )
19          Gd tau (19) = (   0.2500000   0.7706139   0.7612922  )
20          Gd tau (20) = (   0.7500000   0.7706139   0.7612922  )
21           Gd tau (21) = (   0.2500000   0.2568713   2.2838766  )
22           Gd tau (22) = (   0.7500000   0.2568713   2.2838766  )
23           Gd tau (23) = (   0.2500000   0.7706139   2.2838766  )
24           Gd tau (24) = (   0.7500000   0.7706139   2.2838766  )
25           Cu tau (25) = (   0.0000000   0.0000000   0.9999082  )
26           Cu tau (26) = (   0.5000000   0.0000000   0.9999082  )
27           Cu tau (27) = (   0.0000000   0.5137426   0.9999082  )
28           Cu tau (28) = (   0.5000000   0.5137426   0.9999082  )
29           Cu tau (29) = (   0.0000000   0.0000000   2.5224925  )
30           Cu tau (30) = (   0.5000000   0.0000000   2.5224925  )
31           Cu tau (31) = (   0.0000000   0.5137426   2.5224925  )
32           Cu tau (32) = (   0.5000000   0.5137426   2.5224925  )
33           Cu tau (33) = (   0.0000000   0.0000000   0.5226762  )
34           Cu tau (34) = (   0.5000000   0.0000000   0.5226762  )
35           Cu tau (35) = (   0.0000000   0.5137426   0.5226762  )
36           Cu tau (36) = (   0.5000000   0.5137426   0.5226762  )
37           Cu tau (37) = (   0.0000000   0.0000000   2.0452606  )
38           Cu tau (38) = (   0.5000000   0.0000000   2.0452606  )
39           Cu tau (39) = (   0.0000000   0.5137426   2.0452606  )
40           Cu tau (40) = (   0.5000000   0.5137426   2.0452606  )
41           Cu tau (41) = (   0.0000000   0.0000000   0.0000000  )
42           Cu tau (42) = (   0.5000000   0.0000000   0.0000000  )
43           Cu tau (43) = (   0.0000000   0.5137426   0.0000000  )
44           Cu tau (44) = (   0.5000000   0.5137426   0.0000000  )
45           Cu tau (45) = (   0.0000000   0.0000000   1.5225844  )
46           Cu tau (46) = (   0.5000000   0.0000000   1.5225844  )
47           Cu tau (47) = (   0.0000000   0.5137426   1.5225844  )
48           Cu tau (48) = (   0.5000000   0.5137426   1.5225844  )
49           O   tau (49) = (   0.0000000   0.0000000   1.2704495  )
50           O   tau (50) = (   0.5000000   0.0000000   1.2704495  )
51           O   tau (51) = (   0.0000000   0.5137426   1.2704495  )
52           O   tau (52) = (   0.5000000   0.5137426   1.2704495  )
53           O   tau (53) = (   0.0000000   0.0000000   2.7930339  )
54           O   tau (54) = (   0.5000000   0.0000000   2.7930339  )
55           O   tau (55) = (   0.0000000   0.5137426   2.7930339  )
56           O   tau (56) = (   0.5000000   0.5137426   2.7930339  )
```

```
57     O   tau (57) = (   0.0000000   0.0000000   0.2521349  )
58     O   tau (58) = (   0.5000000   0.0000000   0.2521349  )
59     O   tau (59) = (   0.0000000   0.5137426   0.2521349  )
60     O   tau (60) = (   0.5000000   0.5137426   0.2521349  )
61     O   tau (61) = (   0.0000000   0.0000000   1.7747192  )
62     O   tau (62) = (   0.5000000   0.0000000   1.7747192  )
63     O   tau (63) = (   0.0000000   0.5137426   1.7747192  )
64     O   tau (64) = (   0.5000000   0.5137426   1.7747192  )
65     O   tau (65) = (   0.0000000   0.2568713   0.9436637  )
66     O   tau (66) = (   0.5000000   0.2568713   0.9436637  )
67     O   tau (67) = (   0.0000000   0.7706139   0.9436637  )
68     O   tau (68) = (   0.5000000   0.7706139   0.9436637  )
69     O   tau (69) = (   0.0000000   0.2568713   2.4662480  )
70     O   tau (70) = (   0.5000000   0.2568713   2.4662480  )
71     O   tau (71) = (   0.0000000   0.7706139   2.4662480  )
72     O   tau (72) = (   0.5000000   0.7706139   2.4662480  )
73     O   tau (73) = (   0.0000000   0.2568713   0.5789207  )
74     O   tau (74) = (   0.5000000   0.2568713   0.5789207  )
75     O   tau (75) = (   0.0000000   0.7706139   0.5789207  )
76     O   tau (76) = (   0.5000000   0.7706139   0.5789207  )
77     O   tau (77) = (   0.0000000   0.2568713   2.1015051  )
78     O   tau (78) = (   0.5000000   0.2568713   2.1015051  )
79     O   tau (79) = (   0.0000000   0.7706139   2.1015051  )
80     O   tau (80) = (   0.5000000   0.7706139   2.1015051  )
81     O   tau (81) = (   0.2500000   0.0000000   0.9470067  )
82     O   tau (82) = (   0.7500000   0.0000000   0.9470067  )
83     O   tau (83) = (   0.2500000   0.5137426   0.9470067  )
84     O   tau (84) = (   0.7500000   0.5137426   0.9470067  )
85     O   tau (85) = (   0.2500000   0.0000000   2.4695911  )
86     O   tau (86) = (   0.7500000   0.0000000   2.4695911  )
87     O   tau (87) = (   0.2500000   0.5137426   2.4695911  )
88     O   tau (88) = (   0.7500000   0.5137426   2.4695911  )
89     O   tau (89) = (   0.2500000   0.0000000   0.5755776  )
90     O   tau (90) = (   0.7500000   0.0000000   0.5755776  )
91     O   tau (91) = (   0.2500000   0.5137426   0.5755776  )
92     O   tau (92) = (   0.7500000   0.5137426   0.5755776  )
93     O   tau (93) = (   0.2500000   0.0000000   2.0981620  )
94     O   tau (94) = (   0.7500000   0.0000000   2.0981620  )
95     O   tau (95) = (   0.2500000   0.5137426   2.0981620  )
96     O   tau (96) = (   0.7500000   0.5137426   2.0981620  )
97     O   tau (97) = (   0.0000000   0.2568713   0.0000000  )
98     O   tau (98) = (   0.5000000   0.2568713   0.0000000  )
99     O   tau (99) = (   0.0000000   0.7706139   0.0000000  )
100    O   tau (80) = (   0.5000000   0.7706139   2.1015051  )
```

```
101          O   tau (81) = (   0.2500000   0.0000000   0.9470067  )
102          O   tau (82) = (   0.7500000   0.0000000   0.9470067  )
103          O   tau (83) = (   0.2500000   0.5137426   0.9470067  )
104          O   tau (84) = (   0.7500000   0.5137426   0.9470067  )
```

APENDIX VI

5.1 Publications

(1) Elastic behavior, pressure-induced doping and superconducting transition temperature of $GdBa_2Cu_3O_{7-x}$ **Jared O Agora**, **Calford Otieno**, **Philip W O Nyawere** and **George S Manyali Published 13 January 2022.**

(2) Ab initio study of pressure induced phase transition, structural and electronic structure properties of superconducting perovskite compound $GdBa_2Cu_3O_{7-x}$

Jared O.Agora, CalfordOtieno, Philip W.O.Nyawere, George S.Manyali

APENDIX VII

6.1 Conferences

1. International conference on Computing and information systems techniques held on 8th-9th October 2018 at Kabarak University.
2. 2nd computational and theoretical physics annual workshop (CTheP) held on 12th -13th June 2019 at Kakamega Guest House, Kakamega Kenya.